Ceramic Materials for Energy Applications V

Ceramic Engineering and Science Proceedings
Volume 36, Issue 7, 2015

Josef Matyáš
Yutai Katoh
Hua-Tay Lin
Alberto Vomiero
Editors

Jingyang Wang
Soshu Kirihara
Volume Editors

The American Ceramic Society

WILEY

Ceramic Materials for Energy Applications V

Ceramic Materials for Energy Applications V

A Collection of Papers Presented at the 39th International Conference on Advanced Ceramics and Composites January 25–30, 2015 Daytona Beach, Florida

Editors
Josef Matyáš
Yutai Katoh
Hua-Tay Lin
Alberto Vomiero

Volume Editors
Jingyang Wang
Soshu Kirihara

WILEY

Published by John Wiley & Sons, Inc., Hoboken, New Jersey.
Published simultaneously in Canada.

Library of Congress Cataloging-in-Publication Data is available.

ISBN: 978-1-119-21169-3
ISSN: 0196-6219

Printed in the United States of America.

10 9 8 7 6 5 4 3 2 1

Contents

Preface

This proceedings issue contains contributions from three energy related symposia that were part of the 39th International Conference on Advanced Ceramics and Composites (ICACC), in Daytona Beach, Florida, January 25-30, 2015:

- Advanced Ceramics and Composites for Sustainable Nuclear Energy and Fusion Energy
- Advanced Materials and Technologies for Energy Generation, Conversion, and Rechargeable Energy Storage
- Advanced Ceramic Materials and Processing for Photonics and Energy

The first two symposia were sponsored by The American Ceramic Society's (ACerS) Engineering Ceramics Division and the third by ACerS Nuclear & Environmental Technology Division.

The editors wish to thank the authors and presenters for their contributions, the symposium organizers for their time and labor, and all the manuscript reviewers for their valuable comments and suggestions. Acknowledgment is also due for financial support from the Engineering Ceramics Division, the Nuclear & Environmental Technology Division, and The American Ceramic Society. The editors wish to thank ACerS for assembling and publishing the proceedings.

Josef Matyáš, Pacific Northwest National Laboratory, USA
Yutai Katoh, Oak Ridge National Laboratory, USA
Hua-Tay Lin, Guangdong University of Technology, China
Alberto Vomiero, Luleå University of Technology, Sweden

Introduction

This CESP issue consists of papers that were submitted and approved for the proceedings of the 39th International Conference on Advanced Ceramics and Composites (ICACC), held January 25–30, 2015 in Daytona Beach, Florida. ICACC is the most prominent international meeting in the area of advanced structural, functional, and nanoscopic ceramics, composites, and other emerging ceramic materials and technologies. This prestigious conference has been organized by the Engineering Ceramics Division (ECD) of The American Ceramic Society (ACerS) since 1977.

The 39th ICACC hosted more than 1,000 attendees from 40 countries and over 800 presentations. The topics ranged from ceramic nanomaterials to structural reliability of ceramic components which demonstrated the linkage between materials science developments at the atomic level and macro level structural applications. Papers addressed material, model, and component development and investigated the interrelations between the processing, properties, and microstructure of ceramic materials.

The 2015 conference was organized into the following 21 symposia and sessions:

Symposium 1	Mechanical Behavior and Performance of Ceramics and Composites
Symposium 2	Advanced Ceramic Coatings for Structural, Environmental, and Functional Applications
Symposium 3	12th International Symposium on Solid Oxide Fuel Cells (SOFC): Materials, Science, and Technology
Symposium 4	Armor Ceramics: Challenges and New Developments
Symposium 5	Next Generation Bioceramics and Biocomposites
Symposium 6	Advanced Materials and Technologies for Energy Generation and Rechargeable Energy Storage
Symposium 7	9th International Symposium on Nanostructured Materials and Nanocomposites
Symposium 8	9th International Symposium on Advanced Processing & Manufacturing Technologies for Structural & Multifunctional Materials and Systems (APMT), In Honor of Prof. Stuart Hampshire

Symposium 9	Porous Ceramics: Novel Developments and Applications
Symposium 10	Virtual Materials (Computational) Design and Ceramic Genome
Symposium 11	Advanced Materials and Innovative Processing ideas for the Industrial Root Technology
Symposium 12	Materials for Extreme Environments: Ultrahigh Temperature Ceramics (UHTCs) and Nanolaminated Ternary Carbides and Nitrides (MAX Phases)
Symposium 13	Advanced Ceramics and Composites for Sustainable Nuclear Energy and Fusion Energy
Focused Session 1	Geopolymers, Chemically Bonded Ceramics, Eco-friendly and Sustainable Materials
Focused Session 2	Advanced Ceramic Materials and Processing for Photonics and Energy
Focused Session 3	Materials Diagnostics and Structural Health Monitoring of Ceramic Components and Systems
Focused Session 4	Additive Manufacturing and 3D Printing Technologies
Focused Session 5	Single Crystalline Materials for Electrical, Optical and Medical Applications
Focused Session 6	Field Assisted Sintering and Related Phenomena at High Temperatures
Special Session	2nd European Union-USA Engineering Ceramics Summit
Special Session	4th Global Young Investigators Forum

The proceedings papers from this conference are published in the below seven issues of the 2015 CESP; Volume 36, Issues 2-8, as listed below.

- Mechanical Properties and Performance of Engineering Ceramics and Composites X, CESP Volume 36, Issue 2 (includes papers from Symposium 1)
- Advances in Solid Oxide Fuel Cells and Electronic Ceramics, CESP Volume 36, Issue 3 (includes papers from Symposium 3 and Focused Session 5)
- Advances in Ceramic Armor XI, CESP Volume 36, Issue 4 (includes papers from Symposium 4)
- Advances in Bioceramics and Porous Ceramics VIII, CESP Volume 36, Issue 5 (includes papers from Symposia 5 and 9)
- Advanced Processing and Manufacturing Technologies for Nanostructured and Multifunctional Materials II, CESP Volume 36, Issue 6 (includes papers from Symposia 7 and 8 and Focused Sessions 4 and 6)
- Ceramic Materials for Energy Applications V, CESP Volume 36, Issue 7 (includes papers from Symposia 6 and 13 and Focused Session 2)
- Developments in Strategic Ceramic Materials, CESP Volume 36, Issue 8 (includes papers from Symposia 2, 10, 11, and 12; from Focused Sessions 1 and 3); the European-USA Engineering Ceramics Summit; and the 4th Annual Global Young Investigator Forum

The organization of the Daytona Beach meeting and the publication of these proceedings were possible thanks to the professional staff of ACerS and the tireless

dedication of many ECD members. We would especially like to express our sincere thanks to the symposia organizers, session chairs, presenters and conference attendees, for their efforts and enthusiastic participation in the vibrant and cutting-edge conference.

ACerS and the ECD invite you to attend the Jubilee Celebration of the 40th International Conference on Advanced Ceramics and Composites (http://www.ceramics.org/daytona2016) January 24-29, 2016 in Daytona Beach, Florida.

To purchase additional CESP issues as well as other ceramic publications, visit the ACerS-Wiley Publications home page at www.wiley.com/go/ceramics.

JINGYANG WANG, Institute of Metal Research, Chinese Academy of Sciences, Shenyang, China
SOSHU KIRIHARA, Osaka University, Osaka, Japan

Volume Editors
July 2015

Ceramics and Composites for Sustainable Nuclear and Fusion Energy

HOOP TENSILE STRENGTH OF CMC TUBES FOR LWRS APPLCATIONS USING INTERNAL PRESSURIZATION VIA ELASTOMERIC INSERT: NEW ASTM TEST METHOD

Michael G. Jenkins, Bothell Engineering & Science Technologies, Bothell, WA, USA,
jenkinsmg@bothellest.com

Jonathan A. Salem, NASA Glenn Research Center, Cleveland, OH, USA,
jonathan.a.salem@nasa.gov

Janine E. Gallego, Bothell Engineering & Science Technologies, Bothell, WA, USA,
gallegoje@bothellest.com

ABSTRACT

The US DOE plans to replace conventional zirconium-alloy fuel rod tubes in light water reactors (LWR) with those consisting of SiC/SiC CMCs to enhance fuel performance and accident tolerance. SiC/SiC CMCs show tolerance to the irradiation and chemical environments of LWRs. Failure modes in LWR fuel cladding include loss of gas tightness and mechanical integrity due to the build-up of internal gas pressure and the swelling of fuel pellets. Therefore, determination of the hoop tensile strength is critically important for evaluation of SiC/SiC CMC fuel claddings. A new ASTM standard test method (C1819) has been developed and is in the final publication stages. The standard uses internal pressurization developed by longitudinal compression of an elastomeric insert to produce radial pressure that results in tensile hoop stresses in CMC tubular test specimens. This test method is based on sound, theoretical analysis of the stresses developed in tubes subjected to internal pressure over a finite length inside a semi-infinitely long tube. The new ASTM test method contains information on test specimen dimensions, testing geometries, test conditions and results interpretation based on this theory and subsequent empirical tests applied to various materials and geometries. This test method is intended for for material development, material characterization, material screening, and quality assurance.

INTRODUCTION

US Department of Energy (US DOE) has proposed replacing conventional zirconium-alloy fuel rod tubes in light water reactors (LWRs) with fuel rods fabricated in whole or in part from ceramic matrix composite (CMC) materials in order to enhance fuel performance and accident tolerance.[1,2,3,4] Because of their demonstrated tolerance to the irradiation and chemical environments of LWRs, silicon carbide continuous fiber-reinforced silicon carbide-matrix (SiC/SiC) CMCs have been targeted for this application. It is noteworthy that SiC/SiC materials exhibit high strength at elevated temperatures and low chemical activity (e.g., no exothermic reaction with water that produces hydrogen gas as zirconium demonstrates at elevated temperatures). In addition, the high-temperature properties of SiC/SiC CMCs indicate that the fuel system using this CMC can retain its geometry and fuel protective functionality even during an accident. Elimination of the exothermic zirconium and water reaction (and the attendant generation of free hydrogen) also increases the temperature at which the fuel can operate, thereby lowering the type of risks created during an accident scenario [1,2].

Anticipated failure modes for the LWR fuel cladding include loss of gas tightness and mechanical integrity due to the build-up of internal gas pressure and the swelling of fuel pellets. Thus, it is critically important to rigorously determine the hoop tensile or equivalent strength properties when evaluating SiC/SiC CMC fuel claddings.

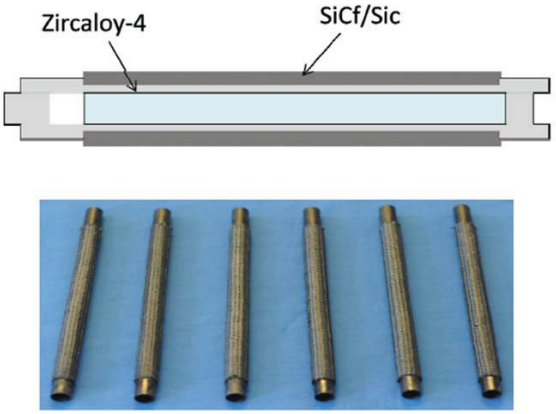

Figure 1 SiC/SiC CMC cladding for LWR fuel rods (from Ref 1)

SiC/SiC CMCs consist of high-strength silicon carbide fiber secondary (or reinforcement) phase in a high-temperature silicon carbide primary (or matrix) phase. In addition to high strength and high fracture resistance at elevated temperatures, this type of composite structure combined with the silicon carbide material results in potentially greater resistance to neutron radiation[5] compared to conventional materials. The ceramic reinforcement in the form of fibre tows have high filament counts (500-2000) and are woven with large units cells, several millimeters in size. In tubular configurations the composites may be constructed as a 1-D filament wound, 2-D laminate, or 3-D (weave or braid) configuration depending on what tensile, shear, and hoop stresses are considered. The fiber architecture in the tubes can be geometrically tailored for highly anisotropic or uniform isotropic mechanical and thermal properties.[2, 3]

Tubular geometries for nuclear applications present challenges for both the material fabricators and the material evaluators of SiC/SiC CMCs. For fabricators, challenges include the following: how to make seamless tubes with multiple direction architectures?; how to ensure integrity in the radial direction?; and how to create uniform wall thickness and uniform/nonporous matrices? For evaluators, challenges include: how to build on decades of experience with consensus standards and data bases for "flat" material forms?; how to interpret information from tests of test specimen in component form?; and how to adapt expertise at room temperature in ambient environments to conditions at high temperature in specific extreme-use environments?

It is important to note that until recently, there were no commonly-accepted design methodologies for tubular components comprised of advanced composite, and in particular, there few mechanical test standards for any of these properties of tubular geometry ceramic composite components. Fortunately, in 2013, a new standard[6] for axial tensile strength of CMC tubes approved and published by ASTM as C1773 "Standard Test Method for Monotonic Tensile Behavior of Continuous Fiber-Reinforced Advanced Ceramic Tubular Test Specimens at Ambient Temperature"[6] after several years of development.

It in important to note that use of CMCs in LWR applications requires mechanical test standards to support not only material development and property databases, but also design codes and component specification documents, as well as Nuclear Regulatory Commission (NRC) regulations on nuclear

design approval, certification, and licensing.[3, 4, 5] In particular, mechanical test standards for nuclear-grade CMCs are necessary to provide accurate, reliable, and statistically-significant data as determined from technically-rigorous, well-defined test methods, detailed test specimen preparation, comprehensive reporting requirements, and commonly-accepted terminology. Development and design of LWR components composed of CMCs could be hampered and delayed if appropriate standards of mechanical test methods are not available in a timely manner.

It is noteworthy that the timing of nuclear applications of SiC/SiC CMCs in LWR components is such that they can advance an existing mature specialized technology of CMCs. In particular, the large strides in development of SiC/SiC CMC materials and structure technology were made possible by funding from the aerospace and defense industries/agencies. Additionally, current evaluation and application of SiC/SiC CMCs in fusion reactors (first wall) and tristructural-isotropic (TRISO) fuel forms provide established properties under extended neutron irradiation and at high temperatures as well as very hot steam environment. Expanding, statistically-significant data bases for SiC/SiC CMCs now exist because of the evolution of consensus test methods and design codes. Finally, maturation of volume-scale manufacturing capability for all types of CMCs including SiC/SiC CMCs adds to the availability and understanding of these materials.

Professional organizations such as American Society of Mechanical Engineers (ASME) and ASTM International are leading the way in developing the codes, specifications, and test standards for CMCs in nuclear applications. ASTM International Committee C28 on Advanced Ceramics has a particular focus on mechanical test standards for CMCs.[7, 8] Specifically, ASTM Subcommittee C28.07 on Ceramic Composites has published fourteen standards for CMCs (e.g., tensile, flexure, shear, compression, creep, fatigue, etc.) [7, 8]

Mechanical testing of composite tube geometries is distinctly different from testing flat plates because of the differences in fiber architecture (weaves, braids, filament wound), stress conditions (hoop, torsion, and flexure stresses), gripping, bending stresses, gage section definition, and scaling issues.[5] Because there are no commonly-accepted design methodologies for advanced composite tubular components, there are almost no mechanical test standards for any properties of tubular ceramic composite components.

Therefore, in this paper, some aspects are presented for a new ASTM standard test method for hoop tensile strength of CMC tubes that has been approved in 2015 via consensus balloting (C1819)[11]. This new standard uses axial compression of elastomeric inserts to produce radial internal pressure and resulting hoop stresses in composite tubular test specimens. This new standard is based on sound, theoretical analysis of the stresses developed in tubes subjected to internal pressure over a finite length inside a semi-infinitely long tube [9, 10] The new standard uses theory as well as subsequent empirical tests applied to various materials and geometries. This test method (a.k.a., overhung tube method) is for material development, material comparison, material screening, material down selecting and quality assurance.

ASTM STANDARD TEST METHOD

A working group within ASTM Subcommittee C28.07 on CMC tube testing developed the new standard[11]: C1819 “Standard Test Method for Hoop Tensile Strength of Continuous Fiber-Reinforced Advanced Ceramic Composite Tubular Test Specimens at Ambient Temperature Using Elastomeric Inserts” over a two year period with final approval by balloting received in 2015. This new standard is discussed in the following sections. The working group is also preparing a second draft, “Standard Test Method for Hoop Tensile Behavior of Continuous Fiber-Reinforced Advanced Ceramic Composite Tubular Test Specimens at Ambient Temperature Using Internal Pressurization” that will be the subject of a future publication.

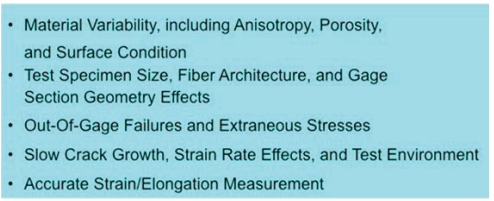

Figure 2 Range of "interferences" in test CMC materials

SCOPE AND APPLICATION

This new standard test method covers the determination of the hoop tensile strength including stress-strain response of continuous fiber-reinforced advanced ceramic tubes subjected to an internal pressure produced by the expansion of an elastomeric insert undergoing monotonic uniaxial loading at ambient temperature. This type of test configuration is sometimes referred to as an overhung tube. This test method is specific to tube geometries, because flaw populations, fiber architecture and specimen geometry factors are often distinctly different in composite tubes, as compared to flat plates.

In the test method a composite tube/cylinder with a defined gage section and a known wall thickness is loaded via internal pressurization from the radial expansion of an elastomeric insert (located midway inside the tube) that is longitudinally compressed from either end by pushrods. The elastomeric insert expands under the uniaxial compressive loading of the pushrods and exerts a uniform radial pressure on the inside of the tube. The resulting hoop stress-strain response of the composite tube is recorded until failure of the tube. The hoop tensile strength and the hoop fracture strength are determined from the resulting maximum pressure and the pressure at fracture, respectively. The hoop tensile strains, the hoop proportional limit stress, and the modulus of elasticity in the hoop direction are determined from the stress-strain data. Note that hoop tensile strength as used in this test method refers to the tensile strength in the hoop direction from the induced pressure of a monotonic, uniaxially-loaded elastomeric insert where monotonic refers to a continuous nonstop test rate without reversals from test initiation to final fracture.

This test method applies primarily to advanced ceramic matrix composite tubes with continuous fiber reinforcement: uni-directional (1-D, filament wound and tape lay-up), bidirectional (2-D, fabric/tape lay-up and weave), and tridirectional (3-D, braid and weave). These types of ceramic matrix composites can be composed of a wide range of ceramic fibers (oxide, graphite, carbide, nitride, and other compositions) in a wide range of crystalline and amorphous ceramic matrix compositions (oxide, carbide, nitride, carbon, graphite, and other compositions).

EXPERIMENTAL FACTORS

CMCs generally exhibit "graceful" failure from a cumulative damage process, unlike monolithic advanced ceramics that fracture catastrophically from a single dominant flaw. The testing of CMC (both flats and tubes) has a range of different material and experimental factors that interact and must be controlled and managed (See Fig. 2). These factors must be managed and understood to produce consistent, representative failures in the gage section of test specimens. Tubular test specimens with cylindrical geometries provide particular challenges in the areas of gage section geometry, loading failures, extraneous "parasitic" stresses (including biaxial and triaxial stresses), and out-of-gage failures.

TEST SPECIMEN GEOMETRIES

Test Specimen Size -- CMC tubes are fabricated in a wide range of geometries and sizes, across a spectrum of fiber-matrix-architecture combinations. It is not practical to define a single test specimen geometry that is universally applicable. The selection and definition of a test specimen geometry depends on the purpose of the testing effort. With that consideration, the test method is generally applicable to tubes with outer diameters (D_o) of 10 to 150 mm and wall thicknesses (t) of 1 to 25 mm, where the ratio of the outer diameter to wall thickness is commonly $D_o/t = 5$ to 30. Tube sections used for test specimens may vary depending on the type of test (e.g., 25 mm to 1000 mm). In many cases, the wall thickness is defined by the number of plies and fiber-reinforcement architecture of the available tube geometry, particularly for woven and braided configurations.

Experience has shown that successful tests can be maximized by using consistent ranges of relative gage section dimensions. Previous studies[9,10] have shown that pressurized length of the tube, L, and hence initial length of the insert should be:

$$L \geq 9/\beta \quad \text{and} \quad \beta = \sqrt[4]{\frac{3(1-\nu^2)}{\left(r_i^{tube}\right)^2 t^2}} \tag{1}$$

where r_i^{tube} is the inner radius of tubular test specimen, t is the wall thickness in the gage section of the tube and ν is Poisson's ratio of test material. Deviations from the recommended geometries may be necessary depending upon the particular composite tube geometry being evaluated.

TEST EQUIPMENT AND PROCEDURES

Test setup, Force and Strain Measurement, Data Acquisition -- The test method can use a standard load frame with a hydraulic or screw drive loading mechanism and standard force transducers for controlled axial loading for the elastomer insert test method. Guidance is given regarding type, composition and properties of the elastomeric insert material. Primary hoop strain measurement can be measured by strain gages and/or string extensometers in the "gage section." If required, an environmental test chamber may be used to control humidity and ambient temperature. Data collection should be done with a minimum of 50-Hz response and an accuracy of ±0.1 % for all data.

Test Procedure -- Generally, a displacement-based, test mode is used to avoid "run-away" tests that sometimes occur in force-control tests. Test mode rates are chosen so as to produce test specimen failures in 5-50 s. Failure within one minute or less should be sufficient to minimize slow-crack growth (SCG) effects. If slow crack growth is observed (e.g. under slow test mode rates), subsequent tests can be accelerated to reduce or eliminate slow crack growth. The test specimen is tested in hoop tension to fracture. The test specimen is retrieved for failure analysis and post-test dimensional measurement. A minimum of five valid tests is required for the purposes of estimating a mean. A greater number of tests may be necessary, if estimates regarding the form of the strength distribution are required. Fractography is suggested if the failure mode and fracture location are of interest.

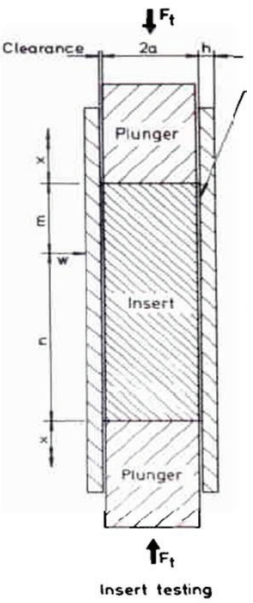

Figure 3 Illustration of test setup for insert testing (Ref. 10)

CALCULATION, REPORTING, PRECISION AND BIAS

Calculations -- Using the measured force data along with the measured strain and/or deformation data as well as the test specimen dimensions, the resulting hoop stress-strain curve for each test specimen is determined. Calculation of the hoop tensile stress is shown in Fig. 4 under the assumption of linear, elastic, homogeneous, isotropic material behavior. Note that calculations for the elastomeric insert method may need to account for friction effects between the insert and the walls of the tubular test specimen[10]. From the stress-stain curve, the following hoop tensile properties are determined: i) ultimate hoop tensile strength and corresponding strain, ii) fracture hoop tensile strength and corresponding strain, iii) proportional limit hoop tensile stress and corresponding strain, iv) elastic modulus in the circumferential direction, v) modulus of toughness.

$$\sigma_\theta = P\left[\frac{2r_i^2}{r_o^2 - r_i^2}\right] and\ \varepsilon_\theta = measured\ directly$$

[at outer radius for internal pressure]

where: $P = f(F_{axial}, A_{insert}, Elastic\ Constants, stiffnesses))$

Figure 4 Calculation of hoop stress for elastomeric insert

Reporting -- The test method provides detailed lists of reporting requirements for test identification, material and test specimen description, equipment and test parameters, and test results (statistical summary and individual test data).

Precision -- CMCs have probabilistic strength distributions, based on the inherent variability in the composite: fibers, matrix, porosity, fiber interface coatings, fiber architecture and alignment, anisotropy, and inherent surface and volume flaws. This variability occurs spatially within and between test specimens. Data variation also develops from experimental variability in test specimen dimensions, volume/size effects, extraneous bending stresses, temperature and humidity effects and the accuracy and precision of transducers and sensors.

CURRENT STATUS AND FUTURE WORK

Now that ASTM Test Method C1819 has been approved, ASTM Committee C28 is planning interlaboratory testing programs per ASTM Practice E691[12] to determine the precision (repeatability and reproducibility) for a range of ceramic composites, considering different compositions, fiber architectures, and specimen geometries. A round-robin interlaboratory testing program for hoop tensile strength will be organized and executed, given available material, funding, and participating laboratories.

CONCLUSIONS

There is a real need for a comprehensive and detailed consensus test standard for hoop tensile strength testing of CMC tubes. This need is based on the certification and qualification requirements for CMC tubes in nuclear fission reactors. Test standards for tubes are needed because tests on flat composite panels are not representative of the architecture and geometry of composite tubes, with their 2-D and 3-D fiber architectures. The new ASTM standard test method C1819 for hoop tensile testing of CMC tubes is comprehensive and detailed, providing strong procedural documents using the conventional ASTM format. This new standard test method is applicable to 1-D, 2-D, and 3-D CMC tubes with diameters up to 150 mm and wall thicknesses up to 25 mm. The test method addresses the following experimental issues -- test specimen geometries and preparation, different loading methods, test equipment, interferences (material, specimen, parasitic stresses, test conditions, etc), testing modes and procedures, data collection, calculations, reporting requirements, and precision/bias.

ACKNOWLEDGEMENT

This work was conducted with U.S. Department of Energy funding under the technical direction of Dr. Yutai Katoh at Oak Ridge National Laboratory, Oak Ridge, TN.

REFERENCES

1. G. Griffith, “U.S. Department of Energy Accident Resistant SiC Clad Nuclear Fuel” INL/CON-11-23186, Idaho National Laboratory, Idaho Fall, Idaho (2011)

2. W. E. Windes, P. A. Lessing, Y. Katoh, L. L. Snead, E. Lara-Curzio, J. Klett, C. Henager, Jr., R. J. Shinavski, “ Structural Ceramic Composites for Nuclear Applications,” Idaho National Laboratory, Report INL/EXT-05-00652, Aug. (2005)

3. L.L. Snead, Y. Kato, W. Windes, R. J. Shinavski, T. Burchell, “Ceramic Composites For Near Term Reactor Application,” Proceedings of the 4th International Topical Meeting on High Temperature Reactor Technology, HTR2008-58050, ASME International (2008)

4. M. G. Jenkins, E. Lara-Curzio, W. E. Windes, “(GENIV) Next Generation Nuclear Power And Requirements For Standards, Codes And Data Bases For Ceramic Matrix Composites,” Ceramics in Nuclear and Alternative Energy Applications, *Ceramic Engineering and Science Proceedings*, Sharon Marra, ed., American Ceramics Society, Vol. 27, Issue 5, pp. 3-9 (2007)

5. Y. Katoh, L.L. Snead, T. Nozawa, N.B. Morley, W.E. Windes, "Advanced Radiation-Resistant Ceramic Composites," *Advances in Science and Technology*, Vol. 45, pp. 1915-1924 (2006)

6. ASTM C1773-13 "Standard Test Method for Monotonic Axial Tensile Behavior of Continuous Fiber-Reinforced Advanced Ceramic Tubular Test Specimens at Ambient Temperature" ASTM International, West Conshohoken, PA (2013)

7. ASTM Committee C28, "Advanced Ceramic Sentinel." ASTM International, West Conshohoken, PA (2015)

8. *http://www.astm.org/COMMITTEE/C28.htm*

9. R. Carter, "Compressed Elastomer Method for Internal Pressure Testing", ARL-TR-3921, Aberdeen Proving Grounds, MD (2006)

10. K. Mosley, "The Stressing for Test Purposes in Tubular Form Using Elastomeric Inserts-Experimental and Theoretical Development, " *Proc. Instn Mech Engrs*, Vol 196, pp. 123-139 (1982)

11. ASTM C1819-15 "Standard Test Method for Hoop Tensile Strength of Continuous Fiber-Reinforced Advanced Ceramic Composite Tubular Test Specimens at Ambient Temperature Using Elastomeric Inserts)" ASTM International, West Conshohoken, PA (2015)

12. ASTM E691-99 "Standard Practice for Conducting an Interlaboratory Study to Determine the Precision of a Test Method," ASTM International, West Conshohoken, PA (2013)

PROPERTIES OF Al_2O_3 – CaO GLASS JOINTS OF SILICON CARBIDE TUBES

M. Gentile, T. Abram

C-NET Research Group, School of Mechanical, Aerospace and Civil Engineering, The University of Manchester, UK

ABSTRACT

This research work studies the microstructure and the properties of glass Al_2O_3-CaO glass material after laser irradiation. The Al_2O_3-CaO glass was used as joining material during laser brazing of SiC/SiC tubes for nuclear applications. The physical properties and corrosion resistance of the braze material were investigated using secondary electron microscopy and an autoclave test, while the mechanical properties of the braze were analysed using a four points bending test.

Electron optical observations reveal that at the end of the laser treatment Al_2O_3-CaO joints had a compact and homogeneous microstructure with good adhesion to the silicon carbide substrate. The joined silicon carbide specimens survived autoclave tests and the measured fracture load for the joints ranged between 80N to 180N.

The experimental results show that glass Al_2O_3-CaO material is resistant in extreme environmental condition and therefore is suitable to be used as joining material for laser brazing of silicon carbide.

INTRODUCTION

Sintered ceramics such as silicon carbide (SiC) have very good material properties with regard to thermal stability[1], corrosion resistance[2], long-term stability and radiation resistance[3,4]. Therefore, these materials offer promising advantages for a wide range of applications in the field of high temperature technology, not least for a range of nuclear applications.

In nuclear power stations, zirconium alloys have been used as fuel cladding material for water-cooled reactors for over 50 years. However, the recent Fukushima accident underlines the vulnerability of such alloys under severe accident conditions, when gross oxidation can result in the generation of large quantities of hydrogen, giving rise to the risk of an explosion. Ceramic SiC-SiC composite claddings offer significantly improved oxidation resistance and prevent explosions due to hydrogen gas generated by the reaction of zirconium cladding with steam.[5].

High performance ceramics, e.g., SiC, can widely be used in the nuclear sector because of their excellent thermochemical and radiological properties. Westinghouse, for instance, has developed a ceramic SiC-SiC composite cladding that consists in a monolithic SiC tube wound with SiC fibers tows that are infiltrated with SiC deposited through chemical vapor infiltration (CVI)[6]. However, it has not been possible to utilise this great potential since a technology for high temperature resistant joining of these ceramic materials has not yet adequately been developed[6].

Diverse technologies have been developed to join ceramics[7-9], although a joint that has application in the nuclear industry has not been identified.

Laser brazing of ceramics is a promising techniques for joining of silicon carbide. The use of laser radiation has several advantages:

1) Versatility – the bonding process can be carried out on pieces of different shapes and dimensions.
2) Reduction of time – the use of laser radiation reduces the manufacturing time of the joining process to only 5 minutes, with significant potential for further reductions, making the process cost effective.
3) Industrially competitive - A laser device tool can be easily introduced in the production line. Consequently implementing this technology on industrial scale does not require consistent modification of existing production plants.
4) Act locally - the use of laser radiation develops localised temperature gradients. Consequently the joining process affects just a restricted area of the silicon carbide, avoiding unnecessary heating of the remaining part of the material. In this way the original material can preserve its initial properties.

In order to employ laser brazing of silicon carbides in large scale manufacturing of nuclear fuel, it is necessary to develop a braze that is able to survive under radiation and in the extreme environmental conditions of a nuclear reactor. In this research work the Al_2O_3-CaO glass was used as joining material during laser brazing of SiC/SiC tubes for nuclear applications. The paper presents the microstructure and the properties of glass Al_2O_3-CaO material after laser irradiation.

EXPERIMENTAL PROCEDURE

Silicon carbide specimens (Hexoloy SA, Saint Gobain Niagara Falls) produced by pressureless sintering submicron silicon carbide powder were joined together using laser radiation and a filler material. The joined specimens had the shape of disks, tubes and bars.

The filler material was prepared blending a powder mixture containing Al_2O_3 and CaO for 24 hours. The specimens were joined using laser irradiation. A laser-supported radiation pyrometer (LumaSense Technologies GmbH) was employed to measure the surface temperature of the silicon carbide during laser irradiation. The temperature profiles were measured using the InfraWin 5.0.1.41.C software.

An autoclave test exposed three specimens of joined silicon carbide disks in water at 500 °C, 25 MPa pressure and the flow rate of 1 m/s with oxygen content of 25 ppm for seven days. The autoclave test conditions are the same conditions employed to test multilayered ceramics composite cladding for commercial water reactors in the final technical report for phase 2 SBIR project work carried out by Gamma Engineering Corporation.

The samples were dried in air. After drying an electrical microbalance was utilized to measure the weight of the silicon carbide specimens at the end of the autoclave test.

Four point bending tests measured at room temperature the strength of the joints using a universal testing machine Instron 3344. The specimens had a width of 5 mm, a length of 42 mm and a thickness of 6 mm. For the test fixture the spacing between the two supporting pins was 20 mm. The seam was centered below the two loading pins (spacing between pins: 10 mm) and loaded at a rate of 0.5 mm/min. The test series comprised 12 test specimens.

Cross sections of the joints were embedded in resin and ground/polished through successive grades followed by finishing to 1 μm diamond. Confocal laser scanning microscope (OLS4100, LEXT) and scanning electron microscope (FEG-SEM JEOL 6300, Tokyo, Japan) imaged the morphology of the joints before and after the autoclave test and after four points bending tests.

RESULTS AND DISCUSSION

Brazing of SiC

SiC-SiC bonds are created through the use of laser radiation with a process that is called ceramic brazing. A layer of joining material is placed between silicon carbide-silicon carbide pieces; subsequently the laser beam scans the seam bonding the two pieces together.

Figure 1 shows SiC disks and silicon carbide tube and lid brazed together using laser radiation. The joining technique joined together SiC specimens having different shapes and dimensions. Figure 2 reveals a confocal laser scanning microscope image of the cross sections of the joint.

The image reveals that the CA has a good adhesion to the SiC substrate. The microstructure of the braze is uniform and compact without porosity. The thickness of the joint was about 200 μm.

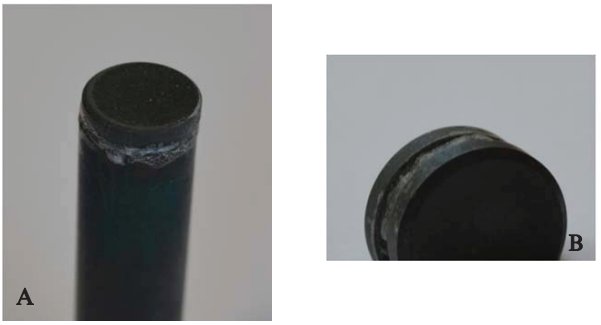

Figure 1. Braze SiC specimens: (A) tube and lid; (B) disks.

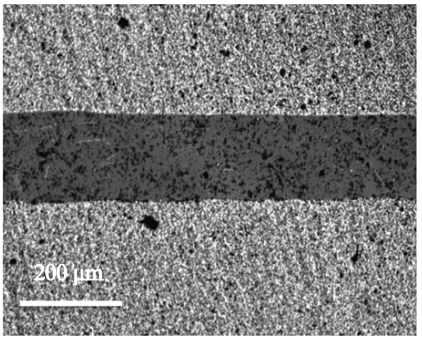

Figure 2 Cross section of the joint imaged using a confocal laser scanning microscope.

Four points bending tests

Four point bending tests revealed that the strength of the joints depended on the laser manufacturing process. The fracture load of the sample ranged from 80N to 180N. Figure 3 shows the morphology of the fractured surface after the four point bending test. The presence of areas free of glass indicates that the joints break mainly at the glass- silicon carbide interface. All the fractured surfaces presented similar morphology at the end of the four point bending test.

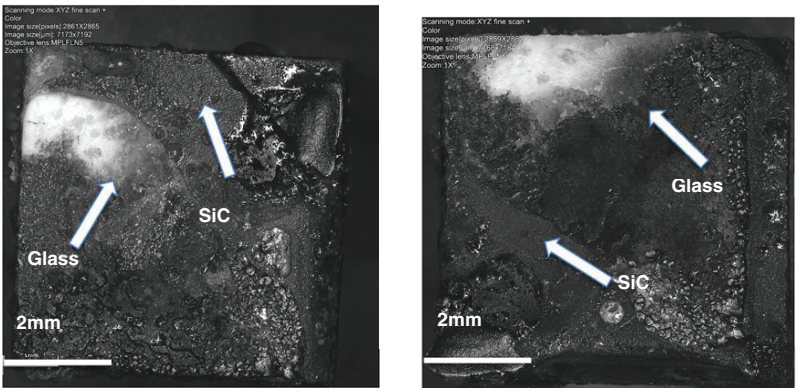

Figure 3. Confocal laser scanning microscope images of the morphology of the fractured joint after four point bending test: (A) right side; (B) left side.

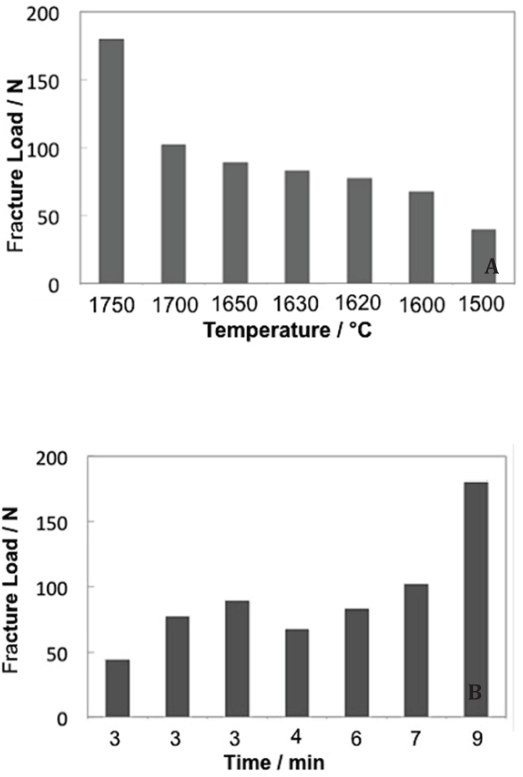

Figure 4. Dependence of fracture load to joining temperature and time: (A) Fracture Load vs. temperature; (B) Fracture Load vs. time.

The diagrams in Figure 4 show that the strength of the joints is strictly dependent on the laser processing parameters. Joints irradiated for longer time and generated at high temperature had higher strength.

Autoclave Tests

SiC disks joined using the braze CA survived the autoclave tests. Figure 5 shows that the images of the cross sections of the joints before and after the autoclave test. The images show that after the autoclave test there is a lack of porosity in the joint microstructure, which is uniform and compact. The joints are also firmly attached to the silicon carbide disks. The specimens had negligible levels of weight loss. These results were confirmed at higher magnification by secondary electron and backscattered electron images of the cross section of the joint after autoclave test shown in Figure 6.

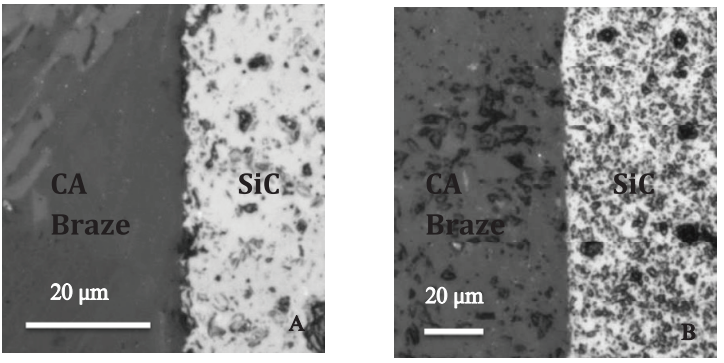

Figure 5. Confocal laser scanning microscope image of the cross section of the joint: (A) before autoclave test; (B) after autoclave test carried out at 500 °C, at a pressure of 25 MPa and at flow rate of a 1 m/s with oxygen content of 25 ppm for seven days.

CONCLUSIONS

Joints of Al_2O_3-CaO glass produced through laser brazing have a uniform and compact microstructure with good adhesion to the silicon carbide substrate. The joint maintains good properties after autoclave test. Therefore the glass Al_2O_3-CaO material is suitable to be used as joining material for laser brazing of silicon carbide.

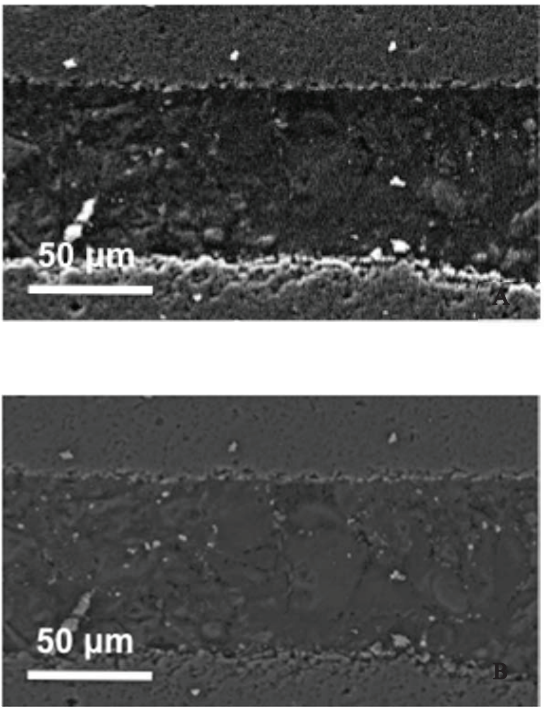

Figure 6. Secondary electron and backscattered electron images of the cross section of the joint after autoclave test carried out at 500 °C, at a pressure of 25 MPa and at flow rate of 1 m/s with oxygen content of 25 ppm for seven days; a) secondary electron (SEM) image; b) backscattered electron (BSE) image.

REFERENCES

1) Slack, G.A. Journal of Applied Physics 1964, 35, 3460
2) Barret, D.L.; Campbell, R.B. Journal of Applied Physics 1973
3) Ford, L.H.; Hibbert, N.S.; Martin, D.G. Journal of Nuclear Materials 1973, 45, 139 149.
4) Snead, L.L.; Nozawa, T.; Katoh, Y.; Byun, T.; Kondo, S.; Petti, D.A. Journal of Nuclear Materials 2007, 371, 329 377.

5) Zinkle, S.J.; Terrani, K.A.; Gehin, J.C.; Ott, L.J.; Snead, L.L. Journal of Nuclear Materials 448 (2014) 374 –379
6) Hallstadius, L.; Johnson, S.; Lahoda, E. Progress in Nuclear Energy 57 (2012) 71-76
7) Katoh, Y.; Snead, L.L.; Cheng, T.; Chunghao, S.; Lewis, W.D.; Koyanagi, T.; Hinoki, T.; Henager, C. H. Jr.; Ferraris, M. Journal of Nuclear Materials 448 (2014) 497-511
8) Henager Jr, C.H.; Kurtz, R.J. Journal of Nuclear Materials 417 (2011) 375–378
9) Henager Jr, C.H.; Shin, Y.; Blum, Y.; Giannuzzi, Y.L.A.; Kempshall B.W.; Schwarz, S.M. Journal of Nuclear Materials 367–370 (2007) 1139–114

CORROSION-RESISTANT TERNARY CARBIDES FOR USE IN HEAVY LIQUID METAL COOLANTS

K. Lambrinou[1], T. Lapauw[1,2], A. Jianu[3], A. Weisenburger[3], J. Ejenstam[4], P. Szakálos[4], J. Wallenius[4], E. Ström[5], K. Vanmeensel[2] and J. Vleugels[2]
[1] SCK•CEN, Boeretang 200, 2400 Mol, Belgium
[2] Department of Materials Engineering, KU Leuven, Kasteelpark Arenberg 44, 3001 Leuven, Belgium
[3] Karlsruhe Institute of Technology (KIT), Institute for Pulsed Power and Microwave Technology, Hermann-von-Helmholtz-Platz 1, 73644 Eggenstein-Leopoldshafen, Germany
[4] KTH Royal Institute of Technology, 10044 Stockholm, Sweden
[5] Sandvik Materials Technology, 73427 Hallstahammar, Sweden

ABSTRACT

A primary concern in the development of accelerator-driven systems (ADS) with liquid lead-bismuth eutectic (LBE) spallation target and Gen-IV lead-cooled fast reactors (LFRs) is the compatibility of the candidate structural steels with the heavy liquid metal (HLM) coolant. In the accelerator-driven system MYRRHA, the envisaged primary coolant is liquid LBE, a potentially corrosive environment for various nuclear grade steels. The inherent LBE corrosiveness is the driving force behind diverse research incentives aiming at the development of corrosion-resistant materials for specific applications. Due to their superb corrosion resistance in contact with liquid LBE, MAX phases are currently being assessed as candidate materials for the construction of pump impellers suitable for MYRRHA and Gen-IV LFRs. In the case of the MYRRHA nuclear system, the pump impeller will be called to operate reliably at ~270°C in contact with moderately-oxygenated (concentration of dissolved oxygen: $[O] \geq 7\times10^{-7}$ mass%), fast-flowing LBE (LBE flow velocity: $v \approx$ 10-20 m/s locally on the impeller surface). Selected MAX phases are currently being screened with respect to their capability of meeting the targeted material property requirements, especially the enhanced erosion resistance requested by this particular application. This work gives a state-of-the-art overview of the processing and characterisation of selected MAX phases that are screened as candidate structural materials for the MYRRHA pump impeller. All considered MAX phases were produced via a powder metallurgical route and their performance was assessed by various mechanical tests in air/vacuum and corrosion/erosion tests in liquid LBE.

INTRODUCTION

The development and reliable operation of heavy liquid metal-cooled nuclear reactors rely greatly on the compatibility of the structural and cladding steels with the primary HLM coolant of these nuclear reactor systems. In the case of the MYRRHA nuclear system, the envisaged primary HLM coolant is the liquid LBE, a potentially corrosive environment for nuclear grade steels, such as the 316L and DIN 1.4970 austenitic stainless steels that are currently considered as the MYRRHA candidate structural and cladding steels, respectively. An undesirable LMC effect that might manifest itself when such steels come into direct contact with liquid LBE is dissolution corrosion. Dissolution corrosion is typically manifested by the loss of the highly-soluble-in-LBE steel alloying elements, such as Ni, Mn and Cr, and the progressive penetration of LBE into the base steel. This results in the gradual thinning of the steel component and the compromise of its mechanical integrity, which is a great concern for thin-walled components (e.g. cladding or heat exchanger tubes). Moreover, the transfer of the highly-soluble austenite stabilizers Ni and Mn into the liquid LBE results in the ferritization of the dissolution-affected zone and an associated change in the steel mechanical properties during service in the LBE

environment. Dissolution corrosion is promoted at high temperatures and/or when the amount of dissolved oxygen in the liquid LBE is low, whereby the formation of a protective oxide scale on the steel surface is either suppressed or significantly decelerated. Therefore, the currently-envisaged LMC mitigation approaches in MYRRHA involve moderate operating temperatures and active oxygen control, i.e. maintaining the concentration of dissolved oxygen in the LBE coolant within a certain range that ensures the formation of a protective oxide on the steel component surfaces while preventing the oxidation of the LBE itself. Since the operation of nuclear reactors cannot exclude the occurrence of high-temperature accidental transients or even the temporary loss of active oxygen control, it would be very desirable to (eventually) have the opportunity to use materials without the intrinsic susceptibility of most nuclear steels towards dissolution corrosion. $M_{n+1}AX_n$ (MAX) phases is a family of materials that possesses a range of very appealing properties, one of which appears to be their inherent resilience to undesirable LMC effects such as dissolution corrosion. In order to explore the great potential of MAX phases for novel nuclear systems, emerging research initiatives revolve around investigating the possible use of these materials for specific applications, such as the pump impeller for MYRRHA and Gen-IV LFRs. The current MYRRHA design foresees the following nominal service conditions for the pump impeller: T ≈ 270°C, [O] ≥ 7×10^{-7} mass% (lowest recommendable LBE oxygen concentration) and v ≈ 10-20 m/s locally on the impeller surface. The expected fast neutron irradiation dose on the pump impeller is very low (< 1 dpa), due to the fact that the impeller is situated close to the reactor bottom and at a distance of 3.3 m from the centre of the reactor core in the current reactor design, so the anticipated activation of this component is limited during the impeller lifetime. In terms of neutron activation, Hoffman et al.[1] have already demonstrated that the neutron activation of commercially-available materials Ti_3SiC_2, Ti_3AlC_2 and Ti_2AlC was similar to SiC and three orders of magnitude lower than Alloy 617, two leading candidate materials for use in next generation reactor components. Moreover, Tallman et al.[2] reported on the effects of neutron irradiation up to 0.1 dpa on polycrystalline Ti_3AlC_2, Ti_2AlC, Ti_3SiC_2 and Ti_2AlN. Interestingly, these authors observed a MAX phase-specific irradiation tolerance, which varied between the enhanced dissociation of Ti_3AlC_2 into TiC, the lesser dissociation of Ti_3SiC_2 and Ti_2AlN into TiC and TiN, respectively, and the remarkable stability of Ti_2AlC. The authors were not able to fully understand the response of these select MAX phases to neutron irradiation, thus emphasising the need for an in-depth study of irradiation-induced defects as well as for data acquired at higher irradiation doses.

In order to use MAX phases as structural materials for specific components, such as the MYRRHA pump impeller, the material mechanical properties are very important; apart from a satisfactory erosion resistance, specific design-related requirements for both flexural strength and fracture toughness must also be met in the foreseen service conditions (e.g. ambient temperature, LBE environment). Different mechanical properties of various MAX phases have already been determined at room temperature in air or inert atmosphere[3]. However, limited information is available on the high-temperature mechanical properties of these ceramics and, in particular, on the effect of the HLM environment on the high-temperature mechanical properties of interest. Since Hu et al.[4] reported that Nb_4AlC_3 exhibits an exceptional temperature stability, maintaining its strength up to 1400°C, this promising MAX phase was produced by spark plasma sintering (SPS) in this work. The mechanical performance of the produced Nb_4AlC_3 was compared with that of the widely-known, commercially-available MAXTHAL 211® (nominally Ti_2AlC) and MAXTHAL 312® (nominally Ti_3SiC_2) materials produced by Sandvik, Sweden.

SPS was also chosen to produce the other MAX phases addressed in this work (i.e. Ti_2AlC, Ti_3AlC_2, $(Ti,Nb)_2AlC$, Nb_2AlC, Nb_4AlC_3 and Ti_2SnC). SPS is a rapid sintering technique that allows the in-situ formation and densification of the targeted MAX phase. During SPS, a direct current is pulsed through the punch/die system and, if conductive, through the powder compact.

Due to the electrical resistivity of the punch/die/powder system, heat is generated due to the Joule effect. This selective heating mechanism facilitates a high heating rate, fast densification and high cooling rate, resulting in short sintering cycles and limiting the grain growth of the synthesised product[5]. Production by SPS has already been reported in literature for various MAX phases, e.g. Ti_3SiC_2, Ti_2AlC, Ti_3AlC_2 and Nb_4AlC_3[6,7]. Recently, Ti_2SnC, which was previously synthesised by reactive hot pressing[8], has also been added to this list[9]. An in-depth analysis of the synthesis process of Ti_2SnC by SPS is also presented in this work.

EXPERIMENTAL

Production of MAX Phases by SPS

Elemental powders (Table I) were mixed in the stoichiometric ratio of the target MAX phase with a slight excess of the A-element (Al or Sn) due to the elemental loss accompanying melting. Dry powder mixing for 24 h in a polypropylene jar was done using a Turbula multidirectional mixer.

Table I: Elemental starting powders used for MAX phase synthesis.

Elemental powder	Supplier	Particle size (μm)	Purity (%)
Al	AEE	< 5	> 99
C	Asbury	< 5	> 99
Nb	CBMM	< 40	> 98
Sn	AEE	< 5	> 99
Ti	Chemetall	< 8	> 99

The powder mixture was transferred in a graphite die and uniaxially cold-pressed at 30 MPa. The green powder compact dimensions were: ∅ 30 mm, height ~5 mm. The heating rate was initially 100°C/min but decreased to 50°C/min close to the final sintering temperature, which was imposed by the target MAX phase and varied in the 1300-1650°C range. At the final sintering temperature, the pressure increased from 5 MPa to 50 MPa, where it was held for a dwell time of 5 min.

The reaction sequence that occurs during MAX phase processing can be quite complex and must be understood, so as to assess whether a particular sintering cycle will yield a single-phase MAX ceramic or a (specific) phase mixture. In this work, the sintering process of Ti_2SnC will be used as a test case, so as to show the complexity of the reaction sequence that may characterize MAX phase processing. In order to follow closely the reaction sequence, the Ti_2SnC sintering cycle was interrupted at 500, 700, 900, 950 and 1100°C and the produced materials were characterized. The final sintering temperature varied in the 1200-1400°C range and was set at intervals of 50°C; an additional specimen was sintered at 1325°C. The total sintering cycle took less than 30 min. The temperature in the SPS facility (FCT-Systeme, HP D 25, Frankenblick, Germany) was controlled by an optical pyrometer for temperatures higher than 400°C. Sintering was performed under vacuum (~100 Pa) and the displacement of the upper piston was constantly monitored. More information on the employed die/punch setup is provided elsewhere[10].

Density, Microstructure and Mechanical Properties of MAX Phases

The Archimedes principle was used to determine the density of the sintered ceramics. The phase assembly of the cross-sectioned discs was determined by X-ray diffraction (XRD), using a diffractometer (Seifert 3003 diffractometer) equipped with a Cu K_α radiation source (operating conditions: 40 kV, 40 mA). The XRD patterns were measured in the 10-60° 2θ range with a step size of 0.02° at 2 sec per step. The microstructural evolution during sintering was studied on

metallographically-polished material cross-sections by means of a scanning electron microscope (SEM, JEOL, JSM-6610LV) equipped with an energy dispersive X-ray spectrometer (EDS, Bruker, Quantax EDS).

Dense MAXTHAL 211® (primarily $Ti_{n+1}AlC_n$) and MAXTHAL 312® (primarily Ti_3SiC_2) ceramics were provided by Sandvik, Sweden. These commercially-available materials were compared to Nb_4AlC_3 produced by SPS. The phase composition was determined by XRD and was quantified by Rietveld refinement using the TOPAS Academic software. Flexural strength and fracture toughness were determined using rectangular bars (4×3×45 mm^3) that were first shaped by electrical discharge machining (EDM) and subsequently ground to their final dimensions. Flexural strength was determined by 4-point bending in accordance with ASTM standard C1161-13[11], while fracture toughness was determined by the single edge V-notch beam (SEVNB) technique (notch depth: 1 mm, notch tip radius: 20 µm). The impulse excitation technique (IET, IMCE, Belgium) was used to determine the room-temperature dynamic elastic properties, according to ASTM standard C1259-08[12]. The temperature dependence of the Young's modulus was assessed by means of a dedicated IET set-up (IMCE HTVP 1750, IMCE, Belgium) equipped with automated impulse excitation and vibration detection devices. This measurement was performed in vacuum, at a heating rate of 5°C/min up to 1400°C (maximum allowable T).

Liquid Metal Corrosion Testing of MAX Phases

The liquid metal corrosion (LMC) resistance of various MAX phases was assessed by means of a simultaneous screening exposure of selected MAX phases to static LBE. The exposed MAX phase materials included: (i) MAXTHAL 211® and MAXTHAL 312® provided by Sandvik, Sweden, and (ii) experimental grades of Ti_2AlC, Ti_3AlC_2, $(Nb,Ti)_2AlC$, Nb_2AlC and Nb_4AlC_3 produced in the lab by SPS. A metallographically-polished cross-section of these materials was studied by SEM/EDS prior to testing, so as to have an idea of the microstructure of the non-exposed materials. After the SEM/EDS investigation, the specimens were fastened with Mo wires on graphite plates with their polished side facing the LBE bath (~5 kg of LBE); both Mo and graphite were chosen to suspend the specimens in the bath due to their low solubility in liquid LBE. The LMC test was performed in a stainless steel capsule with an alumina (Al_2O_3) inner liner, which prevented the direct contact of the steel container walls with the LBE bath, thus preventing its contamination with highly-soluble-in-LBE steel alloying elements that would have definitely occurred under the aggressive exposure conditions. The temperature and oxygen concentration during the test were monitored with a thermocouple (type K) and an electrochemical oxygen sensor (Bi/Bi_2O_3 reference electrode). The MAX materials were exposed for 3501 h at 500°C to static LBE with a very low concentration of dissolved oxygen ([O] < 2.2×10^{-10} mass%). The exposure conditions were chosen deliberately in order to evaluate the resistance of MAX phases to dissolution corrosion.

Erosion Testing of MAX Phases

The CORELLA (Corrosion Erosion Test Facility for Liquid Lead Alloy) test facility at KIT, Germany, has been recently refurbished to achieve the targeted HLM flow velocities and will be systematically used to assess the erosion resistance of selected MAX phases in contact with fast-flowing LBE. The CORELLA facility, which is presented in Figure 1, is able to achieve rotation speeds >1000 rpm and average HLM (Pb/LBE) flow velocities v > 10 m/s[13,14]. The HLM temperature, the oxygen partial pressure of the conditioning gas phase and the respective oxygen content in the HLM are controlled and monitored. Measurement of the local flow velocities at the specimen location cannot be performed, but visual inspection of the flowing HLM suggests a highly turbulent flow field in the specimen vicinity. Typical specimen dimensions are 60×15×1.5

mm^3; the specimens are fixed in the test tank using a tailor-made holding plate. The adequate performance of the refurbished CORELLA facility for erosion testing in liquid lead alloys was demonstrated earlier by testing simultaneously MAXTHAL 312® together with other materials, such as surface-modified T91 ferritic/martensitic (f/m) steel using the GESA treatment[15] prior to testing. The exact exposure conditions during this test in liquid Pb were: 480°C, 100 h, v ≈ 10 m/s and [O] < 10^{-9} mass%[13]. As may be seen in Figure 2, the observed erosion damages on both materials were very limited, probably also due to the short test duration.

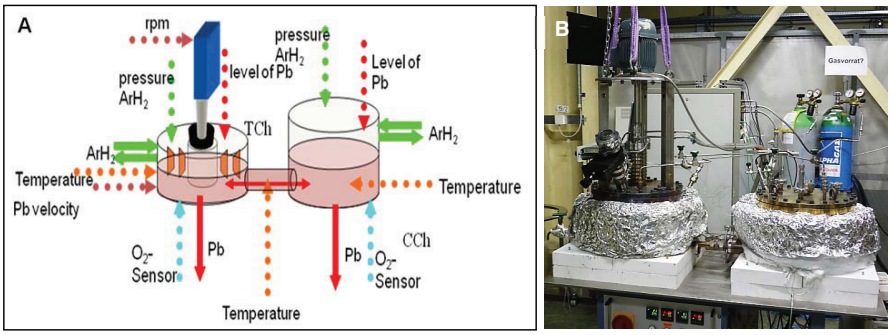

Figure 1. (A) Schematic representation of the CORELLA facility, which comprises two tanks: the HLM conditioning tank (right) and the testing tank (left). The test specimens are fixed on a holding plate that is attached to the rotating axis, the speed of which is measured and controlled during testing. Temperature and concentration of dissolved oxygen in the HLM are monitored by means of a thermocouple and an electrochemical oxygen sensor, respectively. The HLM oxygen concentration is controlled by bringing the HLM in equilibrium with the appropriate (oxidizing or reducing) conditioning gas phase. (B) Picture of the CORELLA facility.

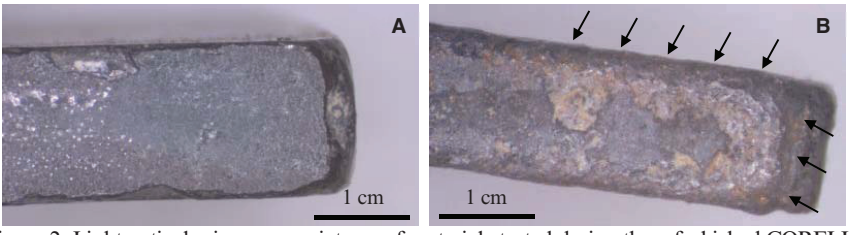

Figure 2. Light optical microscopy pictures of materials tested during the refurbished CORELLA performance qualification test (i.e. liquid Pb, 100 h, 480°C, [O] < 10^{-9} mass%, v ≈ 10 m/s). (A) MAXTHAL 312®: specimen side facing the Pb flow. The erosion assessment was challenging, due to the non-perfectly flat surface of the pristine specimen. Erosion damages – if any – were limited. (B) T91 f/m steel surface-modified with the GESA treatment: specimen side facing the Pb flow. Erosion damages were only observed on the small specimen facets (arrows) that have not been subjected to the surface modification treatment.

After the successful qualification test of the refurbished CORELLA facility, two tests were performed in liquid LBE; these tests targeted the MYRRHA pump impeller service conditions, i.e. ~270°C, v > 10 m/s, [O] ≥ 7×10^{-7} mass% and tried to compare the erosion resistance of the commercially-available MAXTHAL 211® and MAXTHAL 312® materials with that of other

candidate structural materials, such as the 316L austenitic stainless steel. The actual test conditions were: (i) 500 h, 300°C, [O] < 10^{-8} mass%, v ≈ 8 m/s in the 1st test, (ii) 500 h, 300°C, [O] = 10^{-6} – 10^{-5} mass%, v ≈ 8 m/s in the 2nd test. At the end of the 1st test, the specimens were first visually examined and then surface profilometry measurements were done on representative specimen areas by means of white light interferometry. After the assessment of erosion damages, the specimens were re-introduced in the CORELLA facility and the 2nd test was performed.

RESULTS AND DISCUSSION

Production of MAX Phases by SPS

The reaction sequence during Ti_2SnC synthesis could be reconstructed based on the evolution of the monitored parameters (i.e. temperature and upper piston displacement) during sintering (Figure 4), the XRD patterns (Figures 3 and 5) and the SEM/EDS analysis results (Figure 6) of the produced ceramics. It was found that the first intermetallic phase that formed at 500°C was Ti_2Sn_3, while increasing the sintering temperature resulted in the formation of Ti_6Sn_5 and Ti_5Sn_3 (Figure 3). According to the Ti-Sn equilibrium phase diagram[16], this phase evolution shows the formation of intermetallics with progressively higher Ti-content.

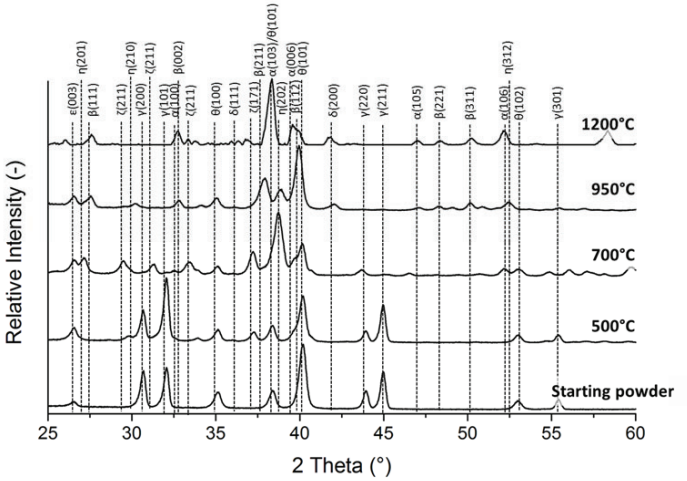

Figure 3. XRD patterns of the ceramics produced by the interrupted Ti_2SnC sintering cycles at 500, 700, 950 and 1200°C. α: Ti_2SnC, β: Ti_5Sn_3, γ: Sn, δ: TiC, ε: C, ζ: Ti_2Sn_3, η: Ti_6Sn_5, θ: Ti.

Based on the above, the following reaction steps can be suggested:

At 230°C:	$Sn(s) \rightarrow Sn(l)$	(1)
At 500°C:	$2Ti(s) + 3Sn(l) \rightarrow Ti_2Sn_3(s)$	(2)
At 600°C:	$8Ti(s) + 5Ti_2Sn_3(s) \rightarrow 3Ti_6Sn_5(s)$	(3)
At 800°C:	$3Ti_6Sn_5(s) + 7Ti(s) \rightarrow 5Ti_5Sn_3(s)$	(4)
At 950°C:	$Ti(s) + xC(s) \rightarrow TiC_x(s)$	(5)
At 1100°C:	$(3\text{-}x)C(s) + TiC_x(s) + Ti_5Sn_3(s) \rightarrow 3Ti_2SnC(s)$	(6)

In general, four main steps can be considered for the production of M_2AX phases: (1) melting of the A-element (T_m(Sn) = 230°C and T_m(Al) = 660°C, where T_m is the A-element melting point), (2) formation of M-A intermetallics, (3) formation of MX_x and (4) synthesis of M_2AX. For $M_{n+1}AX_n$ with n > 1, an additional reaction between MX_x and M_2AX produces the targeted MAX phase, e.g. Nb_4AlC_3:

$$2NbC(s) + Nb_2AlC(s) \rightarrow Nb_4AlC_3(s) \quad (7)$$

The four-step synthesis of Ti_2SnC can be also observed in the evolution of the piston displacement curve of Figure 4. At 230°C, the melting of Sn induces a first shrinkage to the powder compact. Although the pyrometer only starts measuring at 400°C, a part of the shrinkage is still captured due to the high initial heating rate. The expansion after the formation of the Ti_2Sn_3 intermetallic can be attributed to the lower density of the later-forming intermetallics Ti_6Sn_5 and Ti_5Sn_3. No noticeable piston displacement is found during the formation of TiC_x around 950°C. Finally, the small shrinkage at higher temperatures (>1000°C) can be attributed to the formation of Ti_2SnC and the completion of the solid-state sintering of the powder compact.

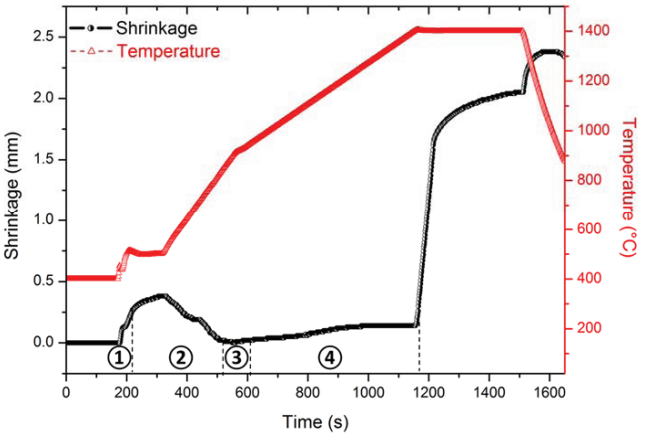

Figure 4. Temperature and shrinkage evolution as a function of time for the Ti_2SnC sintering cycle at 1400°C. Regions (1)–(4) can be correlated to the reaction sequence during sintering.

The XRD patterns in Figure 5 show the effect of the final sintering temperature, while the SEM micrographs of Figure 6 facilitate the further investigation of the reaction path. Four main phases are identified in the 1200-1400°C range: Ti_2SnC, Ti_5Sn_3, Sn and TiC_x. With increasing temperature, the peak intensities of Ti_5Sn_3 decrease and the presence of Ti_2SnC becomes more pronounced. This is in good agreement with reaction (6). This evolution is further supported by Figure 6, which shows a strong reduction in the amount of the bright, Sn-rich Ti_5Sn_3 phase as the sintering temperature increases from 1200°C (Figure 6A) to 1400°C (Figure 6D).

At 1325°C, no more Ti_5Sn_3 is observed in the XRD pattern, but Sn peaks appear (Figure 5). The microstructure at 1325°C is shown in Figure 6C: it mainly consists of micrometer-sized Ti_2SnC grains (grey matrix phase) with Sn (bright phase) and TiC_x (dark phase) at the grain boundaries. This phase mixture indicates the onset of the dissociation of Ti_2SnC, according to the following reaction[17]:

$$Ti_2SnC(s) \rightarrow 2TiC_{0.5}(s) + Sn(l) \quad (8)$$

The optimal density was achieved at 1325°C, with a value of 6.28 g/cm^3 or 98.7% of the theoretical density (= 6.36 g/cm^3)[17], assuming the material consists of pure Ti_2SnC. However, a minimum amount (<3 wt%) of TiC_x is found at 1325°C. At lower temperatures, the secondary TiC_x carbides cluster together around C-rich areas, providing nucleation sites for the Ti_2SnC grains. These observations are in good agreement with the suggested reaction sequence for Ti_2SnC. Similar processes have been observed during the production of other MAX phases, whereby a MX_x-rich region facilitates the nucleation of MAX grains, consuming the A-rich intermetallic regions. The final product often consists of elongated MAX phase grains, sometimes separated by a thin A-rich layer.

At temperatures above 1325°C, the amount of TiC_x increases again as a result of the decomposition of Ti_2SnC, as shown by the dark phase in Figure 6D. For other MAX phases, an increase in the synthesis temperature does not result in degradation but in transformation into a $M_{n+1}AX_n$ phase with a higher n stoichiometry, as observed with Ti_2AlC and Nb_2AlC that transform into Ti_3AlC_2 and Nb_4AlC_3, respectively. However, in the case of Ti_2SnC, Ti_3SnC_2 did not form.

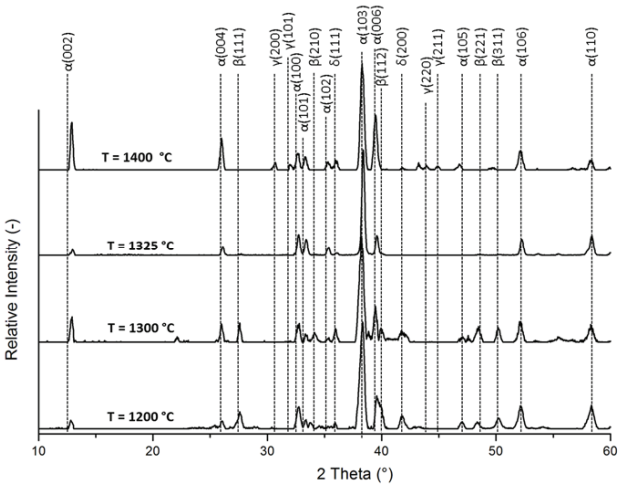

Figure 5. XRD patterns of the Ti_2SnC ceramics sintered at a final sintering temperature in the 1200-1400°C range under a pressure of 50 MPa. α: Ti_2SnC, β: Ti_5Sn_3, γ: Sn, δ: TiC.

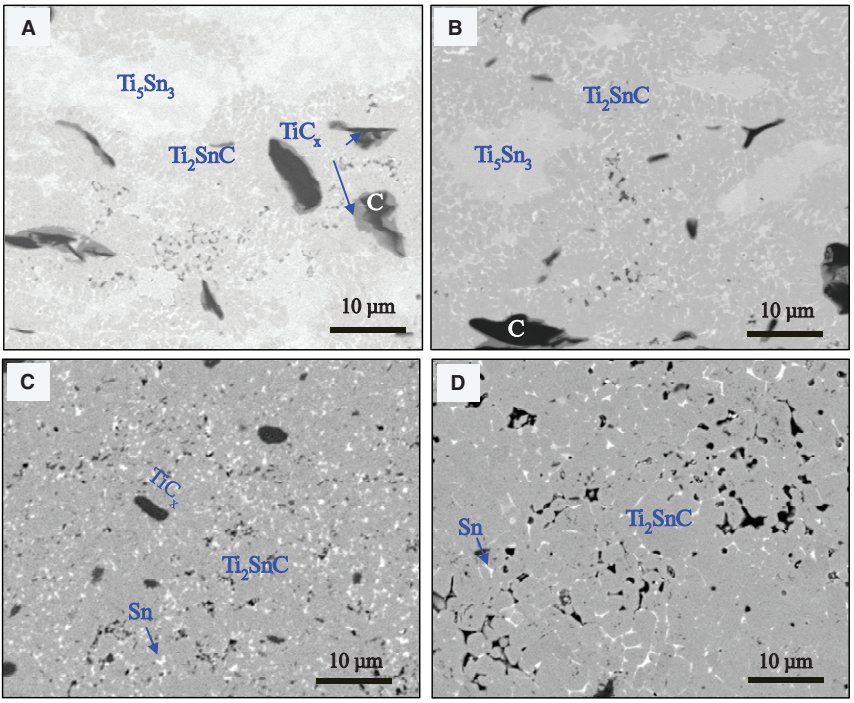

Figure 6. Backscattered electron (BSE) detector images of cross-sectioned Ti_2SnC ceramics sintered at (A) 1200°C, (B) 1300°C, (C) 1325°C and (D) 1400°C. The brightest areas are Sn-rich.

Mechanical Properties of MAX Phases

A comparative summary of the properties of MAXTHAL 211®, MAXTHAL 312® and Nb_4AlC_3 is presented in Table II. MAXTHAL 211® is a mixture of Ti_2AlC and Ti_3AlC_2 with a small amount (7 wt%) of $TiAl_3$, MAXTHAL 312® mainly consists of Ti_3SiC_2 with a small amount (10 wt%) of TiC, while a small amount of Al_2O_3 (2 wt%) is present in Nb_4AlC_3. The microstructure of these three ceramics is shown in Figures 7A-7C. As may be seen, the location of the secondary phases differs in the three materials: in MAXTHAL 211®, $TiAl_3$ forms intergranularly between the elongated MAX grains, as a result of the synthesis process explained in the previous section. In MAXTHAL 312® and Nb_4AlC_3, TiC and Al_2O_3 are randomly distributed in the material. The Al_2O_3 particles (black specs in Figure 7C), in particular, are observed within the Nb_4AlC_3 grains, indicating that they were present prior to the formation of Nb_4AlC_3.

The fracture surfaces of the three ceramics are shown in Figures 7D-7F. Remarkably, there is a significant grain size difference between the two commercially-available MAX phases (50-100 µm for MAXTHAL 211®; 5-10 µm for MAXTHAL 312®). Such microstructural differences are directly reflected in the mechanical properties (i.e. flexural strength and fracture toughness) of the MAX phase-based materials (Figure 8). The Hall-Petch relationship, which is applicable to MAX phases[18], partially explains the higher flexural strength of MAXTHAL 312® as compared

to MAXTHAL 211®. Obviously, other factors may also affect the flexural strength, e.g. porosity, intrinsic strength of each phase and phase purity. A combination of the latter two is presumably responsible for the higher strength of Nb_4AlC_3 as compared to MAXTHAL 312®.

Table II: Comparison of the properties of MAXTHAL 211®, MAXTHAL 312® and Nb_4AlC_3.

Property	MAXTHAL 211®	MAXTHAL 312®	Nb_4AlC_3
Phase composition (wt%)	55 Ti_2AlC + 38 Ti_3AlC_2 + 7 $TiAl_3$	90 Ti_3SiC_2 + 10 TiC	98 Nb_4AlC_3 + 2 Al_2O_3
ρ (g/cm³)	4.02 (98% ρ_{th})	4.42 (98% ρ_{th})	6.89 (99% ρ_{th})
Grain size (μm)	50-100	5-10	10-20
E (GPa)	265 ± 4	325 ± 5	340 ± 5
G (GPa)	112 ± 2	137 ± 3	137 ± 2
ν	0.17	0.19	0.23
T (°C) where $E/E_{RT} = 0.75$ (*)	± 1250	± 1300	> 1400
$H_{v,3kg}$ (GPa)	3.2 ± 0.5	3.8 ± 0.4	3.7 ± 0.3
σ_{4pt} (MPa)	210 ± 12	404 ± 44	573 ± 39
K_{IC} (MPa·m$^{1/2}$)	6.2 ± 0.2	4.8 ± 0.2	6.6 ± 0.1

(*) Measurement done in vacuum

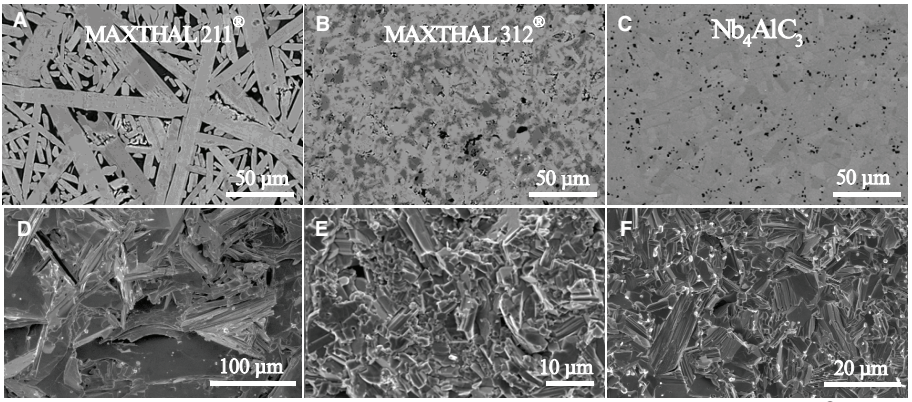

Figure 7. BSE detector images of polished cross-sections of (A) MAXTHAL 211®, (B) MAXTHAL 312® and (C) Nb_4AlC_3. Secondary electron detector images of the fracture surface of (D) MAXTHAL 211®, (E) MAXTHAL 312® and (F) Nb_4AlC_3.

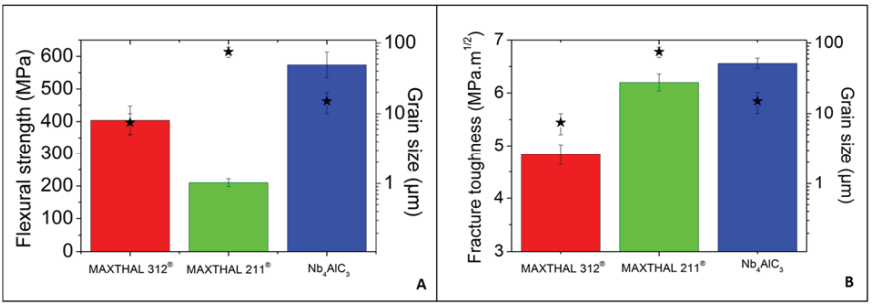

Figure 8. Comparison of the flexural strength (A) and fracture toughness (B) of MAXTHAL 211®, MAXTHAL 312® and Nb_4AlC_3. The stars indicate the average grain size of the different MAX phase materials. The error bars show the standard deviation of all properties.

With respect to the fracture toughness of MAX phases, an increase in grain size is usually associated with a higher fracture toughness. This observation was made by Hu et al.[19] for V_2AlC and was confirmed for other MAX phases. The larger grains in MAXTHAL 211® can thus justify the higher fracture toughness of this material as compared to MAXTHAL 312®. The phase purity and intrinsic properties of Nb_4AlC_3 might account for its high fracture toughness.

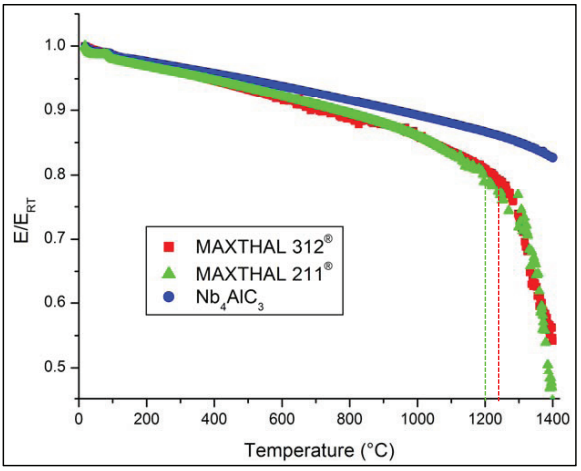

Figure 9. The normalized Young's modulus (E/E_{RT}) as function of temperature measured by IET. The vertical lines indicate the temperature where $E/E_{RT} = 0.75$. Since the E/E_{RT} of Nb_4AlC_3 has not been reduced to 0.75 at 1400°C, the superior thermal stability of this MAX phase is obvious.

The temperature dependence of the normalized Young's modulus (E/E_{RT}) for the three MAX phase-based materials is shown in Figure 9. The decrease in Young's modulus as a function of the ambient temperature is clearly indicative of the material thermal stability. In this respect, the superiority of Nb_4AlC_3 is shown by the fact that the Young's modulus decreases linearly up to 1400°C, in agreement with the observations of Hu et al.[4]. For the commercially-available materials, MAXTHAL 312® exhibits a higher temperature stability than MAXTHAL 211®, since

the decrease in their Young's modulus deviates from linearity around 1250°C and 1200°C, respectively. Differences in thermal stability are associated with the intrinsic thermal stability of the constituent phases; therefore, Ti_3SiC_2 appears to be a better candidate for high-temperature structural applications than Ti_2AlC.

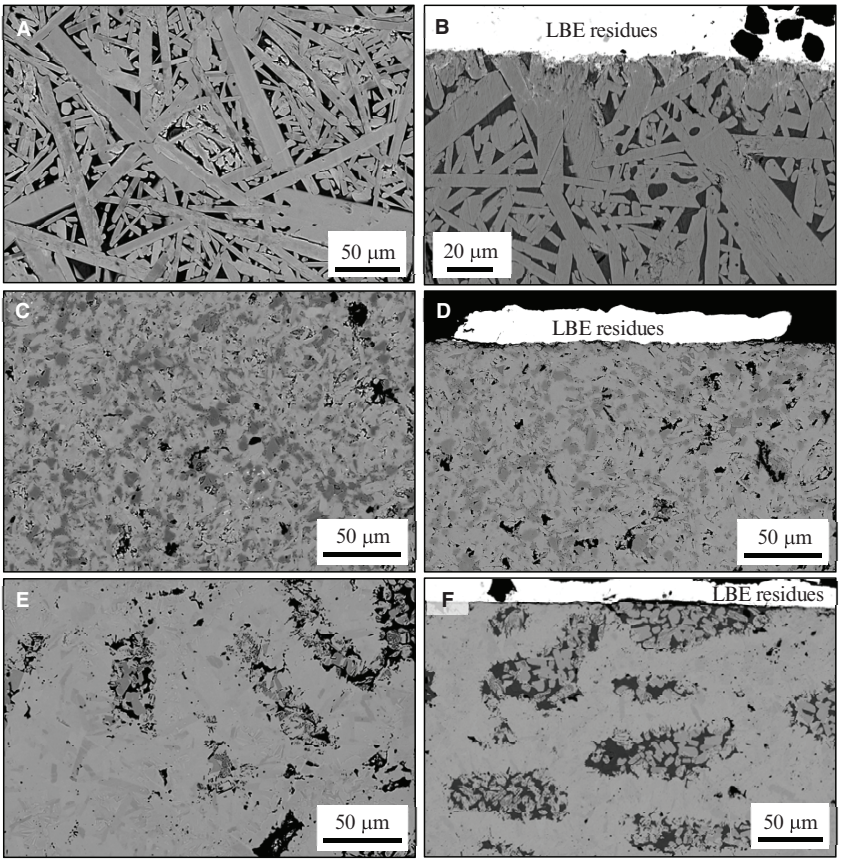

Figure 10. BSE detector images of polished cross-sections of the non-exposed MAX materials (A) MAXTHAL 211®, (C) MAXTHAL 312® and (E) Nb_4AlC_3. BSE images of the same MAX material cross-sections after exposure for 3501 h at 500°C to poorly-oxygenated ([O] < 2.2×10^{-10} mass%) static LBE: (B) MAXTHAL 211®, (D) MAXTHAL 312® and (F) Nb_4AlC_3.

Liquid Metal Corrosion Testing of MAX Phases

All MAX phase-based materials demonstrated a superb LMC resistance in contact with static LBE, despite the very aggressive exposure conditions (3501 h, 500°C, [O] < 2.2×10^{-10} mass%). The SEM micrographs in Figure 10 illustrate the lack of interaction between liquid LBE and three of the exposed MAX materials, i.e. MAXTHAL 211® (Figure 10B), MAXTHAL 312® (Figure 10D) and Nb_4AlC_3 (Figure 10F). The same figure also presents SEM micrographs of the

pristine microstructure of the three MAX materials MAXTHAL 211® (Figure 10A), MAXTHAL 312® (Figure 10C) and Nb_4AlC_3 (Figure 10E); no changes in the material microstructure were observed after the exposure to liquid LBE. Heinzel et al.[20] has previously reported the satisfactory LMC resistance of Ti_3SiC_2 after an exposure of 3000 h at 550°C to moderately-oxygenated ([O] = 10^{-8} – 10^{-6} mass%) static LBE. In the work by Heinzel et al.[20], a thin (< 1 μm) TiO_2 (rutile type) was observed on the surface of the exposed material, allowing one to attribute the LMC resistance of Ti_3SiC_2 to the formation of a protective oxide. However, the very low oxygen concentration ([O] < 2.2×10^{-10} mass%) that was maintained in the LBE bath during the test reported in this work has effectively suppressed the formation of a similar oxide, thus pointing out the inherent chemical stability of all exposed MAX phases in liquid LBE. The undoubted LMC resistance of MAX phases in lead alloys (Pb/LBE) at high temperatures and very low concentrations of dissolved oxygen makes these materials very promising candidate materials for use in MYRRHA and Gen-IV LFRs, as they have the potential to sustain high-temperature accidental transients accompanied by loss of active oxygen control.

Erosion Testing of MAX Phases

At this stage, only the erosion damages from the 1st test in the CORELLA facility have so far been assessed. Visual inspection of the tested MAX specimens concluded that their surface was quite clean with almost no adhering LBE residues, a further confirmation of the limited chemical interaction between MAX phases and liquid LBE. Only one spot on the MAXTHAL 211® specimen showed signs of erosion damages: the surface profile of the damaged area (Figure 11B) is compared to that obtained from the pristine specimen (Figure 11A). Figures 11C and 11D show the surface profiles of the MAXTHAL 312® specimen before and after testing, respectively. One may clearly see that MAXTHAL 211® has suffered a non-negligible material loss at this specific location in contrast to MAXTHAL 312®, which appears unaffected. The eroded spot on the MAXTHAL 211® specimen was found on the surface facing the impacting LBE flow, which is the facet typically exhibiting erosion damages in a wide variety of materials. The more severe erosion damages observed on MAXTHAL 211® might be associated with the inferior phase purity of this material in comparison to MAXTHAL 312®, since different material constituent phases are characterised by distinctly different properties (hardness, stiffness) and their interfaces might constitute weak material areas enabling the mechanical removal of sizeable grain aggregates by the LBE flow.

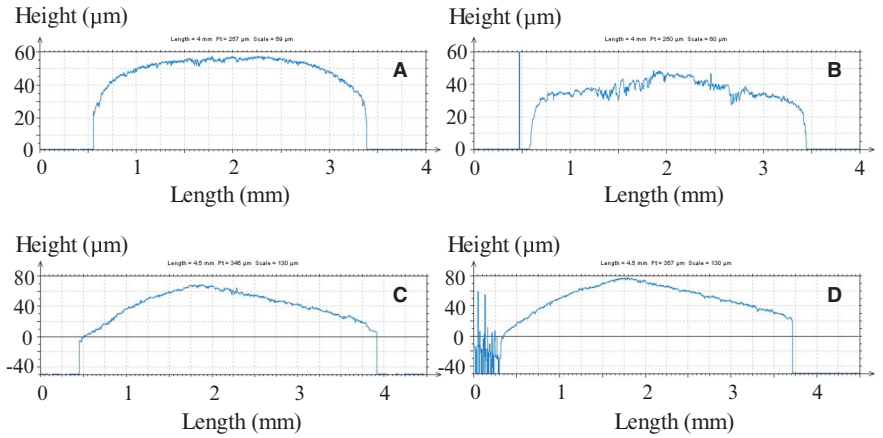

Figure 11: Surface profilometry on test specimens before and after the 1st erosion test. (A) Pristine and (B) exposed MAXTHAL 211® specimen, with LBE residues, at the location of enhanced erosion damage. (C) Pristine and (D) exposed MAXTHAL 312® specimen, with LBE residues, showing no signs of erosion damage.

CONCLUSIONS

This work provides an overview of ongoing research activities dedicated to the exploration of the potential of selected MAX phases as candidate structural materials for certain nuclear applications, such as the pump impeller for the MYRRHA nuclear system. Before concluding whether a specific MAX phase is suitable for such an application, several steps must be taken: (i) the processing must be closely-controlled, so as to produce stable phase mixtures that optimize specific mechanical properties (e.g. strength, fracture toughness, etc.) required by the end (pump impeller) application, (ii) the produced ceramics must be subjected to rigorous mechanical testing both in inert and LBE environments, so as to detect possible environment-assisted degradation effects (e.g. liquid metal embrittlement), (iii) the produced ceramics must be tested in contact with static liquid LBE in a variety of exposure conditions (i.e. T, [O], time), so as to understand their LMC behavior, (iv) the produced ceramics must be tested in contact with fast-flowing liquid LBE in MYRRHA-relevant conditions, so as to assess their erosion resistance; if the latter is found inadequate, post-processing heat treatments of the machined component in a judiciously-chosen atmosphere might be adopted, so as to form durable phases on the component surface that will (presumably) increase the component lifetime in service. Moreover, this work discusses some of the challenges involved in the processing, mechanical testing, liquid metal corrosion and erosion testing of selected MAX phases.

ACKNOWLEDGMENTS

The research leading to these results is partly funded by a PhD grant No. 131081 of the Agency for Innovation by Science and Technology (IWT), Flanders, Belgium, partly by the European Atomic Energy Community's (Euratom) Seventh Framework Programme FP7/2007-2013 under grant agreement No. 604862 (MatISSE project) and falls within the framework of the EERA (European Energy Research Alliance) Joint Programme on Nuclear Materials.

REFERENCES

[1] E. N. Hoffman, D. W. Vinson, R. L. Sindelar, D. J. Tallman, G. Kohse, and M. W. Barsoum, "MAX phase carbides and nitrides: Properties for future nuclear power plant in-core applications and neutron transmutation analysis," *Nuclear Engineering and Design* ***244***, 2012, 17-24.
[2] D. J. Tallman, E. N. Hoffman, E. N. Caspi, B. L. Garcia-Diaz, G. Kohse, R. L. Sindelar, and M. W. Barsoum, "Effect of neutron irradiation on select MAX phases," *Acta Materialia* ***85***, 2015, 132-143.
[3] M. W. Barsoum, and M. Radovic, "Elastic and mechanical properties of MAX phases," *Annual Review of Materials Research* ***41***, 2011, 195-227.
[4] C. Hu, F. Li, L. He, M. Liu, J. Zhang, J. Wang, Y. Bao, J. Wang, and Y. Zhou, "In Situ Reaction Synthesis, Electrical and Thermal, and Mechanical Properties of Nb_4AlC_3," *Journal of the American Ceramic Society* ***91***, 2008, 2258-2263.
[5] S. G. Huang, K. Vanmeensel, and J. Vleugels, "Powder synthesis and densification of ultrafine B_4C-ZrB_2 composite by pulsed electrical current sintering," *Journal of the European Ceramic Society* ***34***, 2014, 1923-1933.
[6] C. Hu, Y. Sakka, H. Tanaka, T. Nishimura, and S. Grasso, "Low temperature thermal expansion, high temperature electrical conductivity, and mechanical properties of Nb_4AlC_3 ceramic synthesized by spark plasma sintering," *Journal of Alloys and Compounds* ***487***, 2009, 675-681.
[7] W. B. Zhou, B. C. Me, J. Q. Zhu, and X. L. Hong, "Synthesis of high-purity Ti_3SiC_2 and Ti_3AlC_2 by spark plasma sintering (SPS) technique," *Journal of Materials Science* ***40***, 2005, 2099-2100.
[8] Y. C. Zhou, H. Y. Dong, X. H. Wang, and C. K. Yan, "Preparation of Ti_2SnC by solid-liquid reaction synthesis and simultaneous densification method," *Materials Research Innovations* ***6***, 2002, 219-225.
[9] T. Lapauw, K. Vanmeensel, K. Lambrinou, and J. Vleugels, "Rapid synthesis and elastic properties of fine-grained Ti_2SnC produced by spark plasma sintering," *Journal of Alloys and Compounds* ***631***, 2015, 72-76.
[10] K. Vanmeensel, A. Laptev, J. Hennicke, J. Vleugels, and O. Van der Biest, "Modelling of the temperature distribution during field assisted sintering," *Acta Materialia* ***53***, 2005, 4379-4388.
[11] ASTM Standard C1161-13, 2013, "Standard test method for flexural strength of advanced ceramics at ambient temperature," ASTM International, West Conshohocken, PA 19428-2959, USA, 2013, www.astm.org.
[12] ASTM Standard C1259-08, 2008, "Standard test method for dynamic Young's modulus, shear modulus, and Poisson's ratio for advanced ceramics by impulse excitation of vibration," ASTM International, West Conshohocken, PA 19428-2959, USA, 2008, www.astm.org.
[13] Final Report Summary – LEADER (Lead-cooled European Advanced Demonstration Reactor) Project, pp. 11-12; http://cordis.europa.eu/result/rcn/147643_en.html; LEADER project reference: 249668, funded under: FP7-EURATOM-FISSION.
[14] M. Kieser, H. Muscher, A. Weisenburger, A. Heinzel, and G. Müller, "Liquid metal corrosion/erosion investigations of structure materials in lead cooled systems: Part 1," *Journal of Nuclear Materials* ***392***, 2009, 405-412.
[15] V. Engelko, B. Yatsenko, G. Müller, and H. Bluhm, "Pulsed electron beam facility (GESA) for surface treatment of materials," *Vacuum* ***62***, 2001, 211-216.
[16] H. Okamoto, "Sn-Ti (Tin-Titanium)," *Journal of Phase Equilibria and Diffusion* ***31***, 2010, 202-203.
[17] M. W. Barsoum, G. Yaroschuk, and S. Tyagi, "Fabrication and characterization of M_2SnC (M = Ti, Zr, Hf and Nb)," *Scripta Materialia* ***37***, 1997, 1583-1591.

[18] M. W. Barsoum, "Mechanical Properties: Ambient Temperature" in "MAX Phases-Properties of Machinable Carbides and Nitrides," Wiley-VCH Verlag GmbH & Co., 2013, pp. 307-361.
[19] C. Hu, L. He, M. Liu, X. Wang, J. Wang, M. Li, Y. Bao, and Y. Zhou, "In Situ Reaction Synthesis and Mechanical Properties of V_2AlC," *Journal of the American Ceramic Society* **91**, 2008, 4029-4035.
[20] A. Heinzel, G. Müller, and A. Weisenburger, "Compatibility of Ti_3SiC_2 with liquid Pb and PbBi containing oxygen," *Journal of Nuclear Materials* **392**, 2009, 255-258.

DEVELOPMENT OF ACCIDENT TOLERANT SIC/SIC COMPOSITE FOR NUCLEAR REACTOR CHANNEL BOX

Shoko Suyama, Masaru Ukai, Masayuki Uchihashi, Hideaki Heki, Satoko Tajima, Kazunari Okonogi and Kazuo Kakiuchi
Power Systems Company, Toshiba Corporation
Yokohama, Japan

ABSTRACT

SiC/SiC composites have been attracting attention as a high-temperature structural material because of its stability at high temperatures. Recently, SiC/SiC composites have become one of the candidates for the nuclear material used in accident tolerant fuel (ATF). In the case of the incident at the Fukushima Daiichi nuclear power plant, the oxidation of metallic components in a high-temperature steam induced the generation of hydrogen and caused the explosion of the reactor building. In order to reduce the probability of hydrogen explosion in the future, SiC/SiC composites are seriously being considered for their effectiveness and accident tolerant properties, and Toshiba has started the designing of material compositions for applying the SiC/SiC composites to the channel box and fuel cladding of light water reactors (LWR). For the material design of the channel box, Toshiba has showed the effectiveness of a channel box of a laminate structure that is composed of CVI-SiC/SiC and CVD-SiC with an interface layer.

INTRODUCTION

Fiber-reinforced ceramic matrix composites are some of the most promising candidate materials for high-temperature structural applications. SiC matrix composites are being considered for use as a material of gas turbine hot section parts. Namely, using SiC matrix composites will make it possible to improve the gas turbine efficiency through the reduction of cooling air. The fabrication processes for SiC matrix composites are typically divided into four types; chemical vapor infiltration (CVI), precursor impregnation and pyrolysis (PIP), melt infiltration (MI) and sintering such as hot pressing (HP). The development of low oxygen content SiC fibers (Hi-Nicalon TypeS, Tyranno SA), which show excellent high-temperature stability, enables various matrix consolidation processes at high-temperatures. Dense matrices are preferable in order to protect the fiber and interface layer from severe oxidation environments[1-3].

In the case of the incident at the Fukushima Daiichi nuclear power plant, the oxidation of metal components in a high-temperature steam induced the generation of heat and hydrogen, and caused the core meltdown and the explosion in the reactor building. In order to prevent such a severe accident from occurring again, nuclear power plants in Japan are taking numerous measures to ensure the strengthening of the defense in depth. In order to enhance the safety, the application of fiber-reinforced ceramic matrix composites to structural materials is seriously

being considered for their effectiveness and their accident tolerant properties, because their chemical and mechanical stability is higher than that of metals at high-temperatures. Recently, SiC/SiC composites have become one of the candidates for the core material used in accident tolerant fuel (ATF) [4-6].

IBIDEN Co., Ltd., The University of Tokyo, Tohoku University, Nuclear Fuel Industries, Ltd. and Toshiba Corporation started a joint project in 2012 to develop SiC/SiC composites for accident tolerant core materials that can be used in the current light water reactors, as well as the next generation light water reactors. Toshiba has started the designing of material compositions for applying the SiC/SiC composites to the channel box and fuel cladding of light water reactors (LWR). The material design of the channel box is described and discussed in this paper.

SELECTION OF ACCIDENT TOLERANT CORE MATERIAL

Several studies have already been started on the development of accident tolerant fuel[4-6]. In regards to metals, Toshiba selected stainless steel as a candidate for the ATF material. The other metals which can withstand high-temperatures have a disadvantage concerning neutron absorption. In regards to ceramics, Toshiba selected SiC ceramics due to its greater advantages, mainly the mechanical and thermal properties at high-temperatures.

Table 1 shows comparisons of the properties between zirconium alloys and the two selected candidates. Stainless steels are well-researched materials, thus the hurdles for their practical use are fairly lower than SiC ceramics. Nevertheless, there are still some issues which include the relatively large neutron absorption cross-section, and the low melting-temperature compared with zirconium alloys. Stress corrosion cracking (SCC) properties are one of disadvantage for any stainless steels [4].

Table 1. Comparison of properties for Zirconium alloy and the two selected candidates

	Zirconium alloys	Stainless steels	SiC ceramics
Melting temperature	ca. 2100K	ca.1700K	ca. 3000K
Phase transformation temperature	ca. 1100K (α to β)	ca. 900K (sensitization)	ca. 2500K (β to α)
High temperature oxidation	High rate	Low rate	Extremely low rate
Stress corrosion cracking (SCC) with water	No	Almost yes	No
Thermal neutron absorption cross section	0.18b	2.9b	0.08b
Stability against irradiation	Good	Good	Good

SiC ceramics show greater advantages compared with zirconium alloy from every aspect in Table 1, except for manufacturability and mechanical properties[7, 8]. Its small neutron absorption cross-section and stability at high-temperatures are attractive from the viewpoint of practical use in ATF material. Therefore, SiC ceramics have high-potential as a material to

enhance both the economic efficiency and safety of nuclear fuel. In order to improve the mechanical properties, such as the fracture toughness, it is necessary for applying a SiC matrix composite which is reinforced with SiC fiber.

SELECTION OF SIC MATRIX FABRICATION PROCESSES FOR ACCIDENT TOLERANT CORE MATERIAL

The basic material properties of SiC/SiC composites are significantly affected by the SiC matrix fabrication processes. The fabrication processes for SiC matrix composites is typically divided into four types; sintering, chemical vapor infiltration (CVI), precursor impregnation and pyrolysis (PIP), melt infiltration (MI) and sintering such as hot pressing (HP). Table 2 shows a comparison of the advantages and issues of the SiC matrix fabrication processes[2, 3].

Table 2. Comparison of advantages and issues of SiC matrix fabrication processes

Process	Advantages	Issues
Chemical Vapor Infiltration (CVI)	✓ Lower process temp. ✓ High purity matrix ✓ Suited to thin-walled structures	● Porous matrix ● Scalability ● Expensive
Precursor Impregnation and Pyrolysis (PIP)	✓ Lower process temp. ✓ Complex shape capability ✓ Scalability	● Amorphous matrix ● Porous matrix
Melt Infiltration (MI)	✓ Lower process temp. ✓ Dense matrix ✓ Complex shape capability	● Containing residual Si ● Scalability
Sintering	✓ Dense matrix	● Higher process temp. ● Needs high-pressure and/or sintering-additives ● Shape capability and scalability

The CVI process forms a high purity, stoichiometric and polycrystalline SiC matrix at lower process temperatures with the availability of SiC fibers. Generally, the densification rate is slow, and leaves an unavoidable final porosity with the infiltration of a gas phase SiC precursor. This forms a porous SiC matrix which has a relatively high residual porosity (>10 vol %)[9-11]. Some issues with the infiltration of a gas phase precursor are the limited scaling and shaping capability of the manufacturing. However, this process is suitable for forming thin-walled structures, such as the channel box (rectangular structure with thin walls) and the cladding tubes (cylindrical structure with thin walls).

The PIP process uses a SiC-precursor polymer to impregnate a fiber preform. In this process, several impregnation-pyrolysis cycles are necessary. The amorphous SiC matrix leaves a significant amount of residual porosity (>10 vol %). Therefore, since both the elastic limit and

the beginning strength of the micro-cracking of the matrix are considerably low, it would be difficult to apply it to structural material.

The MI is one of the processes suitable for forming a dense matrix without firing shrinkage[2-3]. The densification provides improved SiC matrix thermo-mechanical properties relative to composites consisting of CVI and PIP. The elastic limit and the beginning of the micro-cracking of the matrix are high enough to apply it to structural material. However, some residual Si remains (>5 vol %). Therefore, it would decrease the resistance to hydrothermal corrosion.

Sintering is a process of forming a SiC matrix composite by sintering aids and/or high pressure, such as hot pressing (HP) and hot isostatic pressing (HIP). Higher process-temperatures showed significant strength degradation of the SiC fiber. Moreover, this process has some issues with the shape capability and scalability, and has little practical application.

In the next step, Toshiba benchmarked the SiC matrix fabrication processes at lower process-temperatures in regards to the requirements for the channel box (Table 3).

Table 3. Benchmark comparison of SiC matrix fabrication processes for channel box

Priority	Requirements	CVI	PIP	MI
1	Corrosion resistance during normal operation	Issue	No	No
1	Irradiation resistance during normal operation	Good	No	Issue
1	High-temperature tolerance under severe conditions	<1700K	<1400K	<1600K
4	Mechanical properties during normal operation	Issue	Issue	Good
4	Mechanical properties during earthquakes	Issue	Issue	Issue
4	Thermal shock resistance under severe conditions	Issue	Issue	Issue
4	Fabrication of both thin-walled and elongated models	Issue	Good	Issue
8	Thermal properties during normal operation	Issue	No	Good
9	SiC matrix fabrication cost	Issue	Good	Good

The first priority in satisfying the requirements for the channel box was the corrosion and irradiation resistance during normal operation and the high-temperature tolerance under severe conditions which for example, would not work in a cooling water system. This shows thermal resistance temperature due to the SiC matrix fabrication processes. Furthermore, oxidation resistance in steam atmosphere is needed for the accident tolerant channel box. The CVI process is an effective method of satisfying the requirements for the channel box among these processes. The CVI process shows high-temperature tolerance (<1700K) because of its high purity, stoichiometric and polycrystalline SiC matrix. The corrosion resistance during normal operation is currently under examination.

However, the CVI process has some issues, such as the mechanical properties during

normal operation, mechanical properties during earthquakes, thermal shock resistance under severe conditions, fabrication of both thin-walled and elongated models, thermal properties during normal operation and the SiC matrix fabrication cost. Toshiba has discussed the material design of the channel box in order to satisfy the mechanical properties of the CVI-SiC/SiC composites.

MATERIAL DESIGN OF CHANNEL BOX

The channel box requires mechanical properties for protection of the fuel assemblies. In addition to the existing safety standards, under the new regulations, a heat resistance of over 1473K is required for the channel box during severe accidents. Thus, the new regulations require that the channel box is able to withstand seismic loads, as well as heat resistance up to 1473K or higher. As the channel box is being designed for use under these conditions, the application of these materials was carefully reviewed.

Toshiba has started designing the material compositions for applying the CVI-SiC/SiC composites to the channel box. In the case of an accident, the channel box is required to withstand seismic loads and heat resistance up to 1473K or higher. None of the CVI-SiC/SiC structures have sufficient enough strength properties during both normal operation and earthquakes. Therefore, Toshiba has settled on using a laminate structure composed of CVI-SiC/SiC and CVD-SiC with an interface layer, which combines the mechanical properties of the CVD-SiC's strength and the CVI-SiC/SiC's toughness[11-14]. The interface layer could be incorporated into both the load baring capacity of the CVD-SiC, and the large damage tolerance of the CVI-SiC/SiC. Figure 1 shows a cross-section view of a channel box using this material design concept. The rectangular structure with thin walls is composed of three layers, the CVD-SiC, interface layer and CVI-SiC/SiC.

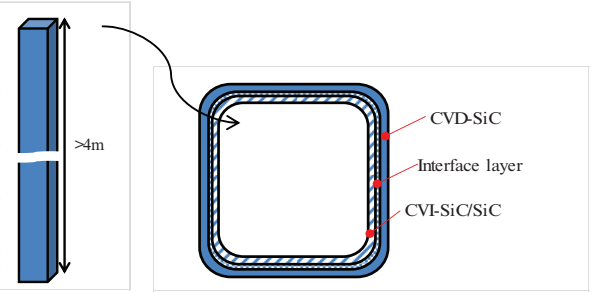

Figure 1. Cross-section view of channel box using this material design

Figure 2 shows the consideration of the stress-strain curves for a hybrid structure. The hybrid structure, comprised of layers of CVD-SiC and CVI-SiC/SiC with an interface layer, has a fracture strength that is initially high, and also shows a high fracture energy[13-14]. As for the design of the SiC hybrid material, it is very important that the thickness of each layer is optimized based on the properties of the CVD-SiC, CVI-SiC/SiC and interface layer, including the reversible structure shown in figure 1.

This hybrid structure will provide not only the mechanical properties required under the new regulations, but also cost performance of the channel box due to the SiC fiber reduction, etc.

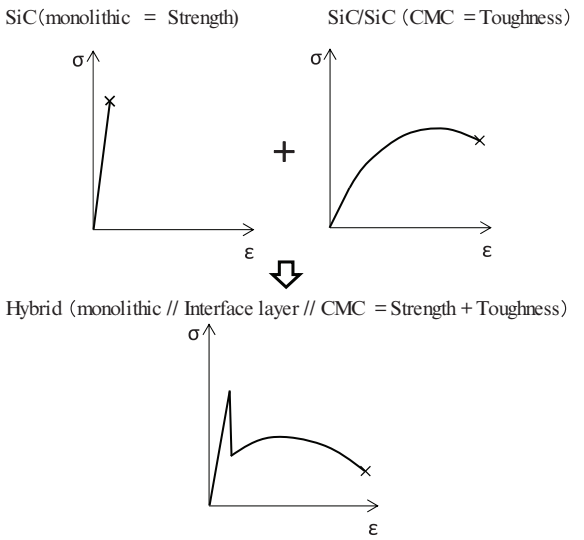

Figure 2. Consideration of stress-strain curve for hybrid structure[14]

SUMMARY

Toshiba and the collaborating partners started a joint project to develop a SiC/SiC composite for accident tolerant core materials. Toshiba has started the designing of material compositions for applying the SiC/SiC composites to the channel box and fuel cladding of light water reactors (LWR). First, the material design of the channel box was described and discussed in this paper.

For the material design of the channel box, Toshiba benchmarked the SiC matrix fabrication processes with the requirements of the channel box. The sintering process temperature affected the strength degradation of the SiC fiber. Concerning the matrix, standard PIP and MI processes are not effective in both hydrothermal corrosion and irradiation resistance. As a result of the benchmarking, the CVI process was selected for the fabrication process of the

SiC/SiC composite for the channel box due to its corrosion and irradiation resistance during normal operation, and high-temperature tolerance under severe conditions. It was suitable for forming a thin-walled structure, such as the channel box (rectangular structures with thin walls) and the cladding tubes (cylindrical structures with thin walls).

Next, Toshiba showed the effectiveness of a channel box of a laminate structure composed of CVI-SiC/SiC and CVD-SiC with an interface layer, in order to improve the mechanical properties during normal operation and earthquakes. The hybrid structure of the CVD-SiC and CVI-SiC/SiC is considered to be attractive in achieving the mechanical properties, because both the load baring capacity of the CVD-SiC and the large damage tolerance of the CVI-SiC/SiC could be incorporated into the channel box. As for its design, optimization of the microstructure, including the interfacial properties of the hybrid structure should be made in order to obtain the accident tolerant properties. The main focus of this structure is to understand the design variables based on the micro-failure process of the CVD-SiC and CVI-SiC/SiC hybrid structures.

In the future, we will design the material composition for the fuel cladding for applying the SiC/SiC composite.

ACKNOWLEDGEMENT

The authors would like to express our sincere gratitude to Prof. Takashi Goto of Tohoku University, Prof. Yutaka Kagawa of The University of Tokyo, Mr. Shinji Ono of NFI, Mr. Syuichi Kubo and Mr. Takashi Takagi of Ibiden for their cooperation in the the CVD/CVI technology development project.

REFERENCES

[1] T. Kameda, S. Suyama, Y. Itoh, K. Nishida, I. Ikeda, T. Hijikata, T. Okamura, Ceramic gas turbine component development and characterization: Progress in ceramic gas turbine development, Vol.2, Chapter 18: *Development of Continuous Fiber-Reinforced Reaction Sintered Silicon Carbide Matrix Composite for Gas Turbine Hot Parts Application*, pp.331-351, (2003).

[2] S.SUYAMA, Y.ITOH, *Evaluation of Microstructure for SiC/SiC Composites using Mercury Intrusion Method, Ceramic Engineering & Science Proceedings*, Vol.30, Issue 3, (1999) pp.181-189.

[3] S.SUYAMA, T.KAMEDA, Y.ITOH, *Evaluation of Microstructure for SiC/SiC Composites, Int. J. of Materials and Product Technology*, Vol. 16, Nos. 1/2/3, (2001) 232-238.

[4] K. Kitano, M. Ukai, T. Kubo, *Development of innovative material for nuclear reactor core with enhanced safety*, TopFuel 2013, Charlotte, North Carolina, September 15-19, 2013, pp.936-942.

[5] C. Sauder, A. Michaux, G. Loupias, P. Billaud, J. Braun, *Assessment of SiC/SiC cladding for LWRs*, TopFuel 2013, Charlotte, North Carolina, September 15-19, 2013, pp.951-956.

[6] Y. Katoh, K.A. Terrani, L.L. Snead, *Systematic Technology Evaluation Program for SiC/SiC*

Composite-based Accident-Tolerant LWR Fuel Cladding and Core Structures, ORNL/TM-2014/210, May, 2014.

[7] T. Narushima, T. Goto, Y. Iguchi, T. Hirai, *High-Temperature Oxidation of Chemically Vapor-Deposited Silicon Carbide in Wet Oxygen at 1823 to 1923K*, J. Am. Ceram. Soc., 73, 12, 3580-3584, (1990).

[8] T. Goto, *High-Temperature Oxidation Behavior of Chemical Vapor Deposited Silicon Carbide*, J. Ceram. Soc. Jpn., 110, 10, 884-889, (2002).

[9] Y. Kagawa: *Thermal Shock Damage of Two-Dimensional Woven SiC Fiber-Reinforced SiC Matrix Composite*, Composite Science and Technology, Vol.57 (1997), 607-611.

[10] Y. Kim Y, S. Zhu S and Y. Kagawa "*Effectiveness of Surface Composite Layers on Impact Resistance of Brittle Materials*," Advances Engineering Materials, 6(1-2), (2004), 71-73.

[11] A.G.Evans, et.al, *On crack path selection and the interface fracture energy in bimaterial systems*, Acta metal. 37, pp.3249-54 (1989).

[12] M. A. Mattoni, et.al, *Effects of matrix porosity on the mechanical properties of a porous-matrix, all-oxide ceramic composite*, J. Am. Ceram. Soc., 84, pp.2594-602 (2001).

[13] R. J. Kerans, et.al, *Interface design for Oxidation-resistant ceramic composites*, J. Am. Ceram. Soc., 85, 2599-632 (2002).

[14] Y. Kagawa, Tokyo University, Japan, Personal communication, 2014.

THERMAL DIFFUSIVITY MEASUREMENT OF CURVED SAMPLES USING THE FLASH METHOD

J. Zhang, H.E. Khalifa, C. Deck, J. Sheeder, C. A. Back
General Atomics, P.O. Box 85608, San Diego, CA 92186-5608

ABSTRACT
The flash method is a commonly used technique to measure the thermal diffusivity of solid samples. In this work, the classical flash method for planar specimen geometries was extended to measure cylindrically curved plates. The temperature evolution of the back surface of the cylindrical plate was calculated and a measurement method incorporating a geometrical correction concept was evaluated. Experimental measurements of the thermal diffusivity on a set of planar and curved lead samples were used to confirm the validity of the method and determine the geometrical correction factor. Additional thermal diffusivity measurements on a set of stainless steel samples at temperatures from room temperature to 800°C demonstrated that the geometric factor is not a function of sample temperature. This method was then applied to obtain thermal diffusivity measurements for curved composite materials. Silicon carbide fiber reinforced, silicon carbide matrix composites (SiC-SiC) are being developed for nuclear fuel cladding applications, where thermal conductivity is an important design parameter. Due to the fabrication process, the structure and fiber geometry of curved composite samples may differ from planar samples, and as a consequence, data from planar samples may not be representative and direct measurement of curved composite specimens is critical. Composite structure was found to have a strong effect on the thermal diffusivity measurements for prototypical SiC-SiC cladding tubes.

1. INTRODUCTION

The flash method was introduced by Parker and coworkers [1] and is widely acknowledged as a standard for thermal diffusivity measurements of solid materials. The principle of this technique considers a burst of energy emanating from a pulsed laser that is absorbed on the front face of the opaque slab, and results in homogeneous heating. The relative temperature increase on the rear face of the sample is measured as a function of time by an IR or other detector, and the thermal diffusivity is obtained by computing the time corresponding to the half maximum of the temperature rise (t1/2). For adiabatic conditions, the thermal diffusivity, is a function of h, the sample thickness, and $t_{1/2}$, the time at 50% of the temperature increase and is given by the equation:

$$\alpha = 0.1388\frac{h^2}{t_{1/2}} \quad (1)$$

With the flash method, the challenging measurement of the absolute quantity of laser energy absorbed by the sample and of the resulting absolute temperature increase is replaced with more accurate and direct measurements of time and relative temperature increase via the detector voltage.

In Parker's initial work, no heat loss and an infinitely narrow flash pulse width were assumed. Since then much work has been done on heat loss and pulse width corrections. Cowan [2] improved the flash measurement method by considering heat loss at high temperatures. Clark and Taylor [3] studied the effect of radiation heat loss on thermal diffusivity measurements. Based on Cowan and Clark and Taylor's results, Koski [4] derived a more general equation including a heat loss factor to predict the rear surface temperature rise with time. Cape and

Lehman [5] had studied the ratio of pulse width to the characteristic thermal response time and generated the correction curves for thermal diffusivity measurement.

The flash method has been mainly restricted to flat samples, and for monolithic materials, the thermal diffusivity would not change as a function of the specimen geometry. However, for composites materials, especially ceramic matrix composites (CMC), the thermal diffusivity will depend on fabrication process and fiber architecture, which can vary depending on sample shape. Therefore, it is necessary to develop a measurement method to measure the thermal diffusivity of non-flat plate. Apinanniz, et al [6] and Salazar et al [7] extended the flash method to measure the radial thermal diffusivity of rods, tubes and spheres. Recently, Salazar et al [8] developed a method to measure the thermal diffusivity of cylindrical and spherical plates. In their work, they assumed an ideal point or line light source pulse uniformly illuminated on OD surface instead of pencil beam pulse. However, in a real measurement, it is difficult to generate a point or line light source and to have uniform illumination on curved plate's surface.

The primary purpose of this work is to develop a method to measure the radial thermal diffusivity of CMC tubes. These SiC-SiC CMC tubes are being developed for use as nuclear fuel cladding in fission reactor, and for this application, the tube diameters will be between 1cm and 2cm, with a wall thickness of roughly 1 mm.

In this work, a flash method was developed to measure cylindrical plate's thermal diffusivity with a regular pencil laser beam as the light energy source. First, a theoretical model was developed to calculate the temperature rise at the rear surface of a cylindrical sample as a function of the radius. Numerical simulations indicate that it is possible to directly use Eq. (1) multiplied by a geometric factor to account for sample geometry. Flash measurements of the back temperature of series of cylindrical lead plates with different radii confirm the validity of the calculation and these results were used to determine the actual geometric factor. Flash measurements of cylindrical steel plates at different temperatures indicate that the geometric factor is not a function of temperature. Finally, thermal diffusivity values were obtained for prototypical SiC-SiC nuclear fuel cladding structures and the effects of tube microstructural features on thermal diffusivity was assessed.

2. THEORETICAL MODEL AND CALCULATION

The theoretical model is developed by first reviewing the calculation of the temperature rise above the ambient of a flat plate illuminated by a brief pencil beam light pulse, and then extending this calculation to the case of cylindrical plate. The purpose of the theoretical calculation is to see if it is possible to directly use Eq. (1) multiplied by a geometric factor to get the thermal diffusivity of cylindrical plate. For this calculation, we will only use the same boundary conditions as used by Parker [1], where heat loss and pulse width effects are not considered. To determine an accurate geometrical factor value, experimental results will be used rather than theoretical results.

Consider an opaque flat plat of thickness h uniformly illuminated by an ideal Dirac pulse with an energy density q. The cross-section of this arrangement is shown in Fig. 1. To obtain the time evolution of this sample, the one-dimensional heat conduction equation must be solved:

$$\frac{\partial^2 T}{\partial x^2} = \frac{1}{\alpha}\frac{\partial T}{\partial t} \tag{2}$$

Boundary conditions:

$$\frac{\partial T(0,t)}{\partial x} = q\delta(t)$$

$$\frac{\partial T(h,t)}{\partial x} = 0$$

Initial condition

$$T(x,0) = 0$$

Solving Eq. 2, gives the temperature rise on the back surface:

$$T(h,t) = T_\infty \left[1 + 2\sum_{n=1}^{\infty}(-1)^n \exp\left(-\frac{n^2\pi^2}{h^2}\alpha t\right)\right] \quad (3)$$

If $t_{1/2}$ is the time required for the back surface to reach half of the final or maximum temperature rise, then, Eq. 3 can be simplified to Eq. 1 and the thermal diffusivity can be determined.

For a sample consisting of a 1.25 mm thick lead plate with thermal diffusivity of 23 mm^2/s, and with an energy density q selected to produce a final temperature rise of 40°C, Eq. 3 will produce the temperature rise plot as shown in Fig. 2.

A Cylindrical plate

Consider a cylindrical plate (a section cut from a tube) with inner radius r_i and outer radius r_o and a width of d. The illumination would be the same as in the flat plate case (Fig. 3). For this sample geometry, the heat conduction equation becomes two dimentional.

$$\frac{\partial^2 T}{\partial r^2} + \frac{1}{r}\frac{\partial T}{\partial r} + \frac{1}{r^2}\frac{\partial^2 T}{\partial \theta^2} = \frac{1}{\alpha}\frac{\partial T}{\partial t} \quad (4)$$

Boundary conditions:

$$\frac{\partial T(r_i,\theta,t)}{\partial r} = q\cos\theta\delta(t)$$

$$\frac{\partial T(r_o,\theta,t)}{\partial r} = 0$$

$$r_o - r_i = h$$

$$\frac{\partial T(r,\theta_e,t)}{\partial \theta} = 0$$

e (edge angle) is determined by

$Sin\,\theta_e = \frac{d}{2r_0}$, where d is the width of the plate.

Symmetric condition:

$$\frac{\partial T(r,0,t)}{\partial \theta} = 0$$

Initial condition

$$T(r,\theta,0) = 0$$

This equation can be solved using numerical methods.

For a 10 cm wide cylindrical plate composed of lead with an outer radius of 5 cm and a thickness of 1.25 mm, the calculated temperature change of the center of the rear surface is shown in Fig. 4.

From Fig. 4, it can be seen that the center temperature increases rapidly initially, but then begins to slowly drop after it reaches the maximum. This is due to heat conduction in direction. This is in contrast to the temperature rise for a flat plate, in which temperature does not drop and the maximum temperature is equal to the final temperature. As a result, for laser flash measurements of curved samples, the maximum temperature must be used instead of the final temperature.

Another important difference between a cylindrical plate and a flat plate is that the rear surface temperature is not uniform in a curved sample, with a higher surface temperature in the center and gradually dropping temperatures towards the edges (Fig. 5). For the actual flash measurement method, the IR detector will not only measure the back surface's center temperature, but will actually measure the average temperature of the entire back surface area visible through the detector's aperture.

Assuming the radius of the aperture is R, the average temperature on back surface can be determined by

$$\overline{T} = \frac{4}{\pi R^2}\int_0^R T(x)\sqrt{R^2 - x^2}\,dx \tag{5}$$

Here, x is the distance from the center.

Based on Eq. 5, the average temperature change on the back surface can be calculated as a function of time and aperture radius. Figure 6 compares the center and average back surface temperatures for a curved lead plate, with the same sample geometry as was used for Fig. 4 and assuming an aperture radius of R = 4 mm.

The value for $t_{1/2}$ (time for the temperature rise to reach half the maximum rise) can be determined based on average temperature vs time curve. Using this approach, the $t_{1/2}$ values for lead plates with thickness of 1.25 mm and different radii of curvature can be calculated and are shown in Fig. 7.

From Fig. 7, $t_{1/2}$ is found to decrease as the plate curvature increases. As a consequence, if the flash method is used to measure thermal diffusivity of cylindrical samples of the same material, the resulting thermal diffusivity value obtained using Eq. 1 will be larger for the higher curvature samples, due to this curvature effect. However, by applying a correction factor based on the sample geometry, it is possible to determine the actual material thermal diffusivity value for curved samples. With this approach, the same regular flash measurement method for flat samples can be used to measure the apparent thermal diffusivity of cylindrical plate, and the relation between the measured value $_m$ and real thermal diffusivity can be given by Eq. 6, where g is a geometrical factor and is a function of the curvature of the sample.

$$\alpha_m = \alpha * g(r) \tag{6}$$

This calculation only uses a simple boundary condition without considering heat loss and pulse width effects. The average temperature on the back surface is also a function of the detecting area, which may vary between different instruments. To account for these conditions, the geometrical factor will be determined from experiment. By measuring samples with different

radii of curvature and flat samples (where the radius of curvature is infinity), the geometrical factor can be determined as:

$$g(r) = \frac{\alpha_{m(r)}}{\alpha(\infty)} \tag{7}$$

3. EXPERIMENTAL AND GEOMETRICAL FACTOR DETERMINATION

In order to validate the theoretical predictions and find the geometrical factor, apparent thermal diffusivities were measured for two sets of samples. Lead plates with different radii of curvature were tested at room temperature to determine the geometrical correction factor, and stainless steel samples with different radii were measured at different temperatures to investigate the effect of temperature on the geometrical factor.

For this work, a NETZSCH LFA LFA 427 laser flash analyzer was used to measure thermal diffusivities, and $t_{1/2}$ was calculated using Eq. 1. The scheme of the experimental setup is shown in Fig. 8. Both flat and curved samples were measured, and the sample physical size was kept constant at 10 mm x 10 mm to fit into the measurement instrument. Cowan model with pulse width correction was chose for data analysis.

Lead sample experimental results

Lead plate specimens were cut from a flat lead sheet to keep the thickness and material properties constant. Four samples were made; one piece was kept flat and the other three were bent into radius of 5, 6 and 7 mm, respectively. Lead was selected due to its high ductility and malleability, which facilitated fabrication of the curved samples. Experimental results for $t_{1/2}$ data have been plotted in Fig. 9 alongside the calculated results, and are in good agreement.

The apparent thermal diffusivity values for the different samples were calculated, and the geometrical factor was determined using Eq. 7. The geometric factor is plotted as a function of curvature in Fig. 10, and these experimental data points were fitted to a curve to give an expression for the geometrical factor as a function of the cylindrical plate's outer radius (r, in mm) as follows:

$$g(r) = \frac{2.4651}{r^2} + \frac{0.1067}{r} + 1 \tag{8}$$

As mentioned above, the geometrical factor is a function of the IR detecting area, and therefore is instrument specific. Once a geometrical factor is determined using this experimental approach, it could be incorporated into the instrument's software, and the thermal diffusivity of a cylindrical sample could be measured directly.

Stainless Steel experimental results

To investigate the effects of temperature on the geometrical factor, an additional set of six stainless steel samples was tested. Five curved test plate samples were cut from 304 stainless steel tubes (with OD of 3/8", ½", 5/8", 1" and 1 ¼") and an additional 304 stainless steel flat plate was used as a control (McMaster-Carr). There was a slight variation in the tube wall thickness, ranging from 1.2mm to 1.25mm for each tube, and the thickness was measured at various locations of each sample to get an average. Thermal diffusivity measurements were taken at temperatures of 25, 200, 400, 600 and 800°C, and the geometrical factors were calculated using Eq. 7. The results are shown in Fig. 11, along with the geometrical factor curve obtained from the lead sample set (Eq. 8).

From these results, the geometric factor for the stainless steel samples was found to follow the geometrical factor given by Eq. 8, and no temperature variation to this factor was observed. The small deviations observed could be caused by either sample-to-sample variation (unlike the lead samples, all these steel samples are not from the same piece of material), or tube wall thickness variations.

4. APPLICATION TO COMPOSITES

In composite materials, especially ceramic matrix composite (CMC) materials, the density and void distribution depends on fabrication process and fiber architecture. If the fabrication process or fiber architecture varies between a flat sample and a curved sample, then the thermal diffusivity of curved composite may not be the same as that of flat composite of nominally the same material. In this work, SiC-SiC composite tube samples were fabricated using chemical vapor infiltration (CVI). Details of this fabrication have been reported previously [9]. This fabrication process produces stoichiometric material with high purity, but residual porosity is trapped within and between reinforcing fiber bundles. The fabrication process, fiber architecture, and resulting residual voids can have a large effect on the final material properties.
Thermal diffusivities of cylindrical SiC-SiC CMC tubes were measured using the laser flash method and applying the geometrical correction factor (Eq. 8), and effects of void size, void volume, and tube microstructure were investigated. X-ray tomography (XCT) was also used to scan all samples to determine void sizes and distributions, and sample densities were obtained by measured mass divided by overall sample volume obtained through XCT scans.

Effect of void volume percentage,

The effects of overall void volume were investigated by measuring two different SiC-SiC composite tube samples with a nominal outer radius of 10 mm and thickness of approximately 1.8 mm. The fiber architecture of both samples was the same; both had a fiber volume fraction of roughly 35%, and void volumes for both were measured using XCT. However, one sample had an additional layer of SiC deposited using chemical vapor deposition; this layer was essentially fully dense and had the effect of reducing the overall void volume fraction (8.7%) in that sample compared to the uncoated sample (12.7%). Because the underlying composite fiber architecture was the same for both samples, the voids sizes of both samples are similar. Cross sections of these two samples showing representative porosity is shown in Fig. 12 and the measured thermal diffusivities of these two samples are plotted in Fig. 13 as a function of temperature. The thermal diffusivity was observed to depend on the sample void volume fraction, with larger void volume fractions reducing thermal diffusivity.

Effect of void size

The effects of void size on thermal diffusivity were explored by comparing measurements on three different SiC-SiC cylindrical samples with an outer radius of 5 mm. The overall void volume fraction in each of these samples was approximately the same (between 9% and 11% void), but due to differences in the fiber architecture, the void sizes varied between samples, and one sample had larger voids and one had smaller voids than are typically observed. Representative void distributions from XCT scans are shown in Fig. 14 and the thermal diffusivities of these three samples are plotted as a function of temperature in Fig. 15. These results indicate that although the three samples have similar density and overall void volumes, the relative size of the voids has a large influence on the thermal diffusivities, with larger voids causing a reduction in the thermal diffusivity.

Effect of the structure on thermal diffusivity

Silicon carbide CMC tubes can also be fabricated incorporating a thicker monolithic SiC layer. This layer can provide an impermeable barrier for gas containment and also affects the tube thermal diffusivity relative to a fully composite tube. To investigate the effect of this structural change, two additional SiC tube samples were fabricated by forming a SiC-SiC composite layer around an inner monolithic SiC tube. The composite layer was fabricated using chemical vapor infiltration, and the monolithic SiC layer was composed of a sintered SiC tube (Hexaloy, St. Gobain). The thickness of the monolithic layers in the two samples was the same, but one sample had a thinner composite layer than the other, and the relative monolith volume fractions for the two samples were 38.1% and 34.7%. The void sizes and volumes were very similar for the two samples; their cross sections are shown in Fig. 16 and the measured thermal diffusivities are plotted in Fig. 17 as a function of temperature.

The monolithic SiC thermal diffusivity was measured at 49.8 mm^2/s at room temperature, which is significantly higher than the SiC-SiC composite due to the significantly lower void volume in the monolithic material. This diffusivity difference is reflected in the experimental results for the combined monolith-composite tube samples, where the sample with the higher monolithic SiC volume fraction was observed to have a higher thermal diffusivity.

5. CONCLUSIONS

In this work, a theoretical model was developed and experimental results were used to demonstrate that the flash measurement method can be directly used to measure thermal diffusivity of cylindrical plate samples without modification of a conventional flash measurement instrument. The effects of sample curvature are accounted for by scaling the measured thermal diffusivity value by a pre-determined geometrical factor, which varies with sample radius. This method is especially useful for thermal diffusivity measurements of curved composite materials, since fabrication and fiber architecture differences can lead to differing properties between flat and curved samples.

This geometric correction approach could also be extended to other shapes beyond flat or curved plates. A ductile, malleable, monolithic material (such as lead) would first be used to make two samples; one planar sample with the desired thickness, and one with the same shape as the target composite sample with the same thickness. By measuring thermal diffusivities of these two samples using the flash method, the geometrical correction factor can be obtained for the geometry of interest. Then, the apparent thermal diffusivity of the target composite samples can be measured under the same test conditions, and the geometrical factor can be applied to account for shape effects and calculate the real value of the material's thermal diffusivity.

REFERENCES

[1] W. J. Parker, R. J. Jenkins, C. P. Butler and G. L. Abbott, J Appl. Phys. **32**, 1679 (1961)
[2] R. D. Cowan, J Appl. Phys. 34, 926(1963)
[3] L.M. Clark III and R. E. Taylor, J Appl. Phys. 46, 714(1975)
[4] J. A. Koski, "Improved Data Reduction Method for Laser Pulse Diffusivity Determination with the Use of Minicomputer", in Proc. Eigth Symp. Thermophysical Prop., Vol II, J.V. Sengers, Ed, Amer. Soc. Mech. Eng., New York (1981)
[5] J.A. Cape and G. W. Lehman, J Appl. Phys. 34, 1909(1963)
[6] E. Apinaniz, A Mendioroz, N. Madariaga, A Oleaga, R. Celorrio and A Salazar, J. Phys. D: Appl. Phys. **41**, 015403(2008)
[7] A Salazar, F. Garrido and R. Celorro, J Appl. Phys. **99**, 066116 (2006)
[8] A Salazar,R Fuente, E. Apinaniz and A Mendioroz, Rev. Sci. Instrum. **82**, 014902 (2011)

[9] C. P. Deck, H. E. Khalifa, B. Sammuli, T. Hilsabeck, and C. A. Back, Progress in Nuclear Energy, **57**, 38–45, (2012)

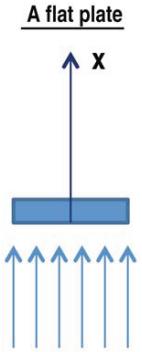

J. Zhang Fig. 1

Fig. 1 Cross-section of a flat plate.

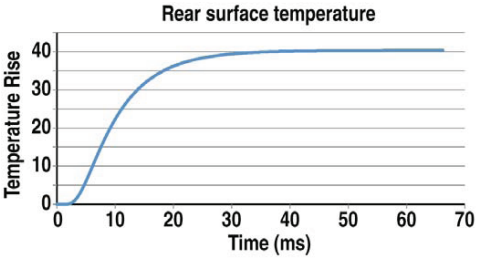

J. Zhang Fig. 2

Fig. 2 Calculated rear surface temperature rise of a lead flat plate, 1.25mm thick.

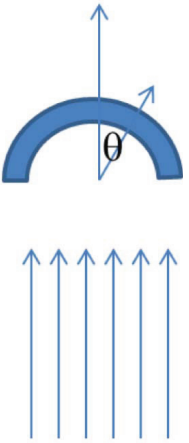

J. Zhang Fig. 3

Fig. 3 Cross section of cylindrical plate.

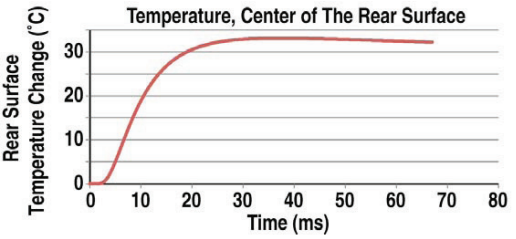

J. Zhang Fig. 4

Fig. 4 Calculated temperature change on the center of the rear surface for a curved lead plate with an outer radius of 5cm.

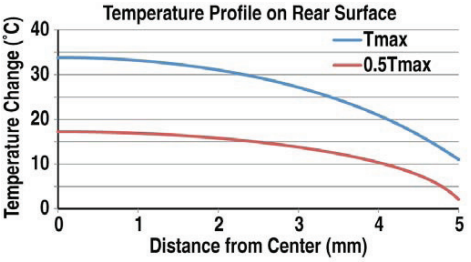

J. Zhang Fig. 5

Fig.5 Calculated temperature profile on rear surface for a curved lead plate when the center temperature reaches the maximum and half of the maximum.

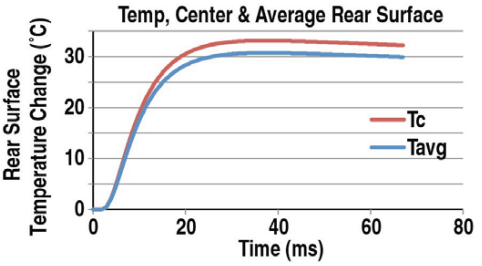

J. Zhang Fig. 6

Fig. 6 Calculated rear surface temperature change, taken at sample center and average of area viewed by detector aperture.

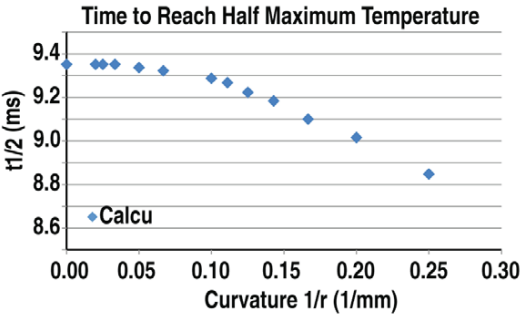

J. Zhang Fig. 7

Fig. 7 Calculated results for time to reach half of the maximum temperature on rear surface as a function of outer radius, r

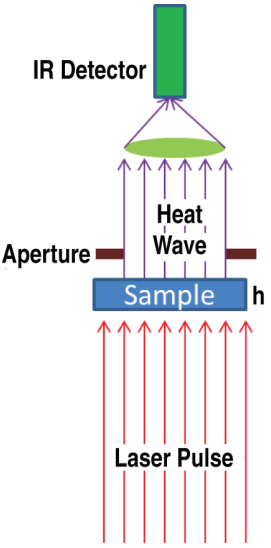

J. Zhang Fig. 8

Fig. 8 Scheme of the experimental setup

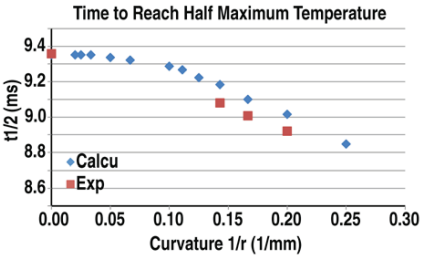

J. Zhang Fig. 9

Fig. 9 Experimental and calculated results for time to reach half of the maximum temperature on rear surface with the function of outer radius, r.

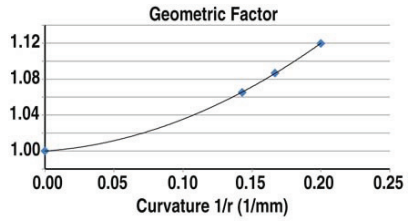

J. Zhang Fig. 10

Fig. 10 Experimental data for the geometrical factor for lead samples at room temperature and a fitted curve (Eq. 8).

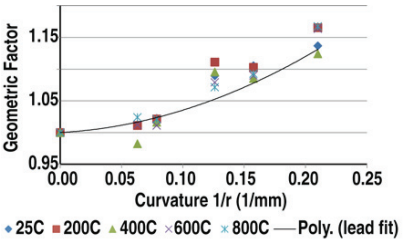

J. Zhang Fig. 11

Fig. 11 Experimental data for the geometrical factor of stainless steel, along with the fitted curve for lead samples (Eq. 8).

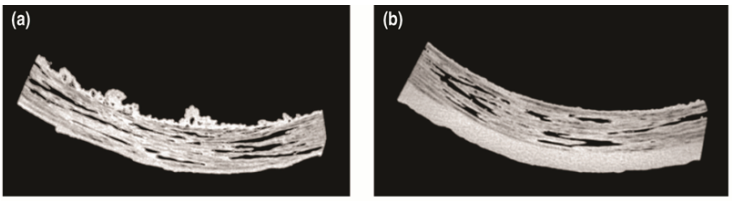

J. Zhang Fig. 12
Fig.12 (a) Representative void distribution for sample with higher void volume, (b) representative void distribution for overcoated sample with lower void volume.

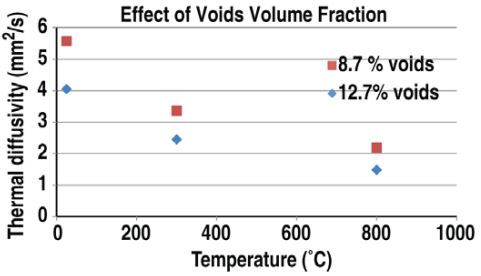

J. Zhang Fig. 13
Fig. 13 Effect of void volume fraction on thermal diffusivity.

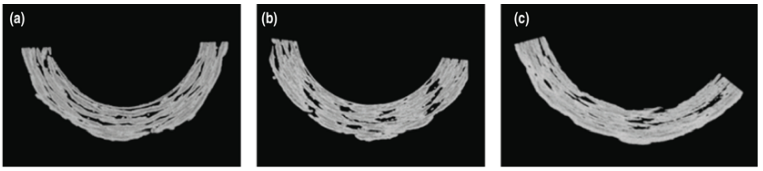

J. Zhang Fig. 14
Fig. 14 (a) Representative void distributions for a sample containing larger voids, (b) sample containing intermediate sized voids, and (c) sample containing smaller voids.

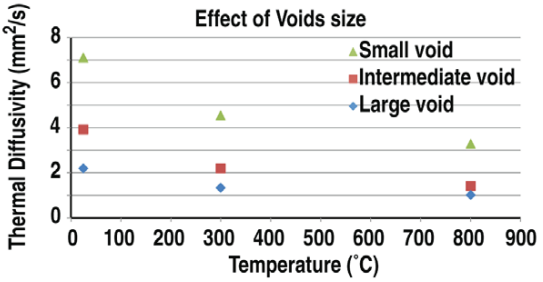

J. Zhang Fig. 15

Fig. 15 Effect of voids size on thermal diffusivity.

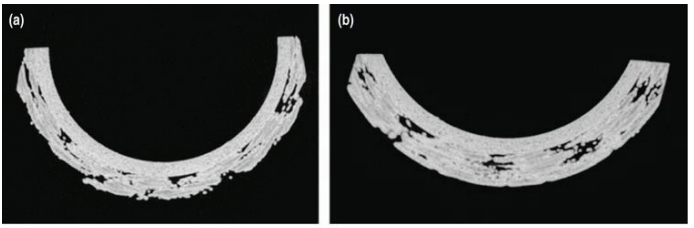

J. Zhang Fig. 16

Fig. 16 Representative cross-sections for combined monolith-composite tube structures having (a) lower monolith volume fraction, and (b) higher monolith volume fraction.

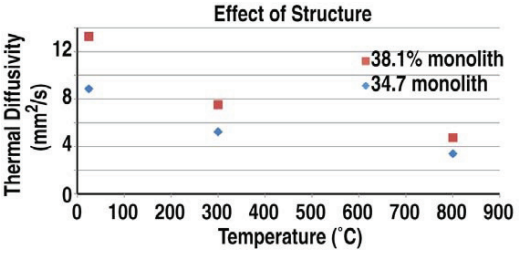

J. Zhang Fig. 17

Fig. 17 Effect of monolith volume fraction on thermal diffusivity.

Ceramics for Energy Generation, Conversion, and Rechargeable Energy Storage

GLASS CERAMIC SEPARATORS FOR ROOM TEMPERATURE OPERATING SODIUM BATTERIES

Wagner, D.; Rost, A.; Schilm, J.; Fritsch, M.; Kusnezoff, M.; Michaelis, A.

Fraunhofer Institute for Ceramic Technologies and Systems
Winterbergstr. 28
01277 Dresden
Germany

ABSTRACT

Promising compositions of solid electrolyte materials can be obtained with several compositions by various synthesis routes, like regular melt- quench process or producing NASICON-type glass ceramic, via sol-gel- or oxide synthesis, followed by calcination and ball milling to fine powders. These powders are transferred into slurries followed by tape casting of thin ceramic foils. Sintering is the most challenging step of the entire process. Cracking, bulging, warping and bloating have to be eliminated to get a plane and dense electrolyte substrate. NASICON-type glass ceramic compositions from the Na_2O-REO-SiO_2-system (REO– rare earth oxides) with and without additions of P_2O_5 have been prepared via glass melting, quenching on different materials, grinding to powder with subsequent sintering and crystallization after shaping steps like cold uniaxial pressing and tape casting. The separator materials were characterized by microscopy, XRD, density measurements and electrochemical impedance spectroscopy. Na^+ ion conducting ceramics with a relative densities of 95 to 97 %, a thickness about 300 µm and conductivities > $1 \cdot 10^{-3}$ S/cm at room temperature were obtained.

INTRODUCTION

While lithium batteries have gained great attention as portable energy sources for various applications (e.g. cell phones), their use as electrical storage for grid balancing is still under discussion because of the limited natural sources of lithium. Sodium is the low cost alternative for stationary battery systems, beyond that it is available in plentiful supply.

Promising stationary battery concepts are high temperature Na-S cell and Na-$NiCl_2$ cell the so called ZEBRA-Battery [ref.], with a sodium melt as an anode, a sulphur or nickel chloride as a cathode and a sodium ion conducting ceramic (β''-Na-Al_2O_3) as solid electrolyte placed in between of both electrodes. Major challenges for these battery types are high operating temperatures (200 to 300°C) which are needed to use liquid-state sulphur or nickel chloride-electrodes and the high volatility and reactivity of sodium. Sodium is very volatile, hygroscopic and oxidizing component, which makes it difficult to handle. This requires a considerable effort in protection of sodium against environment during operation of such battery systems. This leads to intensive research on new sodium sulfur battery systems with solid state electrolytes that are capable to operate at reduced temperatures below 100 °C. In order to maintain a high absolute ionic conductivity, the solid electrolyte needs to be very thin, dense and at the same time self-supporting, with a high sodium ion conductivity at room temperature and an excellent chemical stability e.g. in the battery electrolyte. Further a cycle stability at least of 300 cycles is necessary.

Although β''-Na-Al_2O_3 is used as electrolyte in standard high temperature sodium battery other materials such as $Na_3Zr_2Si_2PO_{12}$ can also be used as high Na^+ ionic conductors. Some of them are even commercialized as Na^+ conducting electrolyte and separator materials in the carbon dioxide gas sensors [3; 5-8]. Furthermore sodium batteries working at low temperatures (near to room temperature) are coming more and more into focus of R&D activities [9, 10, 11]. Also a number of rare earth doped ionic conductors have been investigated around the $Na_5RESi_4O_{12}$–system (RE= Sc, Y, Sm, Gd, Tb, Dy, Ho, Er, Tm,Yb, Lu) [1;4] as Na^+ conductors. Shannon et al. reported the highest Na+ conductivity (10^{-1}-10^{-2} S/cm at 200 °C) for this system [2]. While and β''-Na-Al_2O_3 and $Na_3Zr_2Si_2PO_{12}$ can only hardly be synthesized and sintered to substrates, the $Na_5RESi_4O_{12}$–compositions produced by glass melting route, would provide ability for sintering steps at reduced temperatures below 1200 °C.

For this reason sodium rare earth silicate glasses SiO_2-Na_2O-RE_2O_3 (RE= Y, Sm, Gd) have been investigated in this study for their possible application as sodium electrolyte at room temperature. The investigations focused on reaching an excellent ionic conductivity and good sinter ability as well on manufacturing of substrates by tape casting technology. This technology offers the potential to be up-scaled with a continuous tape casting facility and firing with multiple stacked setters in tunnel furnace typical for the ceramic mass production.

EXPERIMENTAL

All synthesized electrolyte materials were produced via the melt-quenching technique. The compositions of desired stoichiometry were melt in alumina or platinum crucibles. The raw oxides and carbonates were homogenised in a tumble mixer for 30 minutes and calcined for several hours at 500 °C. The melting temperatures varied between 1350 °C and 1450 °C.

The glasses were quenched on graphite, on brass or in water. The quenching procedure have a significant influence on subsequent properties. Preferably the glass stays amorphous during the cooling process. Undesirable are bubbles, streaks or extremely high tension that causes bursting of the glass. Further the frit is pre-milled by a vibratory disc mill and then treated in a planetary ball mill (dry) for at least 12 hours. To ensure that no contaminations occur, agate pots (SiO_2) and balls were used. Some powders were additionally milled in an attrition mill (in ethanol) to gain a fine particle size distribution.

For comparison purposes regarding conductivity, two reference materials were called in, commercial beta alumina purchased from Ionotec and self-made NASICON.

Samples for the ionic conductivity (via impedance spectroscopy) and density measurements were produced by pressing cylindrical compacts with 6mm diameter from the glass powder and sintering them on platinum foil. The plane and parallel interfaces were sputtered with gold (ion blocking electrodes) and pressed between two platinum current collectors. Impedance measurements at room temperature were carried out by a Gamry Reference 600 impedance analyser with a voltage amplitude of ± 100 mV in a frequency range between 100,000 and 0.02 Hz. Density measurements were performed by the archimedean principle in ethanol with a Sartorius CP2245 balance and a density determination kit.

The composition with mainly conductive phases have been processed to a slurry for tape casting. This technique is very flexible regarding the geometry of planar substrates. Long tapes with various thicknesses can be manufactured and any geometry can be cropped or lasered out of it. The slurry is made of the glass powder, which is pre-crystallized or still amorphous, a solvent, dispersant, binders and plasticizers. Mixing is done by roll-milling. If the slurry is homogeneous it will be degased and casted on silicon coated mylar foil, therefore a viscosity of 1-5 Pa·s is ideal.

After drying, which is a very sensitive step in the casting process, the single green tapes can be laminated to increase the green density and to stabilize the edges of cropped geometries. Furthermore several layers of green tapes can be laminated to a multilayer to get mechanically stable samples.

Investigations of the sintering behaviour were made by hot stage temperature microscopy, thermal dilatometry and differential thermal analysis. Comparing weight loss, beginning of visual deforming of the glass and the crystallisation peaks are important to understand the kinetics of the sintering process. Using these parameters the conditions of sintering (heating rates, holding steps, holding durations, cooling rates) have been optimized.

RESULTS AND DISCUSSION

To obtain dense and Na^+ conducting solid electrolytes by sintering of glass or glass ceramic powders, compositions with high ionic conductivity and a good sinter ability have to be found. In $Na_5RESi_4O_{12}$–system three types of crystalline phases denounced as N_3, N_5 and N_9 are known. Especially the N_5-type phase offers a high ionic conductivity and is therefore the most desired phase after crystallization. Hence the investigated compositions were chosen with respect to a good sintering behaviour targeting in the highly conducting N_5-type crystal phase in the sintered microstructures. The chosen compositions (see table 1) have different sodium and rare earth oxide content and show the influence on conductivity resulting from different stoichiometry.

Table 1 List of prepared compositions:

	A	B	C
Na^+: RE^{3+}	6.5 : 1	5 : 1	3.6 : 1
P_2O_5	Yes	No	No
Milling treatment	attrition mill & ball mill	attrition mill & ball mill	ball mill

The resulting sintering behaviors for all compositions after ball milling and attrition milling obtained from optical dilatometry is shown in fig.1. The composition C shows nearly no shrinkage, which indicates an overlap of the crystallization and the sintering process. Visually this can be already seen on quenched sample C (see in figure 1 (photo)). The glass looks milky compared to the amorphous and transparent material A, which is completely amorphous after quenching of the glass melt. Since there are already crystals present after quenching, the shrinkage ability is inhibited. Compositions A and B show beginning shrinkage at 600-625°C which can be associated with densification of the particles by a viscous flow of the glass melt. Furthermore the attrition milled powder of material A shows bloating (expansion) beyond 850 °C. It is important to achieve the sintering and crystallization below this temperature.

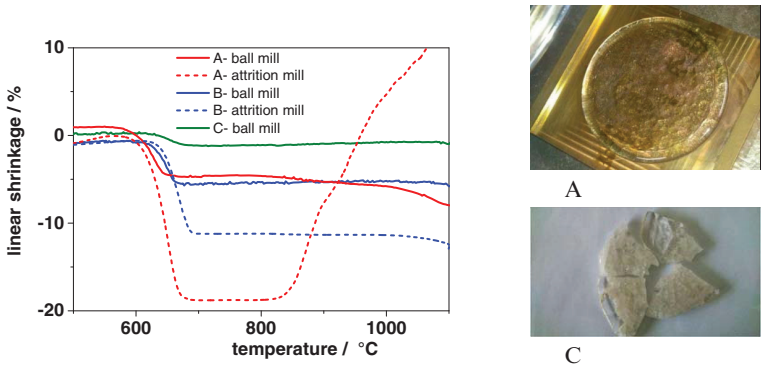

Figure 1 Shrinkage behavior obtained using hot stage microscopy and images of quenched glass samples

A correlation of the shrinkage behavior with the differential thermal analysis shows a clear difference between powders A and B (see figure 2). Material A first passes the sintering step first and crystallization starts subsequently, however for material B sintering and crystallization processes overlap strongly. This is actually a non-desired effect, because growing crystals are prone to inhibit further shrinkage. Also a design of the microstructure, by separated nucleation and crystal growth steps is only hardly possible.

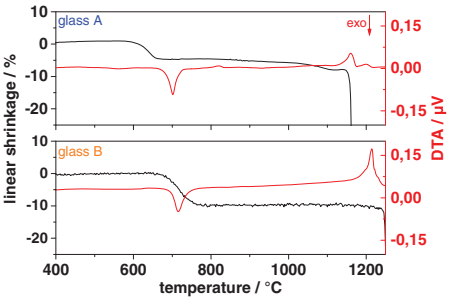

Figure 2 Thermal analysis and linear shrinkage of ball milled powders

A higher degree of densification can be reached, if powders of appropriate stoichiometry are treated by attrition ball milling. By high energy milling particle sizes of 1-2µm for d_{50} can be realized. The surface area is much bigger now and the smaller particles can be compressed even better, resulting obviously in a higher sintering activity. Due to the higher sintering activity of attrition milled powder (figure 1), the beginning of shrinkage is shifted to lower temperatures. The final peak temperature for sintering is reduced from 1100°C for the ball milled powder to only 800 °C for the attrition milled powder with even higher shrinkage in the end.

Fig. 3 shows the densities reached for cylindrical (uniaxial pressed) compacts of material A after holding the samples for 5 hours at the peak temperature. The density of ball milled material A increases further with peak temperatures above the maximum shrinkage/ densification temperature

of 650 °C (see figure 2), but it does not reach values beyond 2.6 g/cm³. In contrast, the achieved densities for attrition milled powder at temperatures above the maximum sintering temperature, are lower, because of the bloating effect (figure 1) at T > 850 °C. The highest density for this powder is reached at ~ 700 °C already with 95 % t. d. These results show that finer particles lead to strongly increased densities at considerable lower sintering temperatures.

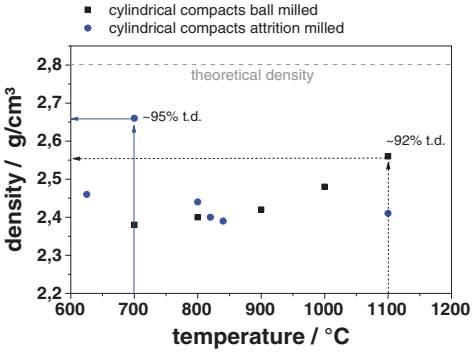

Figure 3 Density of ball and attrition milled powder of material A

Fig. 4 (left) shows typical impedance spectra measured on pressed and sintered samples at room temperature. At low frequencies (<100 Hz) the electrode impedance prevails. The phase shift between voltage and current in the frequency region between 400 Hz and 2 kHz is near to zero. A relaxation process related to the conductivity of the grain boundaries which are located in between neighbored Na+ conducting crystallites is seen at frequencies above 2 kHz. The frequency region 200 Hz – 2 kHz allows therefore a good opportunity for estimation of ionic conductivity. With room temperature measurements in such frequency ranges an interpretation of nyquist plots seems pointless. It is not possible to distinguish between grain interior and grainboundary conductivity here. The authors have also performed high temperature impedance spectroscopic measurements up to temperatures of 500°C. Only at temperatures above 200°C features in these spectra appear that allow to distinguish between both conductivity paths. The arrow in figure 4 (left) shows the point of interest, the impedance reaches a plateau while the phase shift is maximal, there the real part of impedance can be read off.

Not only has the densification had an influence on the ionic conductivity, but also the existing phases and therefore the sintering procedure. In the right diagram of figure 4 the dependence of the conductivity from the peak sintering temperature for material A is shown. The huge gap between sintering at 700 °C and 800 °C is remarkable, because obviously in this temperature range, the crystallization of the conductive phase starts, which increases the conductivity significantly. In accordance to the sintering behavior, shown in figure 1, the attrition milled powder reaches the maximum of conductivity at 850°C, which is even higher than conductivities for coarse powders at this point. In contrast the ball milled powder reaches comparable values not until 900 °C. Unfortunately beyond 850 °C bloating and pores occur for attrition milled powder A, which decreases the greatest possible total conductivity again.

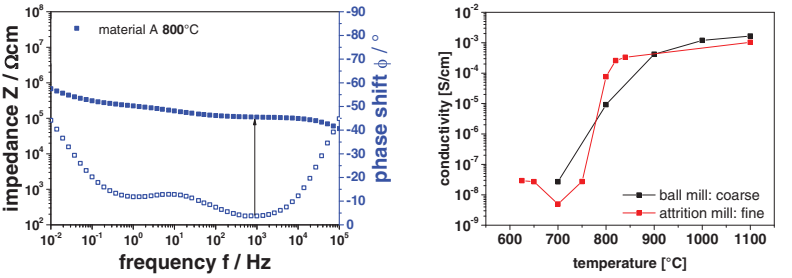

Figure 4 Impedance Vs. Phase Shift (Left) and Conductivity of Different Sintering Temperatures

Conductivity measurements for investigated crystallized glasses show quite different results (table 2), which are in agreement with phase content, detected in the samples. The samples with high content of N_5-type (A) show the highest ionic conductivity of about 10^{-3} S/cm at room temperature. To verify an ionic conductivity in these samples, potentiostatic DC measurements were carried out resulting in transport numbers of higher than 0,9. The crystalline phases appearing in the microstructure are dependent of the available Sodium and rare earth content (table 1). For this material system the high conductive phase is $Na_5RE(SiO_3)_4$ (N_5 type). Secondary phases are the N_3- and N_9- type which are significantly less conductive. Desirable is to get a dense specimen which N_5-type phase and only a low/no content of residual phases, as can be seen in figure 5 for ball milled material A.

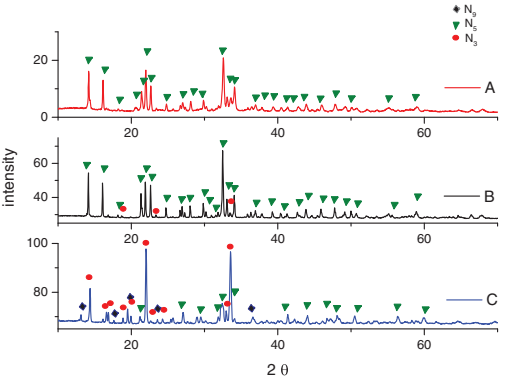

Figure 5 x-ray patterns for ball milled investigated materials >1100°C

Beyond 1100 °C, it is possible that the volatile sodium evaporates and the wanted stoichiometry cannot be realized anymore. X-ray diffraction investigations show N_5 phase mainly for the compositions A and B. Further they show small amounts of N_3-type for material B. Material C however shows only minor amount of the desired conductive phase N_5 and higher contents of N_3 and N_9 type phases. This fact correlates with the conductivity measurements.

Table 1: Room temperature conductivities and crystalline phases found in investigated materials compared to references

material	sintering temperature °C	conductivity S/cm	phase content
A-ball mill	1100	$1.4 \cdot 10^{-3}$	**N_5**
A-attrition mill	840	$3.3 \cdot 10^{-4}$	**N_5**, N_3
B- ball mill	1120	$1.2 \cdot 10^{-3}$	**N_5**, N_3
B-attrition mill	800	$2.4 \cdot 10^{-6}$	**N_3**, N_5
C- ball mill	1200	$3.6 \cdot 10^{-6}$	**N_3, N_9**, N_5
Beta alumina	1600	$8.9 \cdot 10^{-4}$	$NaAl_{11}O_{17}$
NASICON	1230	$2.3 \cdot 10^{-4}$	$Na_3Zr_2Si_2PO_{12}$, ZrO_2

Sample C, containing mainly the less conductive phases as N_3 and N_9 type (figure 5), the conductivity reaches only a maximum of 10^{-6} S/cm, at the maximal frequency (table 2). This indicates that N_3/N_9 are still conductive but not as good as N_5. The reason might be a structural effect of the unit cell of those crystals. The N_5 type is a loose packed cell, while the N_3 type e.g. is a very tight cell where not much ion movement is possible (see figure 6).

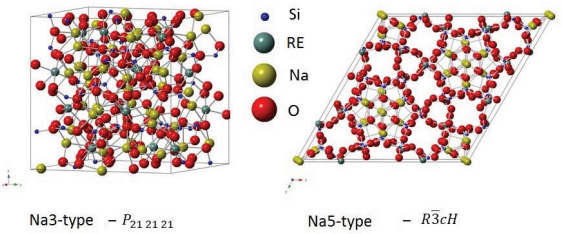

Figure 6 Structure of unit cells of conductive phases

The attrition milled material (A-attrition mill) shows an interesting behavior, the overall conductivity is not higher than for the coarse material A, but although the peak sintering temperature is 300 °C lower than for the ball milled material, it reaches comparable conductivities (Figure 4/ Table2). Still there is the disturbing N_3 phase at 840°C, for the attrition milled powder, assuming that either the peak temperature must be slightly increased or the sinter duration must be extended.

The attrition milled material of composition B shows a significantly lower conductivity. X-ray analysis shows, that because of the lower sintering temperatures for attrition milled powder compacts (B-attrition mill), the conductive phase is not fully crystallized after a short period of time. To get the best possible conductivity the sintering duration at peak temperature has to be extended here as well and a sintering additive might improve the properties.

The fact that a fine powder has a different conductivity behavior indicates, that not only the density and phase distribution but also the grain size and attending spandrels of residual phases have an influence on conductivity paths.

Supporting investigation of microstructure (density, micro cracks, grain sizes, impurities) and existing phases were done by FESEM analysis. Synthesized powders were sintered as powder compacts and cross sections were prepared. Shown here are 2 images of material A in ESB contrast (figure 7), where the dense microstructure, containing 3 different phases can be seen. As expected, it can be seen that finer initial particles lead also to a considerable finer microstructure. Thereby the different phases are distributed more homogenously for the fine grained material. Further in the coarser structure there seems to be some microcrackings , which cannot be found in the fine microstructure.

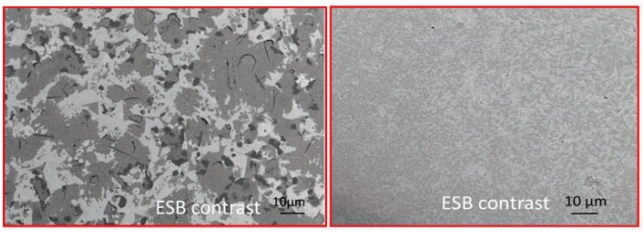

Figure 7 FESEM image of sintered powder compacts, left: ball milled powder ; right: attrition milled powder

For this work, no distinctive measurements for grain and grain boundary conductivity were done so far. Because of different microstructures and impedance measurements for sintered coarse and fine samples, we assume there must be a different conduction mechanism, for both of them. In general the conductivity within the crystalline grains is much higher than in the grain boundary phase. Schneider et. al measured similar total ionic conductivities for LISICON-type materials with strongly differing grain sizes in their micro structures [12]. They postulate that the conductivity of the grains and the grain boundaries distinguishes much more for coarser microstructures. In a microstructure with finer particles the conductivities of grains and grain boundaries are almost equal. Similar results are described by Jackman et al. [13]. Coarser grained materials have fewer grain boundaries, therefore, as grain size decreases, the grain boundary influence on conductivity increases, lowering the total conductivity. As the grains become coarser, the conductivity of the grains begins to dominate. This suggests to create coarse micro structures in order to maximize the effect of the grain conductivity. However an anisotropy for the thermal expansion coefficients according to the different crystallographic axis is known for several ion conducting NASICON-materials. This implies that coarse micro structures will produce micro cracks which impede the conductivity while finer micro structures behave more stable from a mechanical and an electrical point of view.

This matches also to our results where similar overall conductivities have been measured for a coarse and a fine grained micro structure. A high ionic conductivity is provided by the crystal structure of the N_5-type. More over in our case different crystallographic phases are present during sintering while the desired N_5-type phase tend to form at higher temperatures. The sintering additives segregate as poor or even non conducting grain boundaries. In case of our system contradicting effects depending on the sintering process and the initial particle size must be tuned in order to achieve good electrical and mechanical properties. Using a coarse powder a high sintering temperature is needed to achieve a high density and a high conductivity based on a monophasic N_5-type micro structure. This implies also a coarse micro structure and the occurrence of micro cracks. In contrast a fine powder results in highly dense, stable and fine grained micro structures at lower sintering temperatures. However the lower temperature inhibits the monophasic crystallization of the N_5-type phase. This can be only achieved by applying an

additional high temperature treatment which also leads to the undesired bloating effect and probably to grain coarsening.

In order to produce an ionic conductive solid electrolyte, the present powders were tailored in different ways for the tape casting process, either milled in different ways and/or pre-crystallized. Pre-crystallized powders have the advantage of less movement in the tape, while sintering, because the wanted phases are already there. Further sticking to setters might be inhibited. The ball-milled and attrition-milled powders of composition A/B have been sintered as casted tapes resulting in substrates of thickness 160 µm (figure 8). A density of 97 % t. d. was reached for the best sintered tapes (figure 9).

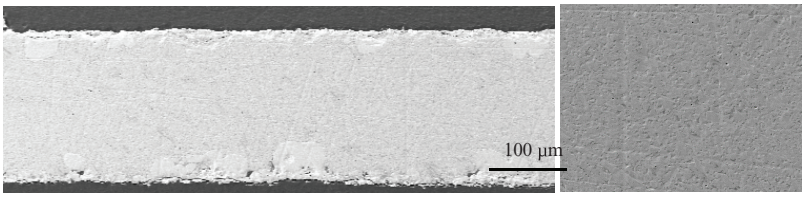

Figure 8 Cross section of a sintered tape of attrition milled powder

CONCLUSION

In this study the ionic conductivity and sintering ability of crystallized glasses in the system SiO_2-Na_2O-RE_2O_3 were examined. Due to partial crystallization while quenching the glass melts, some materials show poor densification, less conductive phases and thereby lower conductivities. The addition of appropriate sintering additives allowed the controlled separation of the sintering and the crystallization process resulting in highly dense micro structures. Maximum conductivities in this system can be obtained by crystallization of N_5-type phase. To realize such conductivities, not only a dense microstructure is needed, but also controlled crystallization at the optimal temperatures, that lead to a mono phasic N_5-type micro structure. It was shown that coarse grained micro structures lead to micro crackings which are assumed to be responsible for lowered ionic conductivities and also mechanical properties. In this work the highest conductivity of $1.4 \cdot 10^{-3}$ S/cm at room temperature was reached for a composition sintered at 1100 °C for 5 hours. Finer particles allowed considerable lower sintering temperatures while achieving only slightly lower conductivities and crack free micro structures. To obtain an actual solid state electrolyte which can be used in a battery cell (figure 9), the powders were used to prepare tape casting slurries for the doctor blade process. Self-supported sintering of sodium conducting glass ceramic tapes down to a thickness of 160 microns were realized by pressure less sintering in air.

Figure 9 translucent separators produced by tape casting; self-supporting sintering

REFERENCES

[1] Yamashita, K., Tanaka, M., Umegaki, T. : Thermodynamic and kinetic study on the phase transformation of the glass-ceramic Na+ superionic conductors, Solid State Ionics 1992, p. 231–236

[2] Shannon, Taylor, Gier , 1977: Ionic Conductivity in Na5YSi4012-Type Silicates, Inorganic Chemistry,1977

[3] Aung, Aung, Yan Lin; Itani, Kazunari; Asahi, Taro; Kiyono, Hajime; Sakamoto, Masatomi: Electrical properties of $(Na_2O)_{35.7}(RE_2O_3)_{7.2}(GeO_2)_{57.1}$ (RE=Sm, Gd, Dy, Y, Ho, Er and Yb) glasses, Materials Chemistry and Physics, 2008

[4] Okura, Toshinori: New superionic conducting glassceramics in the system Na_2O-Y_2O_3-Sm_2O_3-P_2O_5-SiO_2 : Crystallization and Ionic conductivity, Journal of ceramic society of Japan, 2003

[5] Fuentes : Optimised NASICON Ceramics for Na sensing, Solid State Ionics, 2002

[6] Miyajima: Ionic conductivity of NASICON-type $Na_{1+x}M_xZr_{2-x}P_3O_{12}$ (M: Yb, Er, Dy), Solid State Ionics, 1996

[7] Wachsman: High conductivity Nasicon Electrolyte for room temperature solid state sodium ion batteries, patent WO2014/052439, 2014

[8] Hayashi, Akitoshi; Noi, Kousuke; Sakuda, Atsushi; Tatsumisago, Masahiro: Superionic glass-ceramic electrolytes for room-temperature rechargeable sodium batteries, nature communications, 2012

[9] C.-W. Park, J.-H. Ahn, Ho-Suk Ryu, Ki-Won Kim, and H.-J. Ahn, Room-Temperature Solid-State Sodium/Sulfur Battery, Electrochem. Solid State Lett. 9 (2006) A123-A125

[10] H. Ryua, T. Kimb, K. Kima, J.-H. Ahn, T. Nama, G. Wanga, H.-J. Ahn, Discharge reaction mecha-nism of room-temperature sodium–sulfur battery with tetra ethylene glycol dimethyl ether liquid electrolyte, J. Power Sources 196 (2011) 5186–5190

[11] W.G. Coors, C. Boxley, M. Robins, A. Eccleston, Low temperature molten sodium secondary cell with sodium ion conductive electrolyte membrane, WO2012061823A2 (2012)

[12] Schneider,Meike ; SCHOTT, Glass-ceramic electrolytes for solid state batteries, presentation at Bunsen Kolloqium, Frankfurt 11/2014

[13] Jackman, Spencer: Effect of microcracking on ionic conductivity in LATP; Journal of Power Sources , 2012

AVENUE TOWARDS THE DEVELOPMENT OF NEW NANOSTRUCTURED COMPOSITE CATHODE MATERIALS FOR LITHIUM-ION BATTERIES

Nina Kosova
Institute of Solid State Chemistry and Mechanochemistry SB RAS
Novosibirsk, Russia

ABSTRACT

The present work represents a review on nanostructured composite electrode materials prepared by mechanochemically assisted solid-state synthesis using a high-energy mechanical activation (MA). As-developed approaches include: 1) joint MA of two active cathode materials; 2) direct mechanochemically assisted solid-state synthesis from a multicomponent reagent mixture without mutual dissolution of the components; 3) formation of a second phase via partial decomposition of pristine material prepared using MA; 4) solid-state solvent-free formation of "core-shell" cathode materials with a high-conductive "shell". Structure, morphology and electrochemical properties of the as-prepared materials were investigated by a complex of physicochemical methods including XRD with Rietveld refinement, solid-state MAS NMR, Mössbauer and XPS spectroscopy, SEM and TEM microscopy, *in situ* synchrotron diffraction, galvanostatic cycling, etc. It has been shown that due to unique combination of properties, the as-prepared nanostructured composites have advantages over the individual components, including better cycleability and high-rate capability, lower price, more suitable charge-discharge profiles and operating voltage, etc.

INTRODUCTION

One of the promising approaches to the optimization of the properties of lithium-ion batteries (LIBs) is in the development of new composite electrode materials consisting of two (or more) active components in order to use the advantages of the both of them [1]. Due to a unique combination of properties, the mixed materials show some advantages over the individual components. This includes the longer lifetime, the decreased capacity fading upon the cycling, lower price, the improved thermal stability, more acceptable profiles of charge-discharge curves and operating voltage, etc.

In the present work, novel composite electrode materials for LIBs were prepared using the high-energy mechanical activation method (MA) to achieve the enhanced electrochemical properties over the individual components. MA with high-energy mechanoactivators is a modern energy- and eco-efficient method of fine grinding, mixing, and activation of solid reagents and is widely used to prepare different functional materials [2, 3]. As an example, we report the results of studying the synthesis, structure, morphology, and electrochemical properties of the composite cathode materials prepared by different procedures: 1) joint MA of two individual cathode materials (the $LiCoO_2/LiMn_2O_4$ composites); 2) direct mechanochemically assisted solid state synthesis starting from a multicomponent mixture of reagents without mutual dissolution of the components ($LiFePO_4/Li_3V_2(PO_4)_3$ composites); 3) synthesis via heat-induced partial decomposition of a single-phase nanosized cathode material, prepared by MA, with the elimination of a gaseous by-product and the formation of the second electrochemically active component (the $LiVPO_4F/Li_3V_2(PO_4)_3$ composites); 4) solid-state solvent-free mechanochemical synthesis of 'core-shell' materials ($LiCoO_2$ surface modified by inert oxides; $LiMO_2$ (M = Co, Ni)-coated $LiMn_2O_4$).

EXPERIMENTAL

A short-time (5-10 min) mechanical activation was performed using a high-energy AGO-2 planetary mill (900 rpm) with stainless jars and balls. The as-prepared materials were analyzed by X-ray powder diffraction method (XRD) using a Bruker D8 Advance diffractometer, Cu $K\alpha$ irradiation (λ=1.54181 Å). XRD patterns were collected with a step of 0.02°/s and an uptake time of 0.3 – 0.5 s. Structural refinement of the XRD data was carried out by the Rietveld method using the GSAS software package. Mössbauer spectra were recorded by means of a NZ-640 spectroscope, Hungary, with a Co^{57} γ-ray source at room temperature. MAS NMR spectra were recorded using a Bruker AV-300 solid-state NMR spectrometer with rotor-synchronized Hahn-echo pulse sequences. The chemical composition of the surface of the samples was studied with a VG ESCALAB HP X-ray photoelectron (XPS) spectrometer (Al$K\alpha$ radiation, $h\nu$ = 1486.6 eV). The particle size and morphology were investigated by scanning (SEM) and high-resolution transmission (HRTEM) electron microscopy using a LEO 1430 VP and a JEM-40000EX microscopes.

For the electrochemical testing, the composite cathodes were fabricated by mixing 80 wt% active material with 15 wt% Super P conductive carbon (Timcal Ltd.) and 5 wt% PVDF/NMP binder. The mixed slurry was then pasted on the aluminum foil to obtain working electrodes. The loading density of the prepared samples was 2-3 mg cm^{-2}, and an electrode diameter of 10 mm was used throughout. The working electrodes were dried at 120 °C before cell assembly. Swagelok-type cells were assembled in an argon-filled glovebox with Li as the anode; 1M $LiPF_6$ (Sigma Aldrich, 99.99 %) solution in a mixture (1:1 by weight) of ethylene carbonate (EC) and dimethylcarbonate (DMC) (Alfa Aesar, 99 %) as an electrolyte; and a glass fiber filter (Whatman, Grade GF/C) as a separator. Cycling was performed using a galvanostatic mode at room temperature.

Phase transitions upon cycling were studied by *in situ* synchrotron diffraction at the High-Resolution Powder Diffraction (HRPD) beamline P02.1 of the PETRA III electron storage ring at DESY (Hamburg, Germany) (λ = 0.20727 Å). Diffraction patterns were recorded each 2 min by a PerkinElmer XRD 1621 detector under galvanostatic cycling of the samples at C/10 rate at room temperature.

RESULTS AND DISCUSSION

$LiCoO_2$/$LiMn_2O_4$ composites

Layered lithium cobalt oxide $LiCoO_2$ (space group R-3m) [4] and lithium manganese spinel $LiMn_2O_4$ (space group Fd-3m) [5] are well known cathode materials for LIBs. As compared to layered cathodes, $LiMn_2O_4$ is less expensive and less toxic and is characterized by higher operating voltage, better high-rate capability and thermal stability. Therefore, it is very attractive to be used as the second component in a mixture with $LiCoO_2$. At the same time, $LiMn_2O_4$ has a lower Coulomb capacity and some disadvantages associated with the structural rearrangement upon the cycling [6] and the Mn dissolution in the electrolyte [7], which can cause high capacity fading.

Earlier, it has been shown that some disadvantages of cathode materials can be overcome by the preparation of physical blends of these components in blenders [8-10]. In the present study, the (1-x)$LiCoO_2$/$x$$LiMn_2O_4$ ($0.4 \le x \le 0.7$) mixtures of the preliminary synthesized components were jointly activated in a AGO-2 planetary mill. According to Figs. 1 and 2, the XRD patterns of the as-prepared products are a superposition of the reflections of the initial phases, $LiCoO_2$ and $LiMn_2O_4$. The samples are characterized by an average particle size of about 100-200 nm (Fig. 3), i.e. much lower than the initial components.

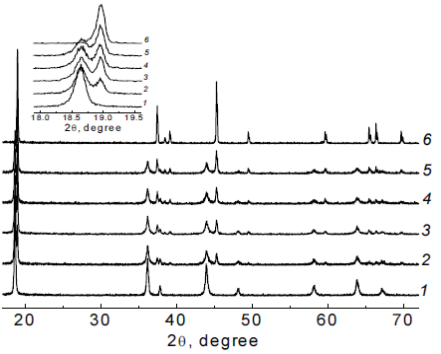

Figure 1. XRD patterns of the initial $LiMn_2O_4$ (1) and $LiCoO_2$ (6), and mechanocomposites (1-*x*)$LiCoO_2$/*x*$LiMn_2O_4$: *x*=0.7 (2); 0.6 (3); 0.5 (4); 0.4 (5).

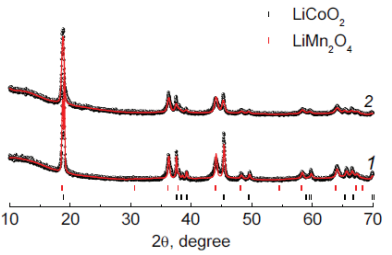

Figure 2. Rietveld refined XRD patterns of the as-prepared mechanocomposite $0.5LiCoO_2/0.5LiMn_2O_4$ (1) and the product formed after the 12th cycle (2).

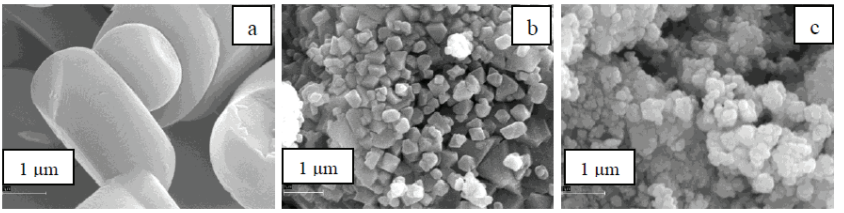

Figure 3. SEM images of the initial $LiCoO_2$ (a), $LiMn_2O_4$ (b) and mechanocomposite $0.5LiCoO_2/0.5LiMn_2O_4$ (c).

The mechanocomposites show the smoothing charge-discharge profiles and a good cycleability with a reversible capacity of ~110 mA h g^{-1} (Fig. 4) [11, 12]. Lithium intercalation-deintercalation is accompanied by the Co^{3+}/Co^{4+} and Mn^{3+}/Mn^{4+} redox processes and the $LiCoO_2 \leftrightarrow CoO_2$ and $LiMn_2O_4 \leftrightarrow MnO_2$ phase transitions. First, the Co^{3+}/Co^{4+} pair is activated and then lithium deintercalation occurs with the participation of the both couples. d*Q*/d*V* vs. voltage plots for the first cycle of the composites show three redox peaks corresponding to the initial components: $LiCoO_2$ and $LiMn_2O_4$ (Fig. 5). The redox peaks of $LiCoO_2$ gradually vanish upon the following cycling of the composites. According to XRD data, the $LiCoO_2$ phase is still preserved in the product after the 12th cycle, although the intensity of its reflections noticeably decreases and the *c* parameter increases (Fig. 2). The decrease in the intensity of the Co^{3+}/Co^{4+} peaks on the d*Q*/d*V* vs. voltage plots is associated most likely with a gradual transition of the layered to spinel structure in the composite, contrary to the corresponding physical mixture.

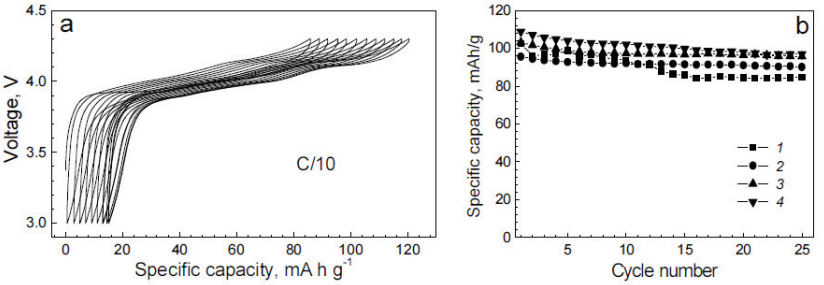

Figure 4. Typical charge-discharge profiles (a) and discharge capacity vs. cycle number plot (b) for mechanocomposites (1-*x*)$LiCoO_2$/*x*$LiMn_2O_4$: *x* = 0.7 (1); 0.6 (2); 0.5 (3); 0.4 (4).

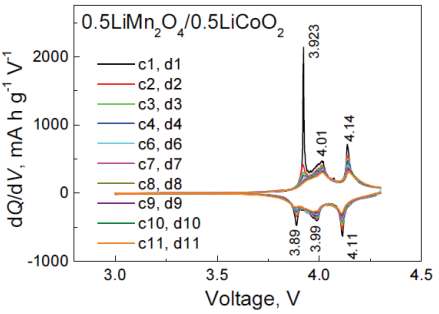

Figure 5. d*Q*/d*V* vs. voltage plots for the first eleven cycles of the 0.5$LiCoO_2$/0.5$LiMn_2O_4$ mechanocomposite.

$LiFePO_4$/$Li_3V_2(PO_4)_3$ composites

Orthorhombic lithium iron phosphate $LiFePO_4$ (space group *Pnmb*) is a favorite among the framework-structured cathode materials due to its high operating voltage and electrochemical capacity, as well as high structural, chemical and thermal stability [13]. However, it is characterized by the low electronic conductivity and lithium-ion diffusion. Another Li-V-based cathode - lithium vanadium phosphate $Li_3V_2(PO_4)_3$ with a monoclinic structure (space group $P2_1/n$) - is a Nasicon-type compound with a high lithium-ion conductivity [14].

In the present work, we prepared the 0.5$LiFePO_4$/0.5$Li_3V_2(PO_4)_3$ composites using MA in AGO-2 planetary mill by the joint carbothermal reduction of Fe_2O_3 and V_2O_5 in a mixture with Li_2CO_3 and $(NH_4)_2HPO_4$. Carbon, used as a reducing agent, hindered the sintering of the product particles, while its excess was used to form an electronically conductive carbon coating. The activated mixture was annealed at 750 °C in an Ar flow. The amount of carbon in the final material was ~ 5%. The XRD pattern of the final product showed two sets of reflections belonging to the $LiFePO_4$ and $Li_3V_2(PO_4)_3$ phases, which is an evidence that the solid solutions

do not form in the whole (but only limited) concentration range in the $LiFePO_4$-$Li_3V_2(PO_4)_3$ system (Fig. 6). No impurity phases were detected. According to the Rietveld refinement, the $LiFePO_4$ component in the composite is characterized by the presence of ~4% of Li vacancies and about ~4% of V^{3+} ions substituted for Fe^{2+}. The Mössbauer spectrum of the $0.5LiFePO_4/0.5Li_3V_2(PO_4)_3$ composite is well fitted by a symmetric doublet originated from the octahedral Fe^{2+} ions in the olivine structure (Fig. 7). A small additional doublet corresponding to ~4% of Fe ions with different electronic configuration has been also detected. SEM results evidence that the composite consists of near-spherical nanosized particles (an average particle size of about 100-200 nm) with a narrow size distribution, while larger rod-shaped particles are observed for pure $Li_3V_2(PO_4)_3$ due to low crystallization temperature, thus pointing that $LiFePO_4$ and $Li_3V_2(PO_4)_3$ hinder the crystal growth of each other particles upon heating.

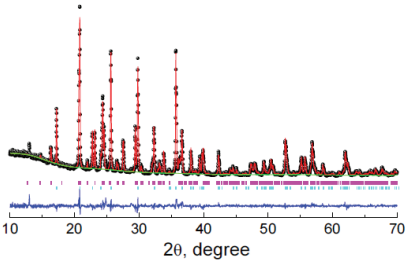

Figure 6. Multiphase Rietveld refined XRD pattern of the $0.5LiFePO_4/0.5Li_3V_2(PO_4)_3$ mechanocomposite.

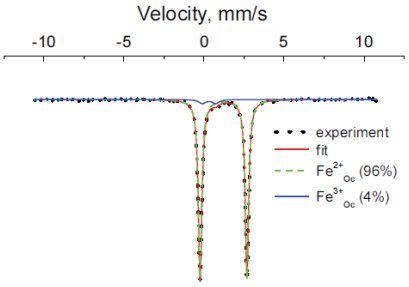

Figure 7. ^{57}Fe Mössbauer spectrum of the $0.5\ LiFePO_4/0.5Li_3V_2(PO_4)_3$ mechanocomposite.

Electrochemical behavior of the composite was studied within the 2.5-4.3 V voltage range at *C*/10-20*C* charge-discharge rates. As it is seen from Fig. 8a, the cycling curves have four plateaus corresponding to the following redox pairs: Fe^{2+}/Fe^{3+} (below 3.4 V) and $V^{3+}/V^{4+,5+}$ (above 3.4 V). According to d*Q*/d*V* vs. voltage plots, a fine mixing of two components at the nanolevel does not change the potentials of the Fe^{2+}/Fe^{3+} and $V^{3+}/V^{4+,5+}$ redox couples [15] as it was observed in the mixed olivine-structured solid solutions [16, 17]. The composite shows an excellent charge-discharge reversibility as compared with the individual components starting from 130 mA h g^{-1} at *C*/10 rate to 70 mA h g^{-1} at 20*C* (Fig. 8b).

The mechanism of phase transitions upon charge and discharge of the composite was studied by *in situ* synchrotron diffraction using a polyamide cell described elsewhere [18]. Figure 9 shows a set of diffraction patterns of the $0.5LiFePO_4/0.5Li_3V_2(PO_4)_3$ composite upon its charge to 4.8 V. It is seen that the process is accompanied by the successive phase transitions: $LiFePO_4 \rightarrow FePO_4$; $Li_3V_2(PO_4)_3 \rightarrow Li_{2.5}V_2(PO_4)_3 \rightarrow Li_2V_2(PO_4)_3 \rightarrow LiV_2(PO_4)_3 \rightarrow V_2(PO_4)_3$, characteristic of the individual components. The enhancement of the electrochemical performance of the composite should be attributed mainly to the fine mixing of $LiFePO_4$ with $Li_3V_2(PO_4)_3$ rather than to the doping of V in the host lattice of $LiFePO_4$, and due to higher lithium diffusion arose from the presence of $Li_3V_2(PO_4)_3$ with the open Nasicon-type structure. The increase of a number of voltage plateaus and the mean intercalation voltage should be advantageous for improvement of the cell performance of $LiFePO_4$.

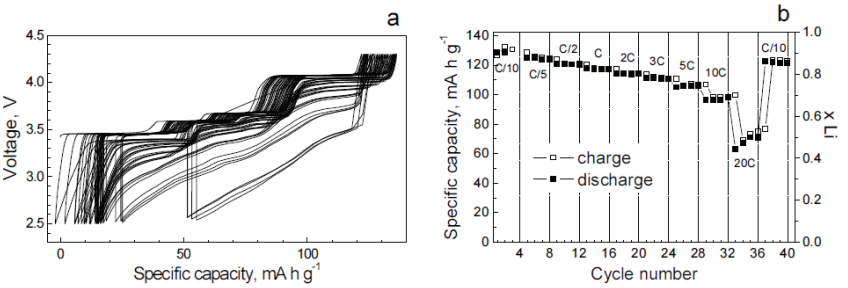

Figure 8. Charge-discharge profiles (a) and specific capacity vs. cycle rate plot (b) for the $0.5LiFePO_4/0.5Li_3V_2(PO_4)_3$ mechanocomposite.

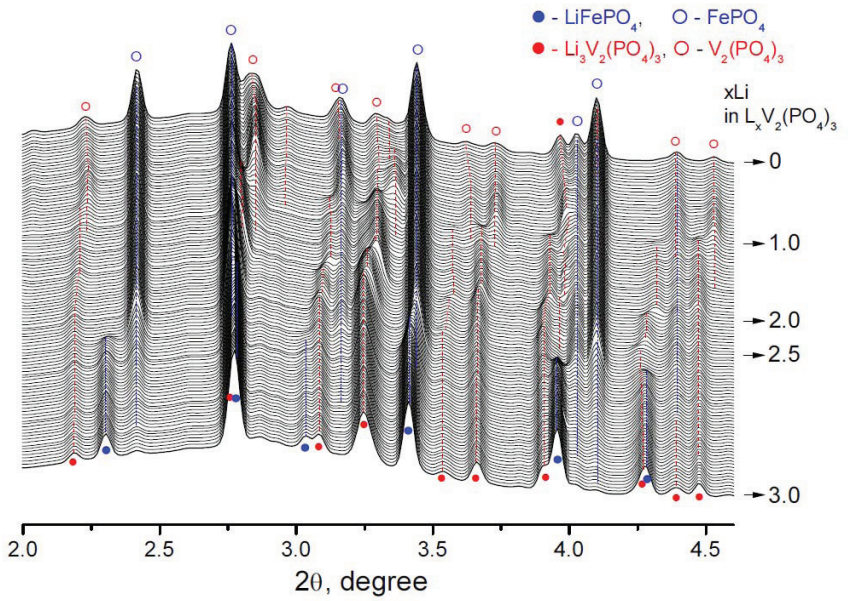

Figure 9. A set of XRD patterns obtained during the charge of the $0.5LiFePO_4/0.5Li_3V_2(PO_4)_3$ composite by in situ synchrotron diffraction (λ=0.20727 Å).

$LiVPO_4F/Li_3V_2(PO_4)_3$ composites

Lithium vanadium fluorophosphate $LiVPO_4F$ with a triclinic structure (space group $P\bar{1}$) is a promising high-voltage cathode material [19]. However, the synthesis of $LiVPO_4F$ is poorly reproducible. In the present work, $LiVPO_4F$ was synthesized by annealing the activated mixture of VPO_4 with LiF [20].

Figure 10 shows *in situ* XRD patterns collected under heating and cooling the activated mixture of VPO_4 with LiF in a temperature-controlled chamber of a Bruker diffractometer. It has been found that $LiVPO_4F$ is formed and crystallizers upon heating up to 500 °C. At temperatures above 600 °C and under slow cooling, $LiVPO_4F$ decomposes to $Li_3V_2(PO_4)_3$ and V_2O_3. In the further experiments, $LiVPO_4F$ was prepared by heating the activated mixture followed by a quick (Sample A) or slow (Sample B) cooling to room temperature.

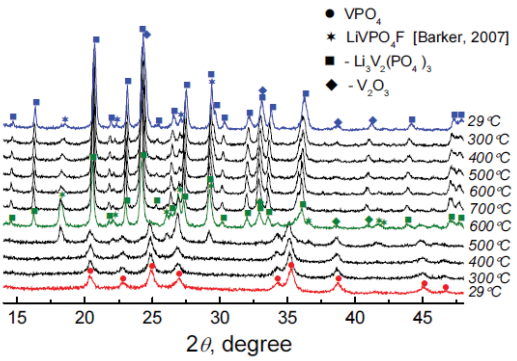

Figure 10. *In situ* XRD patterns of the products formed in the VPO_4+ LiF activated mixture under heating and cooling in a temperature-controlled chamber of a Bruker diffractometer.

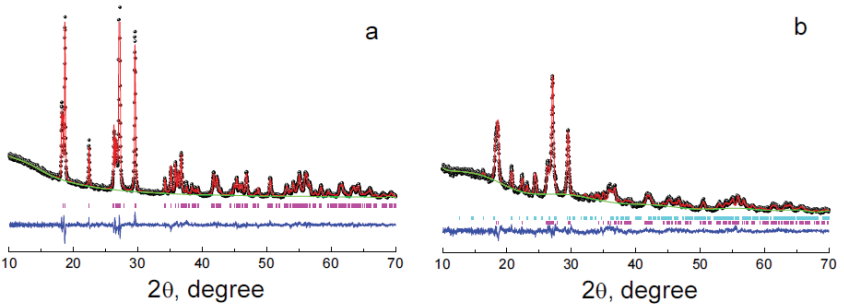

Figure 11. Rietveld refined XRD patterns of phase-pure $LiVPO_4F$ (a) and the $LiVPO_4F/Li_3V_2(PO_4)_3$ composite (b).

Rietveld refined XRD patterns of thus-prepared $LiVPO_4F$ samples are shown in Fig. 11. The diffraction data of Sample A were successfully refined using the $LiFePO_4F$ triclinic structure with the space group $P\bar{1}$ as a refinement model [21]. The $LiVPO_4F$ structure comprises a three-dimensional framework built up from PO_4 tetrahedra and VO_4F_2 octahedra with the oxygen atoms shared between PO_4 and VO_4F_2. The refined lattice parameters of Sample A are as follows: a=5.299(2) Å, b=7.240(2) Å, c=5.163(1) Å, α=107.890(3)°, β=98.482(3)°, γ=107.529(3)° and lattice volume, V=173.3(1) Å^3 (R_{wp}=5.91 %, R_p=4.59 %, χ^2=1.712). XRD

pattern of Sample B is less intensive and indicates that this sample consists of two well crystallized phases: of the triclinic $LiVPO_4F$ with a space group $P\bar{1}$ and the monoclinic $Li_3V_2(PO_4)_3$ with a space group $P2_1/n$. The calculated lattice parameters of the main $LiVPO_4F$ phase are slightly different from those of Sample A: a=5.296(1) Å, b=7.250(1) Å, c=5.193(1) Å, α=107.72(2)°, β=98.63(1)°, γ=107.49(1)° and cell volume, V=174.63(7) Å^3 (R_{wp}=5.67 %, R_p=4.36 %, χ^2=1.822). The parameters of the impurity $Li_3V_2(PO_4)_3$ phase are close to those reported in literature: a=8.603(3) Å, b=8.589(3) Å, c=12.037(4) Å, β=90.27(6)°, and cell volume, V=889.4(5) Å^3. The mass content of $LiVPO_4F$ and $Li_3V_2(PO_4)_3$ determined by multiphase Rietveld refinement is 85 wt.% and 15 wt.%, respectively. The appearance of $Li_3V_2(PO_4)_3$ in Sample B is due to volatilization of VF_3 at longer calcination of the reactive mixture according to the following reaction, first proposed by Barker [22]:

$$3LiVPO_4F \rightarrow VF_3 + Li_3V_2(PO_4)_3 \quad (1)$$

In the HRTEM image of Sample B, a grain boundary of crystalline $Li_3V_2(PO_4)_3$ and $LiVPO_4F$ has been clearly observed [20]. The determined interfacial distances from FFT were as follows: d_{220}=0.3 nm and d_{121}=0.36 nm for $Li_3V_2(PO_4)_3$; d_{010}=0.48 nm and $d_{10\text{-}2}$=0.33 nm for $LiVPO_4F$. Thus, $LiVPO_4F$ and $Li_3V_2(PO_4)_3$ microcrystals well inset into each other resulting in the nanodomain composite formation, rather than a simple microscopical mixing.

Figure 12 shows the cycling voltage profiles and the corresponding differential capacity plots in the 3.0-4.5 V range for two $LiVPO_4F$ samples prepared by quick and slow cooling. Sample A shows a too-step charge profile, while the insertion curve has only one plateau. Correspondingly, two sharp and well defined oxidation peaks are observed on the dQ/dV vs. voltage plots at 4.25 V and 4.30 V, indicating two distinct but energetically similar reactions.

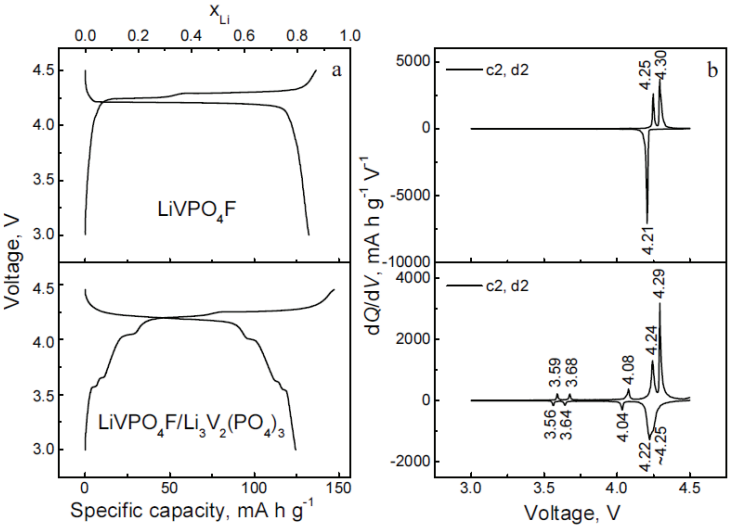

Figure 12. Charge-discharge profiles of phase-pure $LiVPO_4F$ and the $LiVPO_4F/Li_3V_2(PO_4)_3$ composite (a) and the dQ/dV vs. voltage plots (b) in the 3.0-4.5 V range at C/10 rate.

The charge voltage plateaus may be subdivided into two compositional regions with a bend at the voltage of ~4.275 V with x_{Li}~0.338. The Li insertion in Sample A is characterized by a single, sharp and well-defined differential capacity peak, located at 4.21 V vs. Li/Li^+. On the contrary, a slightly sloping profile is observed instead of plateau for Sample B. The reduction peak at ~4.23 V on the dQ/dV vs. voltage plot becomes broader and less intensive than that for Sample A. Moreover, the additional redox peaks are also observed at lower voltages (3.59, 3.68 and 4.08 V), which are well attributed to the $Li_3V_2(PO_4)_3$ phase, corresponding to the XRD results. The authors [23], based on *in situ* X-ray and neutron diffraction data, proposed the formation of the $Li_{0.67}VPO_4F$ intermediate composition between $LiVPO_4F$ and VPO_4F, responsible for the existence of two separate voltage plateaus on charge. Upon discharge, a single two-phase reaction takes place between VPO_4F and $LiVPO_4F$ without the occurrence of the intermediate $Li_{0.67}VPO_4F$ phase.

The samples A and B showed a high discharge capacity of 132 and 125 $mAhg^{-1}$, respectively, in the 3.0-4.5 V range, and a low degree of cell polarization as evidenced by the level of voltage hysteresis and an excellent long-term stability with the exceptionally low-capacity fade characteristics [20]. Low polarization is likely due to a facile ionic transport in the tavorite-type lattice. According to Fig. 13, both samples are capable for a high-rate performance. There is a relatively insignificant discharge capacity 'penalty' when the rate was increased from *C*/10 to *C*, indicating that the high-rate capability of $LiVPO_4F$ is superior to the other polyanion active materials such as $LiMPO_4$ (M=Fe, Mn). An increase in the IR drop becomes noticeable at higher *C* rates and is more pronounced for Sample A. The better high-rate performance of Sample B ($LiVPO_4F/Li_3V_{2(}(PO_4)_3$ composite) can be attributed to the presence of a fast ionic conductor, $Li_3V_{2(}(PO_4)_3$, which improves the ionic transport of the as-prepared composite cathode material. The estimated amount of $Li_3V_{2(}(PO_4)_3$ in Sample B from charge-discharge capacity plots (Fig. 12) is about 10 %, which well corresponds to the XRD multiphase refinement.

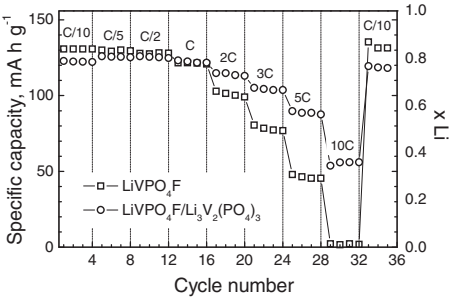

Figure 13. Charge-discharge capacity vs. cycling rate (C/10 – 10 C) plot for phase-pure $LiVPO_4F$ and the $LiVPO_4F/Li_3V_2(PO_4)_3$ composite in the 3.0-4.5 V range.

Thus, the phase composition of the $LiVPO_4F$-based materials, prepared by mechanochemically assisted solid-state synthesis from VPO_4 and LiF, strongly depends on the sintering temperature and heating/cooling rates. In the case of quick cooling, a single-phase material is obtained, while in the case of slow cooling, $LiVPO_4F/Li_3V_{2(}(PO_4)_3$ composites are formed. Such composites are characterized by insertion of the nanocrystals of $LiVPO_4F$ and $Li_3V_{2(}(PO_4)_3$ into each other resulting in a nanodomain structure formation. Contrary to plateaus

observed on charge-discharge curves of $LiVPO_4F$, the $LiVPO_4F/Li_3V_{2(}(PO_4)_3$ composites show the sloping profiles and better high-rate performance attributed to a synergistic effect and high ionic conductivity of $Li_3V_{2(}(PO_4)_3$.

Surface modified $LiCoO_2$

Recent researches demonstrate the importance of surface structural features on the electrochemical performance of electrode materials for lithium-ion batteries. It was found that the surface coating of the cathode materials ($LiCoO_2$, $LiNiO_2$, $LiMn_2O_4$) can prevent their direct contact with the electrolyte solution, suppress side reactions, improve chemical and structural stability, even at extended cell voltage [24]. Simultaneously, other effects are observed such as suppression of the dissolution of Mn^{2+}, higher conductivity, removal of HF from electrolyte solution, etc. After effective coating, the noticeable improvements in the electrochemical performance of the electrode materials including the increased reversible capacity, the enhanced cycling behavior and high rate capability can be achieved. However, the mechanisms of protection are still remaining open.

Surface modification is usually realized by wet chemical methods (such as precipitation solution method; sol-gel; micro-emulsion; Pechini method) or physical methods (pulsed laser deposition, plasma enhanced chemical vapor deposition, gas suspension spray, radio frequency magnetron sputtering). In the present study, we used the solid state solvent-free mechanical activation (MA) method for the surface modification of $LiCoO_2$ by the simple oxides (Al_2O_3, TiO_2, MgO and $Li_2O{\cdot}2B_2O_3$) [25-27]. The commercial $LiCoO_2$ was ground with the correspondent solid precursors in AGO-2 planetary mill and then heat treated at moderate temperatures. $LiCoO_2$ was coated with 1-5 % of Al_2O_3, TiO_2, MgO and $Li_2O{\cdot}2B_2O_3$, using $Al(OH)_3$, $TiO_2{\cdot}xH_2O$, $Mg(OH)_2$ and a mixture of LiOH with H_3BO_3 as the precursors.

Figure 14 shows SEM images of pristine $LiCoO_2$ and $LiCoO_2$ coated with Al_2O_3 (as an example) using MA and the precipitation solution method for the comparison. The particles of pristine $LiCoO_2$ were about 5-10 μm in size and nonporous with smooth facets. Surface modification by MA method led to formation of nanoparticulate uniform coating comparable with that prepared by the solution method. According to XRD, no detectable changes were found in the cell parameters of $LiCoO_2$ after the coating process (MA + heating at 400 °C) evidencing that the particle bulk is free from dopants and indicating that the coating oxides either form solid solution on the surface of the particles or present in amorphous or nanoparticulate state.

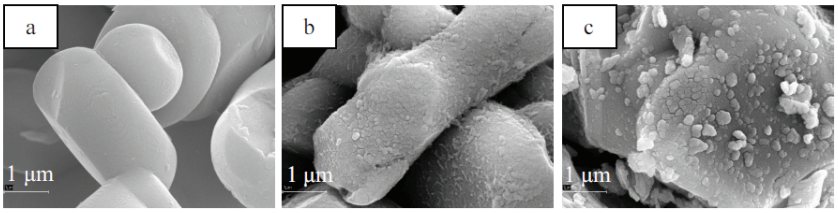

Figure 14. SEM images of pristine (a) and Al_2O_3-coated $LiCoO_2$ prepared by solution (b) and by MA (c) methods.

The surface of the pristine and the coated samples of $LiCoO_2$ was analyzed by XPS before and after Ar^+-ions etching for 30 min with energy of 2.4 keV [26]. In the XPS Co*2p* core-level spectra, two sharp Co$2p_{3/2}$ and Co$2p_{1/2}$ peaks and two low-intensive shake-up satellites are

observed. Such spectrum is a characteristic of $LiCoO_2$ with Co^{3+} ions. For the coated $LiCoO_2$ samples, Mg *1s*, Ti *2p3/2*, Al *2s*, B *1s* and O *1s* spectra were recorded. In the B *1s* spectrum of the $Li_2O{\cdot}2B_2O_3$ coated sample, a sharp line at 192.2 eV is observed, while an intensive peak at 531.9 eV with a weak shoulder at 530 eV is present in the O *1s* spectrum. These data are very close to those published for B_2O_3 (192.4 eV for B *1s* and 531.7 eV for O *1s*). Atomic ratio [B]/[Co] is equal to 20 and decreases to 0.5 after Ar etching evidencing that boron compound is located preferably on the surface. In the MgO-coated $LiCoO_2$ spectrum, the binding energy of Mg *1s* is equal to 1302.9 eV, characteristic of Mg^{2+} ions. In the spectrum of O *1s*, three lines at 529.2, 531.3 и 532.8 eV are observed. The first line can be assigned to oxygen in MgO and $LiCoO_2$. The binding energy of Mg *1s* and O *1s* in MgO correspond to 1303.6-1304.2 and 530.5-530.6 eV, respectively. The line at 532.8 eV is characteristic of $Mg(OH)_2$. Atomic ratio [Mg]/[Co] is equal to 0.72 and decreases to 0.26 after Ar etching. In the Ti *2p3/2* spectrum of the TiO_2-coated $LiCoO_2$ sample, a symmetric peak at 458.4 eV is observed. It is close to the value found for TiO_2 (458.3-458.7 eV). Atomic ratio [Ti]/[Co] is equal to 0.86 and decreases to 0.27 after Ar etching. Because of partial overlapping of Co *3p* and Al *2p* spectra, the Al *2s* spectrum is preferable for quantitative analysis and determination of a chemical state of Al. The XPS Al *2s* core-level spectrum of the coated sample represents a symmetric peak with a maximum at 118.2±0.1 eV typical for Al^{3+}. However, it differs from that of α-Al_2O_3. The closer value was observed, for example, for AlOOH with Al ions in disordered octahedral coordination. Atomic ratio [Al]/[Co] is equal to 0.2 and sharply decreases to 0.05 after Ar etching.

^{27}Al MAS NMR spectrum of the $LiCoO_2/Al_2O_3$ sample prepared at 400 °C consists of the intensive asymmetric peak with a maximum at 4.8–6.2 ppm and two less intensive ones at ~55-56 and ~61-62 ppm (Fig. 15) [27]. Areas of these two signals correspond to 2.6:1. On the other hand, a spectrum of the 800 °C-sample has no peak near 0 ppm, but has a series of peaks with a regularly changed intensity located in the range of 26-62 ppm with an interval of about 7 ppm: 25.9 ppm, 32.6 ppm, 40.2 ppm, 47.2 ppm, 54.7 ppm, 61.4 ppm, similar to those observed for the $LiCo_{1-x}Al_xO_2$ solid solutions. These peaks were assigned to $[Al]_{Oh}$ with different next-nearest-neighbor environment of the resonating Al ions ranging from 6 to 0: 20 ppm (0Co6Al), 28 ppm (1Co5Al), 35 ppm (2Co4Al), 42 ppm (3Co3Al), 48 ppm (4Co2Al), 55 ppm (5Co1Al), 62.5 ppm (6Co0Al). Thus, it can be concluded that the 'shell' of the 400 °C-sample consists of the amorphous aluminium oxyhydroxide. However, the initial chemical interaction between the 'core' and the 'shell' already occurs, making the coating more adherent. As the temperature increases up to 800 °C, all aluminum ions diffuse into the surface layer of $LiCoO_2$ particles,

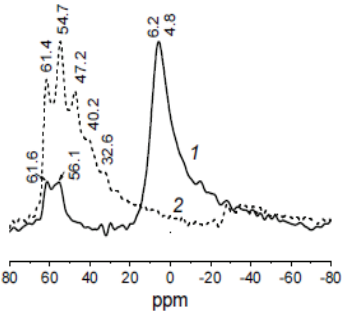

Figure 15. ^{27}Al NMR spectra of the Al_2O_3-coated $LiCoO_2$ samples annealed at 400 (1) and 800 °C (2).

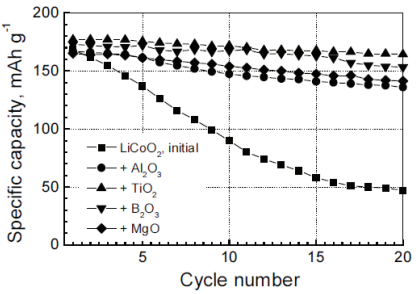

Figure 16. Specific discharge capacity of pristine and coated $LiCoO_2$ vs. cycle number in the 3–4.5 V range.

substituting for Co and forming the $LiCo_{1-y}Al_yO_2$ solid solution. Thus, the degree of chemical interaction between the 'shell' and the 'core' depends on the temperature of heat treatment and results in different thickness and composition of the 'shell'.

Electrochemical testing shows an improved cyclability in the 3-4.5 V range and a significant increase in discharge capacity (> 150 mAh/g) for $LiCoO_2$ coated with Al_2O_3, TiO_2, MgO and $Li_2O \cdot 2B_2O_3$ ($T_{synth.}$ = 400 °C) as compared with the pristine $LiCoO_2$ (Fig. 16). Perhaps, the amorphous surface layers are favorable for Li^+-diffusion, superior to more crystalline layers, and the coating brings to surface stabilization by smoothing the active edge surfaces and removing the surface active centers.

$LiMO_2$ (M=Co, Ni)-coated $LiMn_2O_4$

$LiMn_2O_4$ is a very promising cathode material with economical and environmental advantages over the layered compounds such as $LiCoO_2$ and $LiNiO_2$. A good thermal stability of $LiMn_2O_4$ is a positive factor for its use in LIBs for electric vehicles. However, $LiMn_2O_4$ exhibits a severe capacity fade at the elevated temperatures and insufficient rate capability due to lower electric conductivity as compared with $LiCoO_2$ (10^{-6} vs. 10^{-2} S cm^{-1}). To enhance rate capability, the coating of $LiMn_2O_4$ with $LiMO_2$ (M = Co, Ni) by different coating technique has been investigated [28]. In the present study, we used a facile and convenient solid state mechanochemical process to modify the surface of $LiMn_2O_4$.

To prepare $LiMn_2O_4$ surface-modified with 1-5 % of $LiCoO_2$ and $LiNi_{0.8}Co_{0.2}O_2$, the initial spinel was ground in an AGO-2 mill using the mixtures of solid LiOH with $Co(OH)_2$ or $Ni_{0.8}Co_{0.2}(OH)_2$ in the correspondent ratios and then heat treated at 400-750 °C [29]. Figure 17 presents SEM images of spinel before and after coating. The particles of pristine $LiMn_2O_4$ are about 0.5 μm in size with cubic form and nonporous. The coating process using MA leads to decrease in particle size up to *ca.* 100 nm similar to the solution precipitation method.

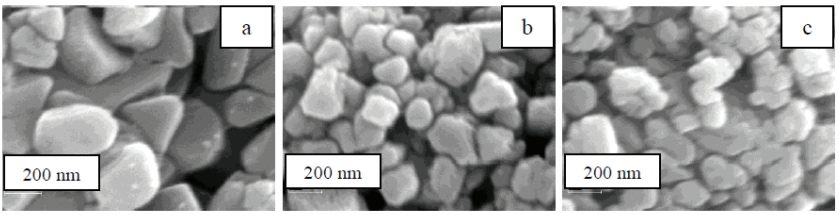

Figure 17. SEM images of pristine (a) and $LiCoO_2$-coated $LiMn_2O_4$ by solution (b) and by MA (c) methods.

According to XRD, the lattice parameter of the coated $LiMn_2O_4$ decreases from 0.8242 nm to 0.8231 nm for the Li-Co-O coating and to 0.8232 nm for the Li-Ni-Co-O coating after annealing at 400 °C and then increases to 0.8236 and 0.8237 nm, respectively, after annealing at 750 °C. XPS data show that the main oxidation state of the cobalt and nickel ions is 3+. The intensity of the Co$2p_{3/2}$ and Ni$2p_{3/2}$ peaks decreases with the annealing temperature and after Ar etching. The Mn$2p_{3/2}$ peaks in the spectra of the coated samples become wide and slightly asymmetric. A shoulder at low binding energy evidences the presence of both Mn^{3+} and Mn^{4+} ions. However, the modification of $LiMn_2O_4$ results in a decreased surface concentration of Mn^{3+} ions. As the annealing temperature increases, the [M]/[Mn] ratio decreases. After Ar etching, it

noticeably decreases for the samples annealed at 400 °C, while it keeps practically unchanged for the samples treated at 750 °C, indicating that the formation of Co- and Ni-rich 'shell' occurs at the moderate temperatures, while diffusion of the 'shell' ions (especially, Ni ions) into the bulk takes place at the elevated temperatures.

The $LiCoO_2$ and $LiNi_{0.8}Co_{0.2}O_2$-coated spinel electrodes show two plateaus during charge-discharge, characteristic of $LiMn_2O_4$; good cycling stability and improved high-rate capability as compared with pristine spinel (Fig. 18). It might be supposed that these improvements are due to a decrease in the particle size and better electronic and ionic transport at the modified surface electrolyte interface.

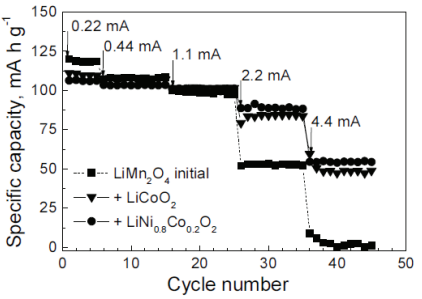

Figure 18. Specific discharge capacity of pristine and coated $LiMn_2O_4$ vs. the cycle rate.

CONCLUSION

Thus, we proposed a new avenue towards the development of novel nanostructured composite electrode materials with more balanced characteristics as compared with the individual components using a high-energy solid-state mechanical activation.

ACKNOWLEDGEMENT

The author is thankful to Dr. A.B. Slobodyuk, Dr. V.V. Kaichev, Dr. A.T. Titov, Dr. A.K. Gutakovskii, E.T. Devyatkina, A.V. Markov, S.A. Petrov for their participation in the investigations, and Helmholtz Association for the experiments at the high-resolution powder diffraction beamline P02.1 at Petra III, DESY.

The work has been partially supported by the Russian Foundation for Basic Research (grant 14-03-01082).

REFERENCES

1. S.B. Chikkannanavar, D.M. Bernardi, and L. Liu, *J. Power Sources*, **248**, 91-100 (2014).
2. V.V. Boldyrev, *Usp. Khim.*, **75**, 203-216 (2006,).
3. E. Avvakumov, M. Senna, and N. Kosova, Soft Mechanochemical Synthesis: A Basis for New Chemical Technologies, *Kluwer Publ.*, Boston, Dordrecht, London, 2001.
4. K. Mizushima, P.C. Jones, P.J. Wiseman, and J.B. Goodenough, *Mater. Res. Bull.*,**15**, 783-789 (1980).
5. M.M. Thackeray, P.J. Johnson, L.A. de Picciotto, P.G. Bruce, and J.B. Goodenough, *Mater. Res. Bull.*, **19**, 179-187 (1984).
6. A. Yamada, M. Tanaka, K. Tanaka, and K. Sekai, *J. Power Sources,* **81-82**, 73-78 (1999).
7. Y. Xia, Y. Zhou, and M. Yoshio, *J. Electrochem. Soc.*, **144**, 2593-2600 (1997).
8. T. Numata, C. Amemiya, T. Kumeuchi, M. Shirakata, and M. Yonezawa, *J. Power Sources*, **97-98**, 358-360 (2001).
9. Z.F. Ma, X.Q. Yang, X.Z. Liao, X. Sun, and J. McBreen, *Electrochemistry Commun.*, **3**, 425-428 (2001).
10. P. Albertus, J. Christensen, and J. Newman, *J. Electrichem. Soc.*, **156**, A606-A618 (2009).
11. N.V. Kosova, E.T. Devyatkina, V.V. Kaichev, and A.B. Slobodyuk, *Solid State Ionics*, **192**, 284-288 (2011).
12. N.V. Kosova, and E.T. Devyatkina, *Elektrochimiya*, **48**, 351-361 (2012).
13. A.K. Padhi, K.S. Nanjundaswamy, and J.B. Goodenough, *J. Electrochem. Soc.*, **144**, 1188-1194 (1997).
14. H. Huang, S.C. Yin, T. Kerr, N. Taylor, and L.F. Nazar, *Adv. Mater.*, **14**, 1525-1528 (2002).
15. N.V. Kosova and E.T. Devyatkina, *Doklady Chemistry*, **458**, 194-197 (2014).
16. N.V. Kosova, E.T. Devyatkina, A.B. Slobodyuk, and S.A. Petrov, *Electrochim. Acta*, **59** 404-411 (2012).
17. N.V. Kosova, O.A. Podgornova, E.T. Devyatkina, V.R. Podugolnikov, and S.A. Petrov, *J. Mater. Chem. A*, **2**, 20697-20705 (2014).
18. N.V. Kosova, E.T. Devyatkina, A.I. Ancharov, A.V. Markov, D.D. Karnaushenko, and V.K. Makukha, *Solis State Ionics*, **22**, 564-569 (2012).
19. J. Barker, M.Y. Saidi, and J.L. Swoyer, *J. Electrochem. Soc.*, **150**, A1394-A1398 (2003).
20. N.V. Kosova, E.T. Devyatkina, A.B. Slobodyuk, and A.K. Gutakovskii, *J. Solid State Electrochem.*, **18**, 1389-1399 (2014).
21. T. N. Ramesh, K.T. Lee, B.L. Ellis, and L.F. Nazar, *Electrochem. Solid-State Lett.*, **13**, A43-A47 (2010).
22. J. Barker, R.K.B. Gover, P. Burns, A. Bryan, M.Y. Saidi, and J.L. Swoyer, *J. Electrochem. Soc.*, **152**, A1176-A117 (2005).
23. J.M. Ateba Mba, L. Croguennec, N.I. Basier, J. Barker, and C. Masquelier, *J. Electrochem. Soc.*, **159**, A1171-1175 (2012).
24. L.J. Fu, H. Liu, C. Li, Y.P. Wu, E. Rahm, R. Holze, H.Q. Wu, *Solid State Sciences*, **8**, 113 (2006).
25. N.V. Kosova and E.T. Devyatkina, *J. Power Sources*, **174**, 959-964 (2007).
26. N.V. Kosova, E.T. Devyatkina, V.V. Kaichev, and A.B. Slobodyuk, *ECS Trans.*, **16**, 21-29 (2009).
27. N. Kosova, E. Devyatkina, A. Slobodyuk, and V. Kaichev, *Solid State Ionics*, **179**, 1745-1749 (2008).

28. S.C. Park, Y.M. Kim, Y.M. Kang, K.T. Kim, P.S. Lee, and J.Y. Lee, *J. Power Sources*, **103**, 86-92 (2001).
29. N.V. Kosova, E.T. Devyatkina, V.V. Kaichev, and A.B. Slobodyuk, *Solid State Ionics*, **192**, 284-288 (2011).

COMPARATIVE STUDY OF POLYSULFIDE ENCAPSULATION IN THE DIFFERENT CARBONS PERFORMED BY ANALYTICAL TOOLS

Manu U. M. Patel and Robert Dominko
National Institute of Chemistry, Hajdrihova 19, SI-1000 Ljubljana, Slovenia

ABSTRACT

Despite the great efforts made for encapsulating sulfur particles with conducting materials, such as carbon black, in order to limit polysulfide diffusion in lithium-sulfur (Li-S) battery, the rapid degradation of Li-S batteries still occurs. The influence of the surface area and the porosity of the host carbon matrices on the battery performance, the active material utilization and the encapsulation of polysulfides are not fully understood. In this study, by using carbon host matrices with three different surface areas, we show the influence of host matrices on the Li-S battery performance. Analytical techniques, including UV-Visible spectroscopy and 4-Electrode Swagelok cells, were employed to study polysulfide diffusion from the cathode composite. Our studies revealed that the presence of high surface area host carbon can enhance the performance of the battery via the efficient utilization and encapsulation of sulfur and lithium polysulfides although complete encapsulation cannot be achieved.

INTRODUCTION

Sulfur is considered as a potential cathode material because of its high theoretical capacity of 1672 mAh g^{-1} and energy density of 2500 Wh kg^{-1}. The high capacity is based on the conversion reaction of sulfur to form lithium sulfide (Li_2S) by reversibly incorporating two electrons per sulfur atom, compared to one or less in the transition-metal ion insertion-oxide cathodes that are in use today. This electrochemistry of sulfur can provide threefold to fourfold greater energy density over conventional cathode electrode materials.[1] Researchers have been studying lithium-sulfur (Li-S) battery systems for two to three decades but commercialization and practical applications have not been possible. However, recently there has been a significant improvement in Li-S battery performance, due to the development of novel cathode materials, electrolytes and separators.[2-8] Sulfur/carbon, sulfur/polymer and nanostructured composites are some of the dominant types of composite cathodes in Li-S batteries that have shown promising performances with high capacity, enhanced rate capability, and long-term cycle stability[2,3,4]. Electrolytes with the desired properties and different types of additives also have played a somewhat significant role in solving the

problems of Li-S batteries.[5,6] In addition, carbon interlayer[7], functionalized interlayer[8] and ion-selective membranes[9] have significantly improved the cycling performance of Li-S batteries.[2,3]

The mechanism of sulfur reduction in the Li-S battery can be divided into three regions. High voltage plateau corresponds to the conversion of sulfur into long chain polysulfides which are soluble in the electrolyte. This is followed by transition from high voltage plateau to low voltage plateau (at 2.1V), where long chain polysulfides are reduced to shorter chains (so called liquid - liquid equilibrium) and finally third region is low voltage plateau which corresponds to reduction of polysulfides to short chain and constant precipitation of Li_2S (so called liquid – solid equilibrium). Formation of soluble polysulfides and concentration gradient inside the cell is the major factor for fast capacity degradation. One of possible directions for preventing polysulfide diffusion is encapsulation of sulfur.

In order to effectively encapsulate the sulfur and its redox products formed during battery operation, the most studied and used host matrix has been carbon.[2-5] One of the important reasons for using carbon as a host to encapsulate sulfur and its intermediate products is it is a highly conductive material, which is essential in the case of Li-S batteries as sulfur and intermediate polysulfides are electronic insulators. The other reasons for using carbon include the possibility of adapting the surface area, shape, size and porosity (macro-, meso- and microporous) depending upon the particular electrode requirement.[10,11,12,13] Based on these criteria, much research has recently been done on carbon-based electrode materials for Li-S batteries.

In this study, we consider carbon blacks with different surface areas as host matrices to encapsulate sulfur and its intermediates, and we monitor the electrochemical performance of these cathode electrodes. Electrochemical measurements of electrodes, which were prepared by mixing carbon blacks of different surface areas, will be considered in order to determine how the mixing of two carbon blacks with different surface areas affects battery performance. The carbon composites with different surface areas were analyzed for their polysulfide encapsulation properties by employing UV-Visible spectroscopy[14] (UV-Vis) and 4-electrode Swagelok cell[15] analytical techniques.

EXPERIMENTAL

Preparation of cathode composites by using carbon blacks of different surface areas

Four types of carbon black samples with different surface areas were used in this work. The carbon black MAXSORB (denoted as MAX) with the highest surface area of 3000 $m^2 g^{-1}$ was obtained from Kansai Coke and Chemicals Japan. Carbon black PRINTEX XE2 (denoted as PRX) with a surface area of 950 $m^2 g^{-1}$ was obtained from Degussa. Vulcan (denoted as Vul) carbon black with a surface area of 250 $m^2 g^{-1}$ was obtained from the CABOT Corporation and Super C65 (denoted as Tim) carbon with a surface area of 60 $m^2 g^{-1}$ was obtained from TIMCAL.

All the obtained carbon black samples were used to make composites with sulfur. A weight ratio of 1:1 of the abovementioned carbon blacks and sulfur was balled milled for 30 minutes at 300 rpm. The obtained mixtures were then heated to 155 °C for 6 hours in an argon atmosphere to encapsulate sulfur in the carbon black. After cooling to room temperature, the samples were recovered and the quantitative content of S was checked via elemental analysis (CHNS). The presence of 48–50 wt.% of sulfur in the composites was confirmed in all the composites.

Preparation of electrodes from the composites

Electrodes were prepared by making a slurry of composites, Polyvinylidene fluoride binder (PVdF) and carbon black (the same carbon black used for the preparation of respective composite was used as additive carbon while preparing the electrode) in N-Methyl-2-pyrrolidone solvent with a wt.% ratio of 85:7:8, respectively. The slurry was then cast on the surface of aluminum foil, using the doctor blade technique. The obtained electrodes were dried and used further.

Battery assembly and electrochemical characterization

Dried electrodes were used to assemble coffee bag batteries in an argon-filled glove box, where 1 M lithium bis(trifluoromethanesulfonyl)imide (LiTFSI) in sulfolane was used as electrolyte. Pure lithium metal foil was used as anode electrode. The sulfur loading was 1.5–2.5 mg cm^{-2} among the electrodes. Electrodes were separated with a glass fiber separator (Whatman 150) and the amount of electrolyte used in all experiments was normalized per active mass at 75 µL per mg of S. Galvanostatic cycling was performed at room temperature by using a Bio-Logic VMP3 instruments with a current density of 167.5 mA g^{-1} in the potential window between 3 V and 1.5 V versus metallic lithium at C/10 rate. Coulombic efficiencies for the measurements were calculated as a ratio between discharge capacity and charge capacity obtained from previous charging.

In operando UV-Vis battery assembly and characterization

The pouch polymer bag with a sealed glass cover[14] was used to prepare the *in operando* battery. The configuration of the assembled battery was as follows: a glass fiber separator was placed onto the surface of the cathode, and this separator was wetted with a quantified amount of electrolyte per 1 mg of S in the electrode. The lithium foil with a hole was placed on the separator, and the sandwich was then sealed inside the pouch polymer bag cell in a vacuum sealer in such a way that there was no lithium present between the glass cover and the cathode that was present below the separator; therefore, the UV-Vis spectra could be obtained without any interference. This configuration enabled the detection of polysulfides in the separator of the battery. The cell was then attached to a UV-Vis spectrometer (Perkin-Elmer Lambda 950) in such a way that the UV light was directly focused on the glass cover of the cell; the whole setup was completely covered by a thick black plastic bag to avoid interference of the light from the surroundings. After taking the initial spectra of the battery, the cycling of the battery was started by using a potentiostat (Biologic SP-200). The batteries were cycled at a rate of one electron C/20 for one complete cycle. Spectra were recorded at a frequency of every 15 minutes in the reflection mode during the battery discharge/charge.

4-Electrode Swagelok cell cathode preparation, cell assembly and measurements

The obtained composites from MAX, PRX and Vul were mixed with corresponding carbon black, from which the composite was prepared in a weight ratio of 9:1 before being used as electrodes for 4-electrode cell measurements. In our work, we used stainless steel and platinum wire as electrodes to measure cyclovoltammograms in the 4-electrode Swagelok cell. The batteries were assembled using two glass fiber separators in such a way that the aforementioned stainless steel and platinum wire came between these two glass fiber separators. Separators were wetted with a quantified amount of electrolyte depending upon the mass of S in the composite. Lithium foil was used as anode electrode and a known weighed amount of cathode was taken in powder form because no binder was used to make electrodes. An open circuit voltage (OCV) between the stainless steel and platinum wires was typically 2.5 V. Electrochemistry in the 4-electrode cell was tested simultaneously on two channels using a VMP3 galvanostat/potentiostat (Biologic, S.A., Claix, France). Before starting the reduction of sulfur, we measured the cyclovoltammogram between stainless steel (working electrode) and platinum (counter electrode) wires with a scan rate of 2 mVs^{-1} over the 2.5 V–0.5 V versus platinum reference electrode. During this measurement,

the Li-S battery was on OCV mode; as soon as the CV scan was completed, the galvanostatic measurement of the Li-S battery was initiated for 2 h with a current density corresponding to a C/20 cycling rate. Measurements were repeated in this sequence until the battery reached the cut-off voltage of 1V versus metallic lithium.

RESULTS AND DISCUSSION

The samples used in this study had different surface areas and pore volumes, as shown in Table 1. We prepared mixtures of carbon host matrix and sulfur in a 1:1 ratio; electrodes used for electrochemical characterization were prepared in the same manner; all the batteries were cycled at same C-rate and room temperature.

Table 1 Types of carbon blacks used their surface areas and pore volume.

Serial Number	Carbon Black name	Pore volume	Surface area
i.	MAXSORB (Max).	179 cm^3/100mg	3000 m^2/g
ii.	PRINTEX XE2 (Prx).	380 cm^3/100mg	950 m^2/g
iii.	Vulcan (Vul).	180 cm^3/100mg	280 m^2/g
iv.	Super C65 (Tim)	-	60 m^2/g

In our experiments, we used batteries that had electrodes prepared by using only one type of carbon black, i.e. the carbon used in the preparation of composite is same as the carbon used for improving conductivity. The capacities obtained from all the battery measurements are shown in Figure 1. By increasing surface area of the carbon black, the capacity obtained from the battery also increased considerably. However, there was not much difference in obtained coulombic efficiencies.

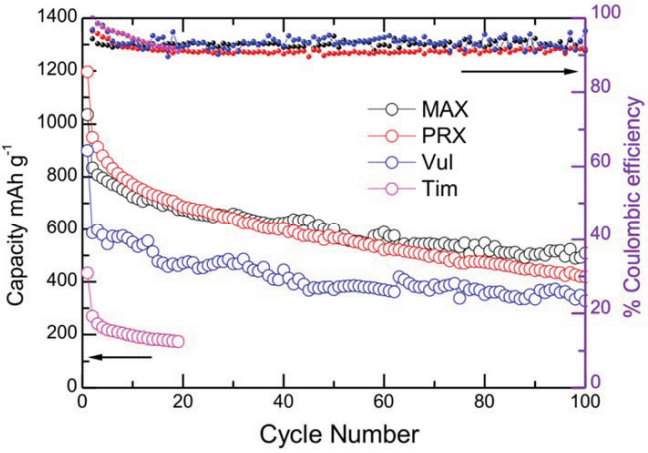

Figure 1. Discharge capacity (left axis) and columbic efficiency (right axis) from the composites prepared by using carbon black with different surface areas.

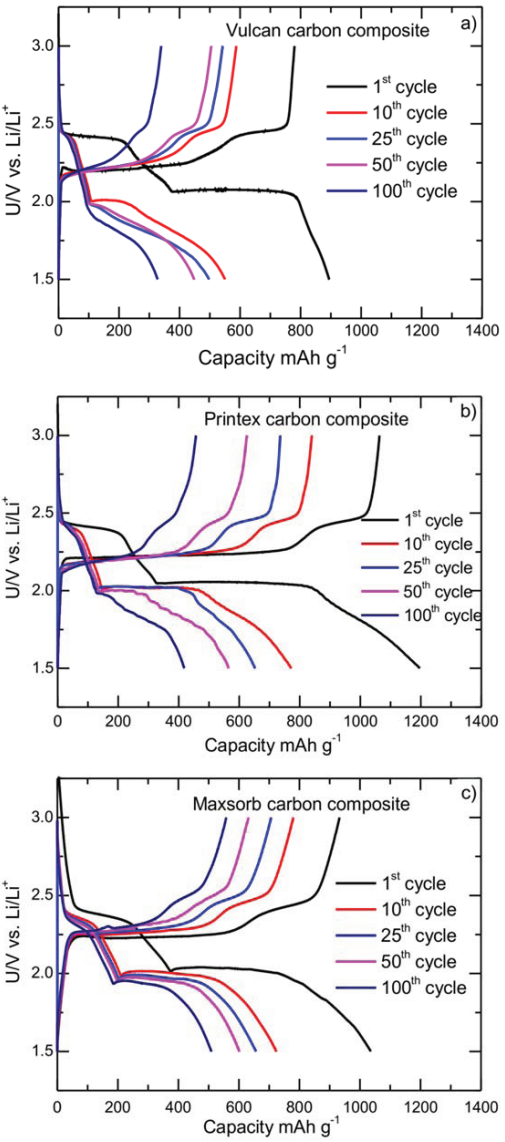

Figure 2. Electrochemical discharge/charge curves of selected cycles from a) Vul carbon/S composite electrode, b) PRX carbon/S composite electrode and c) MAX carbon/S composite electrode.

The lowest capacity was obtained from the carbon black with the lowest surface area, i.e. 60 $m^2 g^{-1}$. The average capacity increased from 200 mAh g^{-1} to 450 mAh g^{-1} when the surface area of the carbon black was increased from 60 $m^2 g^{-1}$ to 250 $m^2 g^{-1}$. The average capacity obtained in the case of carbon blacks with high surface areas of 900 $m^2 g^{-1}$ and 3000 $m^2 g^{-1}$ was 600 mAh g^{-1}. The obtained capacities from the high surface area carbon blacks show that once the surface area of the host carbon matrix reached a certain point, there was no influence of surface area on the obtainable capacity. The possible reason for this could be that once the surface area required for the electrochemical reaction (conversion of S_8 to lithium polysulfides) reaches a certain point (around 1000 $m^2 g^{-1}$), the surface area may not influence the obtainable capacity from the battery. Another explanation could be in the very similar overall porosity of both samples. However, increasing surface area may have some effect on adsorption or encapsulation of the dissolved, diffusing lithium polysulfides. This, in turn, may have an influence on the battery cycle life as well as on the battery performance.

The electrochemical charge/discharge curves from the selected cycles of the carbon black/S composites were examined. We did not consider the Tim carbon electrochemistry as the obtained capacity was very low. It can be seen that the electrode with Vul carbon black, which had a low surface area, started to deteriorate soon after the first cycle Figure 2a.

The capacity obtained from the high voltage plateau dropped from 400 mAh g^{-1} to less than 100 mAh g^{-1} between the 1st cycle and the 10th cycle. The capacity obtained from the high voltage plateau almost remained the same between the 10th cycle and the 100th cycle. It can also be seen from the electrochemical curves that, with cycling, the capacity obtained from the low voltage plateau starts to decrease rapidly along with the increasing polarization. In the case of PRX carbon (Figure 2b) the capacity obtained at the high voltage plateau dropped from 350 mAh g^{-1} to 150 mAh g^{-1} between the 1st and the 10th cycle. The capacity obtained from high voltage plateau after the 10th cycle remained the same throughout cycling, which was similar to the Vul carbon electrode. However, the polarization of this electrode was slightly better in comparison to Vul carbon. The MAX carbon, in contrast, had an initial capacity of the high voltage plateau of 400 mAh g^{-1}, and the capacity dropped by 200 mAh g^{-1} between the 1st cycle and the 10th cycle. The difference between MAX electrodes (Figure 2c) and other electrodes starts to appear only after the 10th cycle. As can be seen, the capacity obtained from the high voltage plateau of MAX carbon was above 200 mAh g^{-1} between the 10th and the 100th cycle. The increase in polarization was the least when compared to the other two electrodes. The increase in 100 mAh g^{-1} capacity in the high

voltage plateau was an indication that the MAX carbon with a high surface area was able to retain the polysulfides more efficiently than the other two electrodes.

To better understand the observed differences in the electrochemical signatures, we performed an analysis of the composite electrodes prepared from different surface area carbon matrices by using analytical techniques: UV-Vis spectroscopy and a 4-electrode Swagelok cell.

At first, *in operando* UV-Vis spectroscopy was used to analyze the electrodes prepared from composites using different surface areas. Figures 3, 4 and 5 shows the UV-Vis spectra obtained from the *in operando* measurements of all three types carbon composites with different surface areas.

The obtained spectra were in agreement with our other previous *in operando* measurements.[16] Initially, we did not observe any absorption shift from the separator of the battery as there was no polysulfide in the separator. With the electrochemical reduction of sulfur and the expected appearance of polysulfides, we observed the formation of the shift of the absorption edge towards higher wavelengths. With continuous discharge, the absorption was moved to shorter wavelengths (shift of colors in Figures 3a, 4a and 5a from red to green to blue), suggesting the formation of polysulfides with shorter chain lengths. The opposite shift in the absorption curve can be observed during the battery charging (Figures 3b, 4b and 5b).

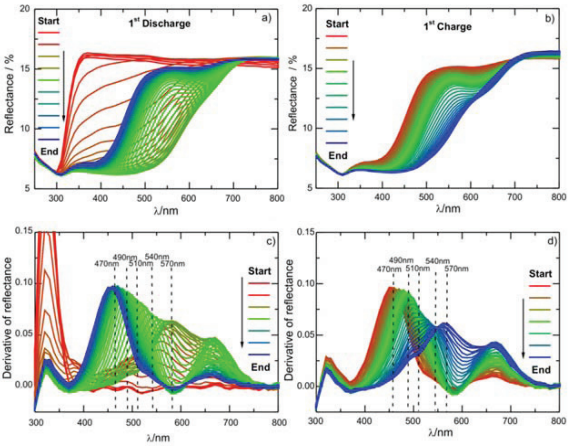

Figure 3. UV-Vis spectra measured *in operando* mode during the 1st cycle of the Li-S battery with MAX/S composite and 1 M LiTFSI in sulfolane electrolyte: a) all spectra measured during discharge, b) all spectra measured during charge, and c,d) corresponding first-order derivatives of the UV-Vis spectra (the color change in all figures from the start to the end is from red through green to blue).

An even clearer picture of the dynamics within the separator can be obtained from the first-order derivatives (Figure 3c and 3d, Figure 4c and 4d and Figure 5c and 5d) of the measured UV-Vis spectra. A continuous shift of the derivative peaks from high to short wavelengths can be observed in all the measurements form the composites. We focused on the wavelength range between 650 and 400 nm, because we observed changes in the derivative peak position in this region. The major positions of derivative peaks were in agreement with the peaks observed from the derivatives of catholyte solutions of sulfolane, as previously reported. [14,16]

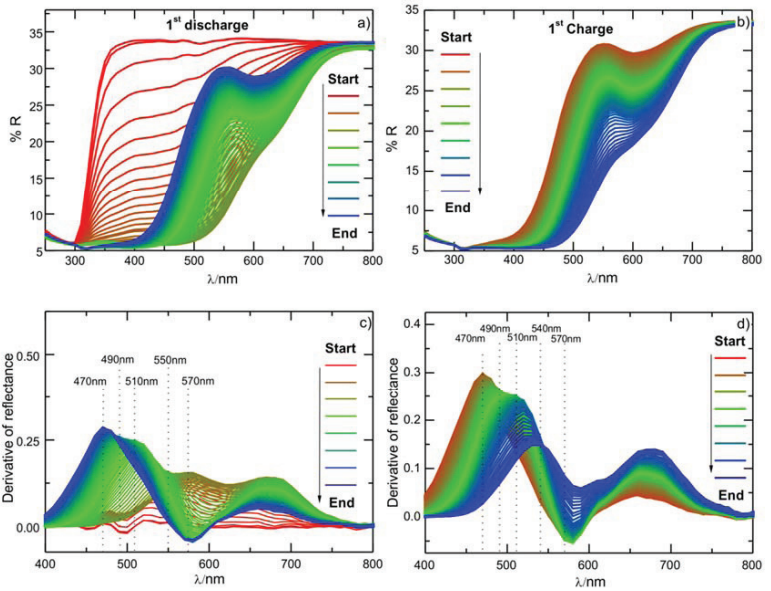

Figure 4. UV-Vis spectra measured *in operando* mode during the 1st cycle of the Li-S battery with PRX/S composite and 1 M LiTFSI in sulfolane electrolyte: a) all spectra measured during discharge, b) all spectra measured during charge, and c, d) corresponding first-order derivatives of the UV-Vis spectra (the color change in all figures from the start to the end is from red through green to blue).

All the three measured UV-Vis spectra looked relatively similar to each other. However, they did show some significant differences when we performed deconvolution of the obtained spectra. Our focus was on the qualitative and quantitative determination of polysulfides, which can provide us information about the mechanism of polysulfide formation and diffusion in the presence of different host matrices. The deconvolution of the obtained spectra was carried out as mentioned in our previous work.[16]

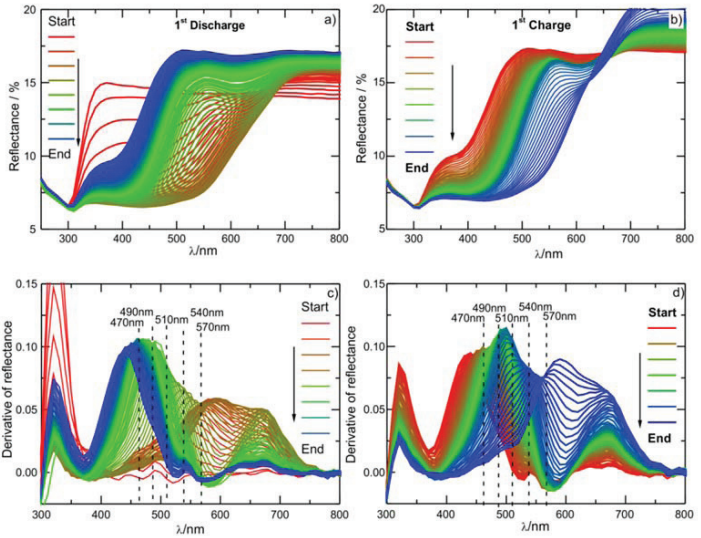

Figure 5. UV-Vis spectra measured *in operando* mode during the 1st cycle of the Li-S battery with Vul/S composite and 1 M LiTFSI in sulfolane electrolyte: a) all spectra measured during discharge, b) all spectra measured during charge and c, d) corresponding first-order derivatives of the UV-Vis spectra (the color change in all figures from the start to the end is from red through green to blue).

Figure 6 shows a comparison of polysulfide evolution in the separators of batteries with electrodes prepared from three different composites. Batteries were measured at a cycling rate of C/20 during the first discharge and charge. Deconvolution of the UV-Vis spectra measured in PRX, MAX and Vul composites showed saturation of the electrolyte with long-chain polysulfides (recalculated concentration from intensities at 570 nm) with a maximum concentration of ~14 mM, 8 mM and 12 mM respectively, at the end of the high-voltage plateau. With a continuous discharge, we observed a decrease in the concentration for long-chain polysulfides and an increase of concentration of mid-chain polysulfides (recalculated concentrations form intensities at 550 nm and 510 nm). The concentration of mid-chain polysulfides reached values between 1.5–2 mM for PRX, 0.75–1.5 mM for MAX and 1.5–4 mM for the Vul composite in the middle of the low voltage plateau. After the evolution of mid-chain polysulfides, we noticed the increase of short-chain polysulfides (recalculated concentrations form intensities at 490 nm and 470 nm), reaching the maximum values of ~2 mM for PRX, 1.5 mM for MAX and 1.75 mM for Vul at the end of the discharge.

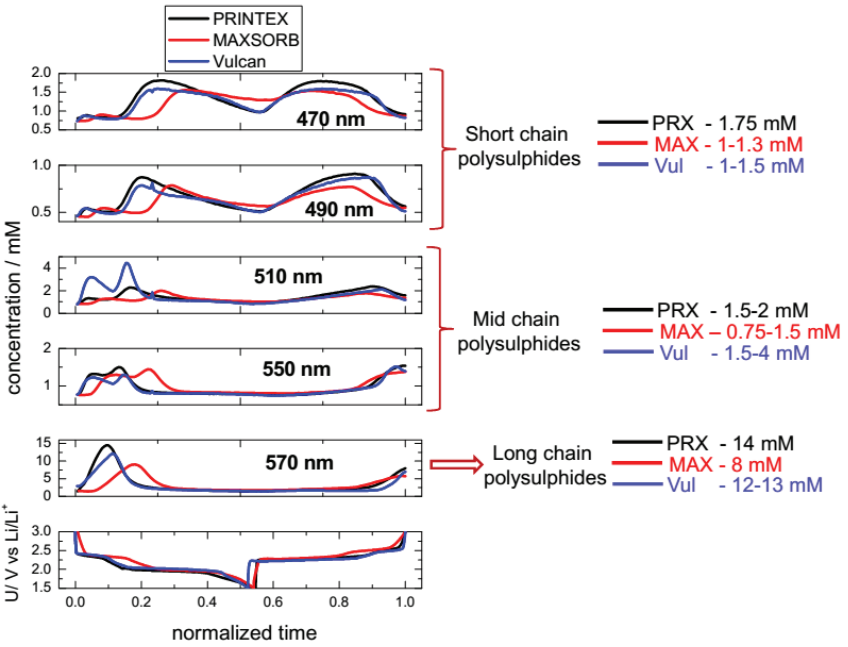

Figure 6. Recalculated concentrations of short-, mid- and long-chain polysulfides detected in the separators of the battery from three types of composites. The black line corresponds to the measurement with PRX composite, the red line corresponds to MAX composite measurement, and blue line corresponds to measurement with Vul composite with 1 M LiTFSI sulfolane electrolyte.

Based on the different modes of polysulfide formation in the composites used in this study, we can correlate capacity fading with differences in the concentration of formation of long-chain polysulfides in the separator. The higher diffusion concentration of polysulfides found in case of the PRX- and Vul-based composites can lead to higher irreversible losses of active material on the surface of the metallic lithium. We correlate this with faster capacity degradation in the battery assembled with PRX and Vul composites. When comparing it to the MAX composite, we found a minimum concentration of polysulfides in the separator at almost all potentials, starting from a longer wave number to a shorter wave number, indicating better encapsulation of lithium polysulfides because of its high surface area carbon, which led to better battery cycling.

A 4-Electrode Swagelok cell was used as another analytical tool to make a comparative study of the composites with different surface area carbon blacks to obtain further information about the influence of high surface area on polysulfides encapsulation properties.

The results obtained from battery measurements are shown in Figure 7; the a,c,e (solid line) shows the discharge curves in the first cycle, and the corresponding CVs measured during the battery relaxation are shown in the Figure 7 b,d,f. A reduction peak at Up≈1.8 V versus platinum is observed at every CV measurement. An integration of this peak in the 2.25 V–1.5 V range gives the cumulative charge, which is plotted in Figure 7 a,c,e (violet, green and blue spheres). The results show that soluble polysulfides are formed at the beginning of the discharge, but diffuse at the later stages of the discharge. The partial cumulative charge associated with the soluble polysulfides increases slightly at the beginning, reaches the maximum at a nominal composition of $Li_{0.4}S$, and then decreases gradually in the cases of Vul and PRX carbon composites.

However, it can be observed that the obtained cumulative charges of these batteries were different from each other. In case of Vul carbon black (low surface area), we observe a gradual increase of cumulative charge to 0.3 μAh at a nominal composition of $Li_{0.4}S$. After reaching the maximum cumulative charge value at $Li_{0.4}S$, it starts to decrease; by the end of the discharge cycle, it reached a minimum value of 0.1 μAh. This was an indication that the polysulfide that diffused into the separator during the discharge did not completely return to the carbon matrix, and a relatively high amount of polysulfides was left behind in the separator that resulted in the higher cumulative charge of the battery. When we compared this with PRX carbon composite, the cumulative charge reached a maximum value of 0.32 μAh at a nominal composition of $Li_{0.4}S$. Soon after this, with continuous discharge, the cumulative charge sharply dropped almost to its initial state. This demonstrates that even though the polysulfides diffused into the separator during the initial stage of discharge, most of the polysulfides returned from the separator as they were encapsulated into the carbon matrix. This shows that there was slight improvement in the encapsulation of polysulfides with the increasing surface area of PRX over Vul carbon.

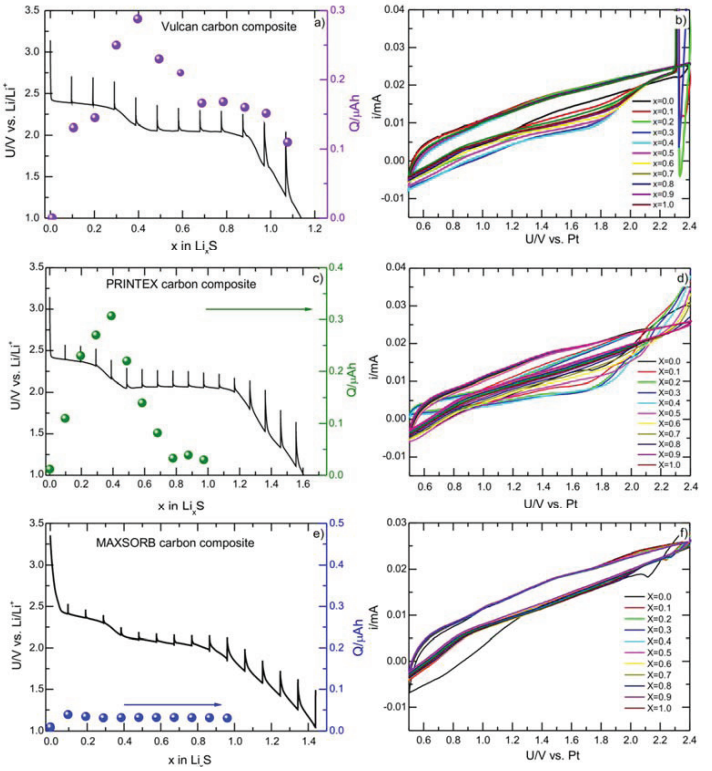

Figure 7. a,c,e) Electrochemical behavior during the first reduction of carbon/S composites with different surface areas and cumulative charges obtained by the integration of individual CV scans. b,d,f) Corresponding CV scans measured for each $\Delta x = 0.1$ change of composition in Li_xS.

We consider the carbon composite with the highest surface area (MAX). While discharging the battery, we did not see any increase in the cumulative charge because of the polysulfide diffusion into the electrolyte. The cumulative charge remained almost unchanged throughout the discharge cycle. This was an indication that the carbon black in this composite was able to encapsulate lithium polysulfides more efficiently than the other two carbon black composites that were measured earlier in this set of experiments.

We obtained similar kind of results from *in operando* UV-Vis measurements, which supports the claim that high surface area of the carbon in the composite influences the S utilization and lithium polysulfide encapsulation.

CONCLUSION

Our comparative study indicates that the presence of a high surface area in the host matrix can greatly influence the utilization of active material and the encapsulation of lithium polysulfides. From the above set of measurements, it is clearly evident that for the electrochemical reaction to occur in an efficient way, the surface area of the carbon black plays a somewhat significant role, after which the presence of a high surface area may not influence the active material utilization. A higher surface area plays a very important role in encapsulating the lithium polysulfides. The presence of a high surface area definitely reduced the diffusion of lithium polysulfides, which improved the overall battery performance and battery life, as seen in the above discussion. The analytical tools used in our work also revealed the influence of a high surface area of the host matrix on the polysulfide encapsulation properties. Both UV-Vis and the 4-electrode Swagelok cells showed that the polysulfide diffusion declined to great extent with the increasing surface area of the host matrix. Our work summarizes the advantages and influences of high surface area host matrix in the Li-S battery cathode electrode.

ACKNOWLEDGEMENTS

This research was funded by the Slovenian Research Agency and the European Union Seventh Framework Programme under grant agreement No. 314515 (EUROLIS).

REFERENCES

[1] P.G. Bruce, S.A. Freunberger, L.J. Hardwick, J-M. Tarascon, *Nat. Mat.*, 11, 19-29 (2012)

[2] S. Eversand, L. Nazar, *Acc. Chem. Res.*, *46*(5), 1135–1143, (2013).

[3] A. Manthiram, Y. Fu, and Y-S. Su, *Acc. Chem. Res.*, *46*(5), 1125–1134 (2013).

[4] Y-X. Yin, S. Xin, Y-G. Guo, and L-J. Wan, *Angew. Chem. Int. Ed.*, 52, 2–18 (2013).

[5] A. Manthiram,Y. Fu, S-H. Chung, C. Zu, and Y-S. Su, *Chem. Rev.*, dx.doi.org/10.1021/cr500062v.

[6] J. Scheers, S. Fantini, P. Johansson, *J. Power Sources*, 255, 204-218 (2014).

[7] Y-S. Su & A. Manthiram, *Chem. Commun.*, 48, 8817–8819 (2012).

[8] A. Vizintin, M. U. M. Patel, B. Genorio, and R. Dominko, *ChemElectroChem.*, 1(6), 1040–1045 (2014).

[9] J-Q. Huang, Q. Zhang, H-J. Peng, X-Y. Liu, W-Z. Qian and F. Wei, *Energy Environ. Sci.*, 7, 347-353 (2014).

[10] C. Zhang, H.B. Wu, C. Yuan, Z. Guo, X.W. Lou, *Angew. Chem., Int. Ed.*, 51, 9592−9595 (2012).

[11] R. Elazari, G. Salitra, A. Garsuch, A. Panchenko, D. Aurbach, *Adv. Mater*., 23, 5641-5644 (2011).

[12] F-F. Zhang, X-B. Zhang, Y-H. Dong, L-M. Wang, *Mater, Chem.*, 22, 11452-11454 (2012).

[13] J. Guo, Y. Xu, C. Wang, *Nano Lett.*, 11, 4288–4294 (2011).

[14] M.U.M. Patel, R. Demir-Cakan, M. Morcrette, J-M. Tarascon, M. Gaberscek, R. Dominko, *ChemSusChem.*, 6, 1177-1181 (2013).

[15] R. Dominko, R. Demir-Cakan, M. Morcrette, J.-M. Tarascon, *Electrochem. Commun.*, 13, 117–120 (2011).

[16] M.U.M. Patel and R. Dominko, *ChemSusChem*, 7, 2167–2175 (2014).

PERFORMANCE STUDY OF LI-ION BATTERY ELECTRODES DRIED USING INLINE MICROWAVE HYBRID SYSTEM

Ramesh D. Peelamedu and Donald A. Seccombe Jr.
BTU International
23 Esquire Road
North Billerica, MA USA

ABSTRACT

The interaction of microwave energy (MW) with battery binders and coating materials can dry the electrodes faster compared to conventional methods that are currently being used in the battery industry. The main objectives of this study are (i) to obtain proof of concept of the BTU's hybrid microwave process with minimal microstructure damage, and (ii) to demonstrate an acceptable coin cell performance prepared using MW dried electrodes. These electrodes were microwave dried under various conditions before they were measured for rate performance and cyclic testing. The moisture levels were measured using Karl-Fisher titration. The results showed that the electrodes prepared using NMP solvent had a much lower moisture levels when compared to electrodes prepared using an aqueous solvent. Presence of high moisture levels in aqueous based electrodes did not show any significant effects in cell performance tests.

INTRODUCTION

One of the cost barriers of high performance lithium ion battery electrodes is the high electrode processing costs in manufacturing[1-5]. By 2016, the aim of U.S. Advanced Battery Consortium is to reduce the plug-in hybrid electric vehicle battery cost to $200-$300/kWh[6]. Hence, manufacturing of advanced lithium ion battery systems for hybrid electric vehicles and plug-in hybrid electric vehicles are now driven towards development of low-cost design of electrode architectures. By 2015, it's aim to achieve $1700-$3400 for 100,000 PHEV units. Previously[7-10], studies have showed that processing steps towards higher performance has resulted in considerable cost benefits. In this paper, we propose use of a controlled microwave dryer for removal of water and organic solvents in both anodes and cathodes. As water, organic solvents and other electrode compositions are highly susceptive to microwave energy in a selective manner, this procedure could be very effective in terms of drying time and improved integrity.

The use of convection flotation drying technology to dry lithium ion battery electrodes can be extremely expensive due to the energy intensity of the air flotation requirements and the

operation of the solvent recovery system. In this study, we have conducted experiments towards the possibility of using this new microwave hybrid technology as a substitute to convection flotation drying systems that operates in air at atmospheric pressure. The footprint of the hybrid microwave system is considerably smaller and operates with a much lower thermal budget. The sequence of a Li-battery manufacturing process for prismatic cells would looks as follows:

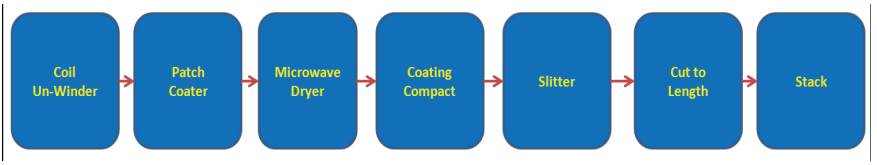

Figure 1 Typical process sequence in a Li-battery manufacturing facility

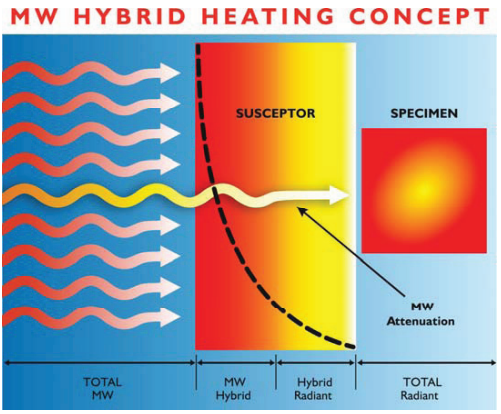

Figure 2: Concept of microwave hybrid heating

In microwave hybrid heating[11-14], simultaneous delivery of both heat and electromagnetic energy is entirely generated by one source, namely the microwave energy (Figure 2). This hybrid effect not only offers uniform heating, but also maintains a fairly uniform microwave field throughout the entire process zone. Since polar molecules in liquid can readily interact with microwave energy, the drying process can be done quickly and effectively. Additionally, solid compositions of the electrode can also interact with microwaves giving further boost to this

heating technology[15]. The equation for absorption by lossy materials[16] in a microwave field is expressed as

$$P = \omega[\epsilon_o \epsilon_r' tan\delta |E|^2 + \mu_o \mu_r' tan\varphi |H|^2]$$

In the above equation, $\omega = 2\pi f$, where f is the microwave frequency, $\epsilon_o = 8.86 \times 10^{-12}$ F/m is the dielectric constant of free space, μ_o = 1.256 × 10^{-6} H/m is the permeability of free space, ϵ_r' is the relative dielectric constant of the material, μ_r' is the relative material permeability, $tan\delta$ and $tan\varphi$ are the loss tangents of the material in electric and magnetic fields. $|E|$ and $|H|$ parameters in the equation represent the electric and magnetic field values that contribute to heating. The first part of the equation belongs to the influence of electric field and the second part of the equation refers to the influence of magnetic field.

EXPERIMENTAL PROCEDURE

a) Electrode Material Preparation:

All the electrode materials used in these experiments were prepared at the Battery Division of Oak Ridge National Laboratory (ORNL). $LiNi_{0.5}Mn_{0.3}Co_{0.2}$ (NMC532) cathodes and graphite (A12) anodes were coated via proto-type slot-die coater using both N-Methyl-2-pyrrolidone (NMP) and aqueous solvents. The NMC532 cathode consists of NMC532 (Toda America), carbon black (Denka), and binder(s) in the ratio of 90:5:5 by weight. The binders are 5130 Polyvinylidene Fluoride (PVDF) for NMP-based processing and Solex HPX-859 (Solvay Specialty Polymers) and Carboxymethyl Carbonate (CMC) in 4:1 weight ratio for aqueous processing. The A12 anodes are composed of 92 wt% A12 Graphite (ConocoPhillips), 2 wt% Super P Li (Timcal), and 6 wt% 9300 PVDF (Solvay Specialty Polymers) for the NMP-based processing. For the aqueous processed anodes, the 6 wt% 9300 PVDF binder was substituted by 4 wt% of Solex HPX-859 and 2 wt% CMC. The areal loadings were 14.6-16.6 mg/cm^2 for NMC532-NMP electrodes and 11.0-12.5 mg/cm^2 for aqueous based samples, respectively. They are 7.0-7.5 mg/cm^2 and 6.0-6.5 mg/cm^2 for the NMP-based and aqueous based A12 anodes.

b) Microwave Drying Process:

Microwave drying of battery electrode samples were carried out using a MW in-line hybrid system[17] shown in Figure 3a & 3b. This system has a wide temperature capability with a very high degree of uniformity, even at elevated temperatures. However, for battery electrode drying, the temperatures employed are usually below 200°C. In our case, drying of NMP– based

electrodes did not exceed 125°C and drying of aqueous based electrodes did not exceed 80°C. The temperatures in various zones of MW system were measured using multiple thermocouples beneath the samples. The detailed description of the technical features of this system can be found elsewhere[17]. The drying times were controlled by the speed of belt speed and in these experiments and varied anywhere from 25 min. to 105 min. After completion, the samples were weighed, and rapidly transferred into a nitrogen filled glove box, then doubly sealed to prevent

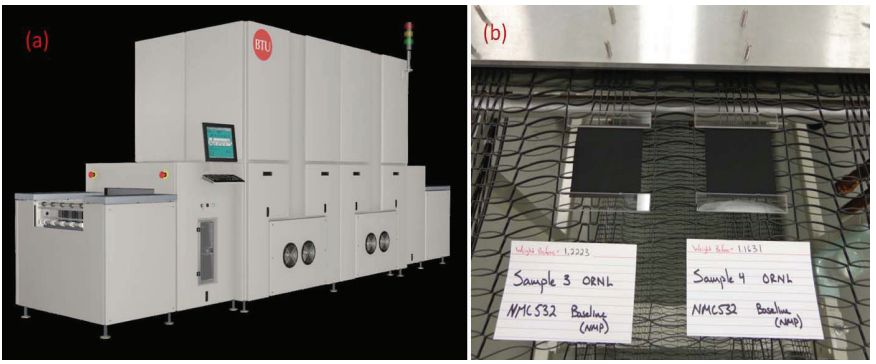

Figure 3: (a) BTU's inline MW system (b) Electrodes entering into the MW exposure zone

any moisture exposure. The performance studies were carried out at ORNL.

c) Electrode Performance Tests:

Figure 4: Coin cells prepared using microwave dried electrodes

Characterization of residual moisture content in microwave dried electrodes and electrode chemical performance evaluation were carried out at ORNL. The residual moisture was characterized by Karl-Fisher (K-F) titration. During measurement, the samples were heated to 200°C to ensure the release of moisture from the samples. Electrode chemical performance was evaluated in half coin cells (Figure 4) with lithium foil as the counter electrode. 1.2 M $LiPF_6$ in Ethylene Carbonate/Diethyl Carbonate (3/7 wt) was the electrolyte and Celgard 2325 was the

separator. The tests were performed by potentiostats (MPG-2, Biologic) inside an environmental chamber with constant temperature at 25°C. The voltage windows are 10mV-1.5V and 2.5-4.2V for the A12 anodes and NMC532 cathodes, respectively. The battery tests include two parts: 1) rate performance tests where the cells were cycled at various C-rates, from 0.05C to 10C with 5 cycles at each C-rate; and 2) cyclability where the cells were cycled at 0.2C/-0.2C and 1C/-2C for 50 cycles, respectively. The C-rate was defined as 1C=160 mA/g for NMC532 and 320 mA/g for A12, respectively.

RESULTS & DISCUSSION

a) Titration Results:

The titration results yielded moisture content in electrode samples processed using the hybrid microwave system. It usually takes about 15 minutes before the accumulate moisture content gets to equilibrium, reaching to a plateau. Figure 5 (a) & (b) shows the K-F titration

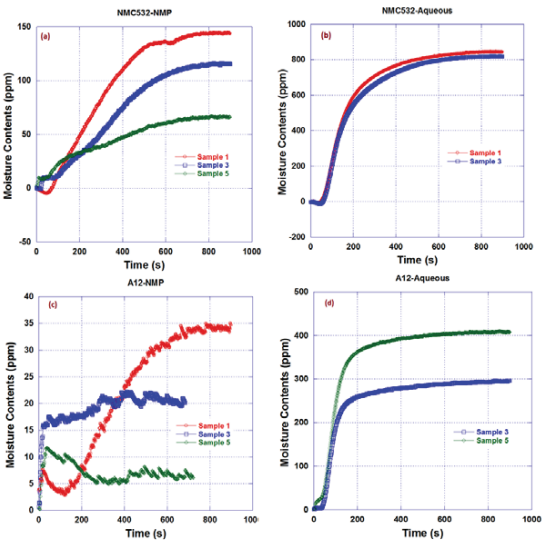

Figure 5: Moisture content in microwave dried (a) NMC532-NMP (b) NMC532-Aqueous (c) A12-NMP and (d) A12-Aqueous samples

curve for NMC532 cathodes. The starting point ideally should be zero but in some cases the observed slight negative value below 100s is due to the adjustment against a minor leak in the system. The measured moisture content in different samples is listed in Table 1.

Table 1: Microwave treatment conditions and residual moisture from titration

NMC532-NMP	Temperature (°C)	Exposure Time	Residual Moisture (ppm)
sample 1	125	25 min 46 secs	144
sample 3	125	51 min 32 secs	115
sample 5	125	1h 43 min 4 secs	66
NMC532-Aqueous			
sample 1	80	25 min 46 secs	842
sample 3	80	24 min 41 secs	818
A12-NMP			
sample 1	125	27 min	35
sample 3	125	53 min	20
sample 5	125	1h 39mins 4 secs	6
A12-Aqueous			
sample 3	80	25 min 46 secs	296
sample 5	80	24 min 41 secs	407

In NMC532-NMP cathodes (Figure 5(a)), for same temperature of treatment, the moisture content decreased from 144 ppm to 66 ppm with an increase in exposure duration from 25 min to 103 minutes. This trend is understandable as longer microwave exposure duration will aid better drying. For the NMC532-aqueous (Figure 5(b)) samples, the microwave treating conditions for sample 1 and 3 are almost identical and so are the results. The repeatability tests for these identically processed samples were required as these aqueous based samples were extremely hygroscopic in nature and their moisture levels could be very different from each other depending on the transfer durations from microwave furnace outlet to vacuum packaging unit. The moisture content of both the NMC532-aqueous samples was measured to be ~ 800 PPM. This reveals that identical phenomena were taking place in both samples under similar drying conditions. Similarly, samples referred both in Figure 5(b) and 5(d) are aqueous based samples and their process conditions were also almost identical. In order to make a fair comparison against conventional processing, a baseline sample was also prepared in a dry room environment. The moisture content in the NMC532-NMP samples dried at 100°C for 2 hours with dry hot air was about 87 ppm. Referring to Figure 5(a) for NMC532-NMP based samples, it can be seen

that the moisture content of all but sample 5 showed higher values. Also, referring to Figure 5(b), NMC532-aqueous samples showed higher moisture content than NMC532-NMP samples. This is ascribed to lower treatment temperature and a more hydrophilic binder in NMC532-aqueous compared to NMC532-NMP samples. Although, we haven't studied this in detail, we believe that higher treatment temperatures and/or longer treatment periods would help to reduce the moisture content in the NMC532-aqueous samples.

Similar titration studies were performed on A-12 anode samples that were dried using the microwave hybrid system. Figure 5c and 5d shows the K-F titration curves for A12 anodes and the corresponding moisture contents are also listed in Table 1. Similar to NMP based electrodes, a reduction in moisture content with increasing microwave exposure period for A12-NMP samples (Figure 5c) was observed. For the A12-NMP sample 3, the measurement was terminated accidentally after 4 minutes and was quickly resumed back. The testing time was also accordingly reset. This leads to much higher moisture content at the beginning than it normally would be. For A12-NMP sample 5, the moisture level was very low, 6 ppm, indicating the drying condition employed was very efficient in removing moisture from the samples. However, the moisture contents of the A12-aqueous samples were much higher compared to A12-NMP electrodes. The reason for this is attributed to lower treatment temperatures and the inclusion of hydrophilic binders. Unlike NMC532-aqueous samples, the A12-aqueous samples showed a considerable variation in moisture content despite identical microwave treatment conditions due to extreme hygroscopicity (see Figure 5b and 5d). The residual moisture content in these samples can further be improved by more efficient material handling, faster transfer time between treatment and packaging, and faster transfer time between the sample removal out of the package and start of measurement, etc,.

b) Electrode Performance Results:

Three categories namely sample 1, sample 3, and sample 5 represent 3 different process durations for same process temperature (see Table 1). Three cells in each category were tested to assure performance reliability of cells. In this study, almost all cells except one showed performances within a reasonable bandwidth and had been taken for consideration. The performance graph contains two portions namely 1) rate performance tests where the cells were cycled at various C-rates starting from 0.05C to 10C with 5 cycles at each C-rate for a total of 50 cycles; and 2) cyclic testing, where the

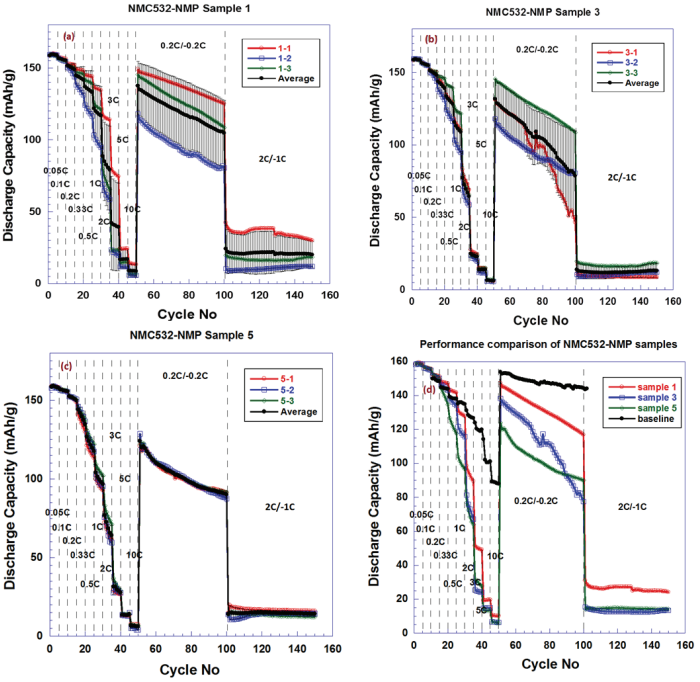

Figure 6: Cyclic performance study of NMC532-NMP samples (a) 1 (b) 3 (c) 5 and (d) their comparison with baseline electrode

cells were cycled at 0.2C/-0.2C and 1C/-2C, each for 50 cycles, respectively. The performance of NMC532–NMP cathodes 1, 3 and 5 is shown in Figure 6. Two samples in the same category, namely 1-1 and 1-3 showed a very consistent performance at lower C-rates. However, during the charging/discharging cycle at 0.2C/-0.2C from 50 to 100 cycles, the individual cells started showing deviations. At a rate of 1C/-2C cycling, the deviation became even higher. The performance of NMC532-NMP sample 3 is shown in Figure 6b. At lower C-rates, the samples showed very good consistency. However, during the charge/discharge cycle, the capacity values started showing larger deviations. A highly consistent behavior for all the 3 samples was observed for sample 5. This sample was microwave dried for 1hr and 45 minutes. The consistency was quite astounding throughout the entire cycling. The observed deviation in 0.2C/-0.2C in half coin cells is attributed to electrolyte consumption by lithium anode. As this chemical reaction occurs, the capacity starts fading, leading to deviations in charge capacities.

From Figure 6d it can be seen that the microwave dried NMC532-NMP samples exhibiting a comparative performance against NMC532-NMP baseline sample at lower C-rates. The faster capacity fading at higher C-rates in MW treated samples is attributed due to higher areal loading (14.6 – 16.6 mg/cm^2) of MW samples than that of baseline (12.5 mg/cm^2) sample. From the graph (Figure 6d), it can also be seen that the electrode performance became lower with longer MW treatment time and lower moisture content. This phenomenon is quite surprising. The question that needs to be understood is whether longer microwave exposure duration has any effect on the performance by influencing the stoichiometry.

A similar study was performed on NMP532-aqueous samples (see Figure 7). The chosen samples namely 1 and 3 had identical MW treatment conditions (Table 1). Despite varying moisture content, the performance reproducibility was excellent in both these samples. Up to 50 cycles, the average performance of these two samples was almost identical within acceptable cell variation. However, when cycled at 1C/-2C deviations started occurring, which was most likely due to the electrolyte consumption by lithium anodes. The electrode performance of NMC532-aqueous was compared to the NMC532-baseline and NMC532-aqueous baseline. The NMC532-aqueous baseline has the same electrode composition as the two NMC532-aqueous samples but was much drier with a residual moisture content of only 50 ppm. The NMC532-aqueous baseline samples also had lower areal loading, which resulted in higher performance at high C-rates. The areal loading of the two NMC532-aqueous samples is similar to that of NMC532-baseline. The NMC532-aqueous samples exhibited better performance than the NMC532-baseline when cycled below 1C but their high rate performance reversed, which could be either due to the much higher residual moisture and/or less uniform distribution of electrode components in the NMC532-aqueous samples.

Figure 8d shows the performance of A12-NMP samples and their comparison to the A12 baseline, which was processed using NMP-solvent and dried with dry air. Unlike previous samples, these samples showed an initial capacity decrease and then an increase within first 50 cycles. Deviation started occurring only after that. However, among themselves they showed an excellent consistency. The capacity decrease during the initial cycles regardless of C-rates could be an indication that it took some time for the electrolyte to completely wet the A12 anodes. The slow wetting behavior is an indication that only part of the electrode participated in the chemical process and the remaining part did not participate in the intercalation-deintercalation process. As cycles continued, the dry anode area became reduced and more A12 anode contributed to the

charge-discharge process thus resulting in a capacity increase. All cells from the three samples demonstrate excellent rate performance and they were comparable to the A12 baseline. The average performance of the three samples was also very similar except that the sample 1 showed more severe capacity degradation. Sample 3 exhibited the best capacity retention during the 50 cycles at 0.2C/-0.2C, but suffered dramatic capacity fade afterwards. It is still unclear if this is anyway related to the differences in residual moisture content among themselves. Referring to Figure 8d, all the 3 A12-NMP cells showed excellent rate performance when compared

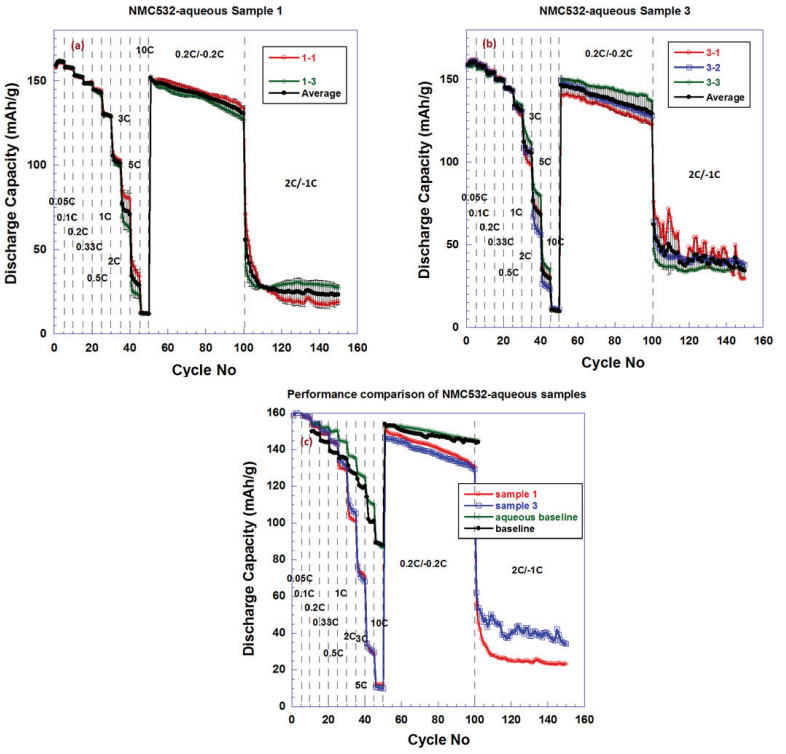

Figure 7: Cyclic performance study of NMC532-aqueous samples (a) 1 (b) 3 and (c) their comparison with baseline electrode

to A-12 baseline electrode. The average of sample 5 matched very well with the baseline electrode although the average of sample 1 shows a severe capacity degradation and average of sample 3

exhibits the best capacity retention initially during the 50 cycle at 0.2C/-0.2C, but suffered a dramatic capacity fade afterwards.

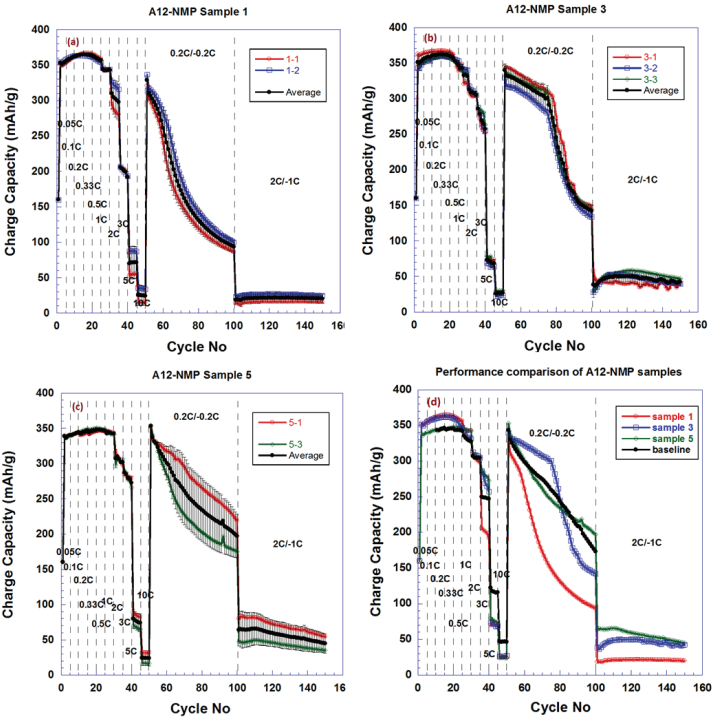

Figure 8: Cyclic performance study of A12-NMP samples (a) 1 (b) 3 (c) 5 and (d) their comparison with baseline electrode

The last series of coin cells that were tested for rate performance are A12–aqueous anodes (Figure 9). Similar to other samples, the A-12-aqueous baseline sample was prepared using dry air by conventional method. Out of 3 cells prepared using sample 3, two cells, namely 1 and 3 showed excellent rate performance. Sample 2 showed a very deteriorated performance. However, in the case of coin cells prepared using sample 5 (Figure 9c), all cells showed an acceptable rate performance and reproducibility. Referring to Figure 9d, the average of sample 3 and sample 5 compared very well with A12 baseline and A12 aqueous baseline curves. In fact, both these samples revealed a better cyclability than A-12 baseline cell. Although, these electrodes had much

higher moisture contents compared to A12-NMP samples, the effect of them, at least in short term cycles, was not noticed in the graph. Daniel and Wixom have noticed[18] that in $LiFePO_4$ cathodes, the electrodes having residual moisture content above 500 ppm showed much faster capacity degradation after 1000 cycles. We could not ascertain this in our work as the cycles employed here were much lower compared to the ones employed in their work.

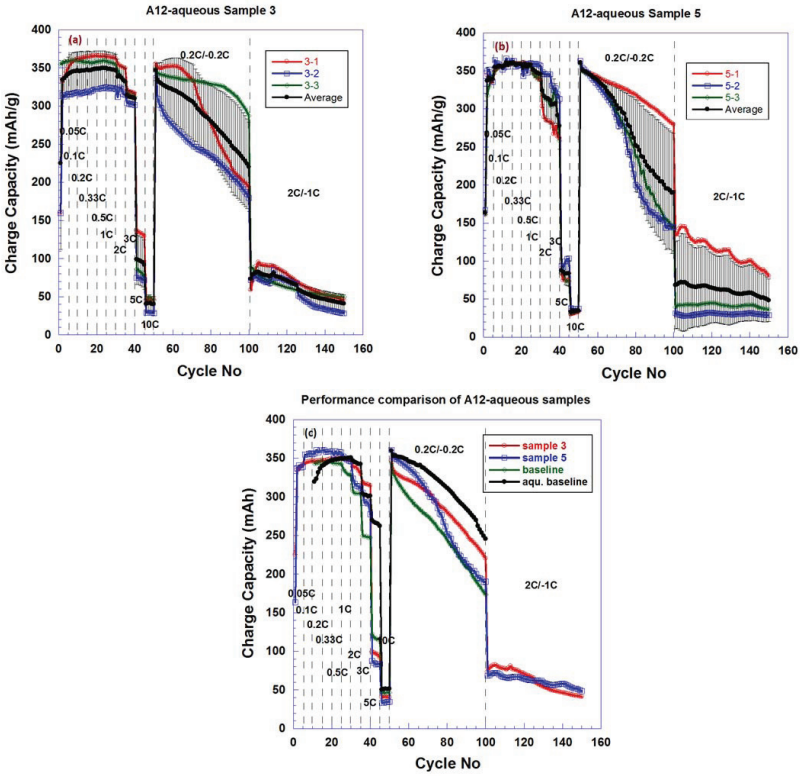

Figure 9: Cyclic performance study of A12-aqueous samples (a) 3 (5) and (c) their comparison with baseline electrode

(c) Microstructure:

It is known that in some applications, the incident microwave energy can potentially cause damages to the target material. Concentration of microwave energy on localized spots can superheat and melt those localized regions. In some other cases, selective constituents in the target material can cause serious arcing that can also alter the surface of the target material. For battery drying, hot spots could cause a very serious problem by greatly deteriorating its performance. By the use of hybrid technology as the one employed here, the electromagnetic energy intensity can be modulated and evenly distributed on a target surface so that possibility of any potential hot spot regions could be totally avoided. None of our microwave hybrid dried samples showed any sudden performance degradation, indicating presence of no abnormalities in the microstructure. In order to examine this, we have performed microstructure studies on NMC532-NMP and A12-NMP samples before and after microwave exposure. The

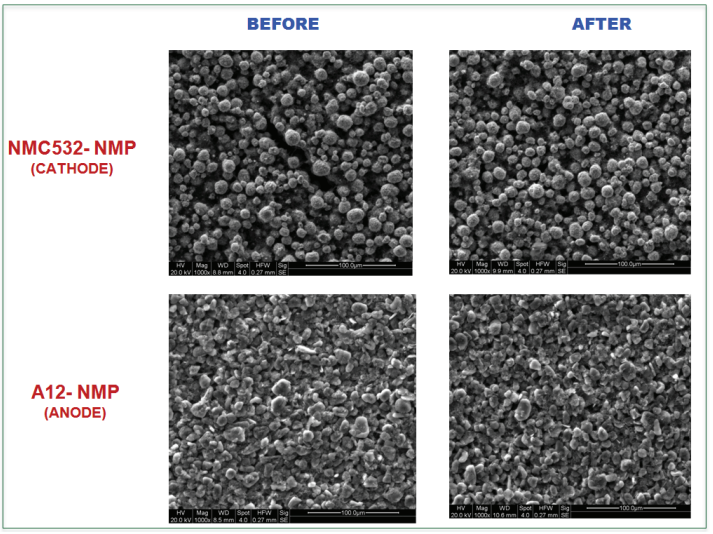

Figure 10: Microstructure of NMC532-NMP and A12-NMP electrodes before and after 103 minutes microwave exposure time

microstructures obtained at 1000x magnification are shown in Figure 10. From the figure, it can be seen that no observable changes were noticed before and after microwave exposure in either

samples. A number of analyses at various magnifications led to the same conclusion that the microwave hybrid drying did not cause any noticeable alterations to the electrode microstructure.

SUMMARY

$LiNi_{0.5}Mn_{0.3}Co_{0.2}$ (NMC532) cathode and graphite (A12) anode coatings were prepared at ORNL using a proto-type slot-die coater with both conventional N-Methyl-2-pyrrolidone (NMP)-based and aqueous solvents. All the electrodes were microwave dried using BTU's novel microwave hybrid system. The dried samples were quickly transferred into a glove box and carefully double packed in a nitrogen environment and shipped back to ORNL for performance testing. Titration results showed that the moisture content of NMP based samples was very low compared to aqueous based samples. This could possibly be due to three reasons; (i) a lower heat treatment temperature and/or (ii) shorter drying duration and/or (ii) hydrophilic binder content. All electrodes treated at various microwave conditions in ambient environment showed excellent rate performance and their performance is fairly comparable to the conventionally prepared baseline electrodes in a dry room. For shorter testing cycles, as the ones we have used here, the inherent moisture content did not show any adverse effects on rate performance. Microstructure studies revealed that there was no surface or microstructural damage to both NMP and aqueous based electrodes due to prolonged microwave exposure. The comparable performance of MW dried electrodes against baseline electrodes has proved that BTU's hybrid microwave technology can be very effective for battery drying with a potential cost savings that could bring down the overall battery manufacturing costs.

ACKNOWLEDGEMENTS

The authors would like to thank Jianlin Li Ph.D. and David L. Wood, III, Ph.D. of the Battery Manufacturing Research and Development facility of ORNL for their immense help with titration and cyclic performance measurements. They also helped in interpretation of the various results reported in this publication. The authors also acknowledge Claus Daniel, Ph.D., Deputy Director for the Sustainable Transportation Program of ORNL for his technical guidance and discussions at various stages of this study.

REFERENCES

[1]Daniel, C. (2008). Materials and Processing for Lithium-Ion batteries, *JOM*, 60(9), 43-48
[2]Nelson, P.A., Santini,D.J. and Barnes,J. (2009). Factors Determining the Manufacturing Costs of Lithium-ion Batteries for PHEVs, *EVS24 International Battery, Hybrid and Fuel Cell Electric Vehicle Symposium*, pp 1-12, Stavanger, Norway, May 13 -16.
[3]Wood III, D.L. et al, (2013). Advanced Materials Processing and Novel Characterization Methods for Low Cost, High Energy-Density Lithium-Ion Batteries, *Advanced Automotive Battery Conference* 2013; 01/2013.
[4]Wood III, D.L., Li, J., Daniel, C. (2015) Prospects of Reducing the Processing Cost of Lithium-Ion Batteries, *J. Power. Sources*, 275, 234-242.
[5]Sakti, A., Michalek, J. J., Fuchs, E. R. H., Whitacre, J. F. (2015) A Techno-Economical Analysis and Optimization of Lithium-Ion Batteries for Light Duty Passenger Vehicle Electrification, *J.Power.Sources*, 273, 966-980
[6]Axsen, J., Burke, A., Kurani, K. (2008) Batteries for Plug-in Hybrid Electric Vehicles (PHEVs): Goals and the State of Technology circa, UCD-ITS-RR-08-14
[7]Anderson, D. L. (2009) An Evaluation of Current and Future Costs for Lithium-Ion Batteries for Use in Electrified Vehicle Power Trains, Master's Thesis, Duke University.
[8] Liang, G. & MacNeil, D.D. (2011) State-of-the-Art Production Technology of Cathode and Anode Materials for Lithium-Ion Batteries in Lithium-Ion Batteries:Advanced Materials and Technologies edited by X.Yuan, H.Liu and J.Zhang pp 328 – 378.
[9]Bitsch, D., Dittmann, J., Schimitt, M., Scharfer, P., Schabel, W. and Willenbacher, N. (2014) A Novel Slurry Concept for the Fabrication of Lithium-Ion Battery Electrodes with Beneficial Properties, J. Power Sources 265, 81-90.
[10]Matthew, K. A., and Heywood, J. B. (2007) Electric Powertrains: Opportunities and Challenges in the U.S. Light-Duty Vehicle Fleet. Report from the Sloan Automotive Laboratory. Massachusetts Institute of Technology.
[11]Janney, M.A., Calhoun,C.L., and Kimrey, H. D. (1992) Microwave Sintering of Solid Oxide Fuel Cell Materials: I, Zirconia-8 mol% Yttria, *Journal of the American Ceramic Society*, 75 [2] 341-46.
[12]Clark, D. E., and Sutton, W. H. (1996) Microwave Processing of Materials, *Annual Review of Materials Science*, vol. 26, 299-331.
[13]De, A., Ahmad, I., Whitney, E. D., and Clark, D. E. (1991) Microwave Heating of Alumina at 2.45 GHz, *Ceramic Transactions*, 21 (1991)319-328.
[14]Schulz, R., Wicks, G., Folz, D., and Clark, D. E. (2011) Overview of Hybrid Microwave Technology, *Journal of the South Carolina Academcy of Science*,9[1].
[15]Ramesh, P. D., Brandon, D. G., and Schatchter, L. (1999) Use of Partially Oxidized SiC Particle Bed for Microwave Sintering of Low Loss Ceramics, *Mater. Sci. & Engg. A*, 266 (1) 211-220.
[16]Roy, R., Peelamedu, R. D., Grimes, C. A., Cheng, J., and Agrawal, D. (2002) Major Phase Transformations and Magnetic Property Changes Caused by Electromagnetic Fields at Microwave Frequencies, *Journal of Materials Research*, 17 (12), 3008-3011.
[17]Peelamedu, R. D., and Seccombe, D. A. (2014) "An Industrial Microwave (Hybrid) System for In-line Processing of High Temperature Ceramics", *Ceramic Engineering and Science Proceedings*, 35(6), 49-60.
[18]Daniel, C., and Wixom, M. (2012) "Transformational Electrode Drying Process", ORNL/TM-2012/617, DOI:10.2172/1060885

Ceramic Materials and Processing for Photonics and Energy

COPPER CLAD ULTRA-THIN FLEXIBLE CERAMIC SUBSTRATE FOR HIGH POWER ELECTRONICS

John A. Olenick, Kathleen Olenick
ENrG Incorporated
155 Rano Street, Suite 300, Buffalo, NY 14207
www.enrg-inc.com

John Andresakis
Oak-Mitsui Technologies, LLC
80 First Street, Hoosick Falls, NY 12090

ABSTRACT

ENrG has established itself as the global source for ultra thin flexible ceramics known as Thin E Strate®. Industry product trends require innovative high performance materials for SWaP - Smaller, lighter Weight and better Performance. There are no other self-supported ceramic membranes on the market this thin at 20 or 40 microns, with the ability to flex, take high temperatures and handle extreme transitions in temperature. These unique properties and advantages show promise as an enabling technology platform into a variety of markets and products, such as microbatteries, solar PV and microelectronics packaging. Ultimately these high volume markets want the new materials in larger sheets, like is now available for FR4, or in a roll-to-roll format. This paper will present work done in conjunction with Oak-Mitsui on double-sided copper cladding of the thin ceramic, with subsequent circuit definition and application testing. Material and application performance data will be presented as available across multiple market applications. The two companies' objective is to meet the growing market need for thermal management in electronics, including LEDs, resistive heater circuits, and power electronics.

INTRODUCTION

ENrG Incorporated (ENrG) is fast establishing itself as the global source for ultra thin flexible ceramics (see Figures 1 and 2) known as Thin E-Strate®. There is no other self-supporting ceramic membrane product on the market at 40 microns, with the ability to flex, take high temperatures and handle extreme transitions in temperature. These unique advantages show promise as an enabling technology platform in a variety of target markets including microbatteries, LEDs, solar PV, and microelectronics packaging. Industry product trends require innovative high performance materials for SWaP - smaller, lighter weight and better performance - which provides further market expansion opportunities for Thin E Strate®.

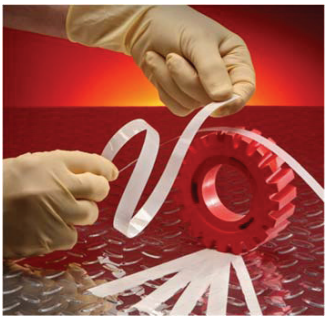

Figure 1 - 50 cm strip of Thin E-Strate®.

Consumer device builders however want the advantages of any new materials without a significant increase in price for these added benefits, and processing of a ceramic electronic substrate material from rolls is regarded as a path with high potential for cost savings. ENrG and Oak-Mitsui's Hoosick Falls, NY operations have teamed to provide a double-sided copper-clad 20 microns thick Thin E Strate®. Both companies will work together to commercialize the clad product into flexible electronics applications.

To further this product, ENrG is developing via cutting laser technology to permit more aggressive heat transfer, electrical connectivity between sides and the production of multiple layer components. Also in development is wire bonding to Thin E Strate®, along with the ability to diamond saw individual components. Work here demonstrated panelization of multiple customer test designs, and then etching and processing through a printed wiring board shop. Customers are now evaluating their test circuits and results will be presented as available.

THIN E STRATE® OVERVIEW

ENrG manufactures Thin E-Strate®, an ultra-thin flexible fully dense zirconia-based ceramic substrate. The flexibility of Thin E-Strate® is illustrated in Figure 2 where a "CD" size substrate, slit along the radius, is twisted back upon itself. Typically, ceramic materials are the last ones considered by high volume designers because they cost more than other common flexible metal or organic substrates.

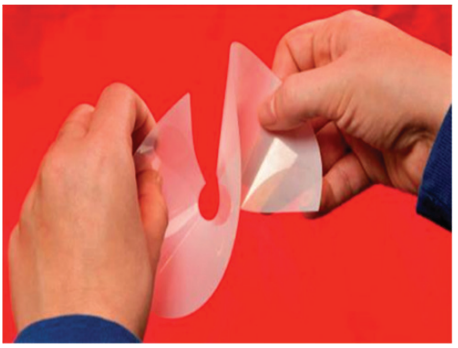

Figure 2 - Twisting of sintered 40µm thick Thin E-Strate®.

Past available thin ceramic versions were not strong or robust, and until now, not self-supporting and flexible. Driven by the market trends mentioned, either established or new high volume markets require a new set of high performance, high temperature capable materials. Desired properties are thinner, lighter and more robust to withstand extreme conditions either in operations, or during the processing of component manufacturing. This brings the designers back to looking for thin flexible ceramic substrates, but device builders want these new materials without significant increase in price for the desired benefits compared to the well established, but underperforming metal or organic flexible materials.

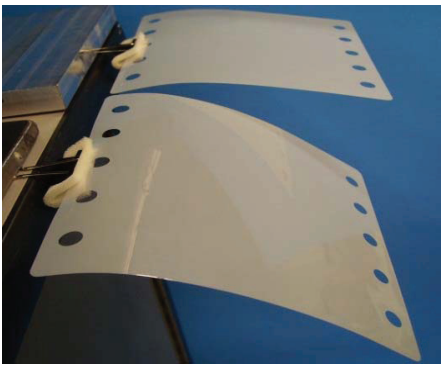

Figure 3 - 20 microns thick Thin E- Strate® in foreground, 40 microns thick in back.

Thin E-Strate® is an ultra-thin, dense, 3 mol% yttria-stabilized zirconia (3YSZ) substrate. It is available in either 20 or 40 microns thick. At 40 microns, it will easily bend to a "taco" shell type radius while the 20 microns version can wrap around a pencil. Substrates up to 120 x 150mm are available, including standard 100mm wafers with flats.

The origin of the Thin E-Strate® technology is based upon a Corning Incorporated invention[1,2], which was licensed by ENrG in 2008. Thin E-Strate® has unique physical properties that provide substantial advantages. ENrG has learned that these same properties and advantages, particularly higher strength, allow fabrication and use of much thinner, yet self-supporting, flexible membranes as shown in Figure 3. The ability to relieve stress through flexing provides remarkable thermal shock tolerance shown in Figure 4.

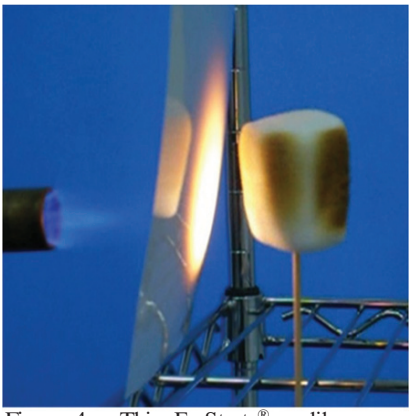

Figure 4 – Thin E- Strate® readily passes heat through plane.

In the field of electronics there has been a growing need for thermal management. As ICs have gotten smaller the heat they generate has gone up dramatically. Also, with the need to save energy in lighting, the push is on to move from incandescent to compact fluorescent and ultimately to LEDs, Figure 5 shows LEDS die attached and wire bonded onto Thin E-Strate®. Although less total energy is thrown off LEDs than incandescent, locally these devices can generate high temperatures that can be damaging to the substrate to which they are mounted, or cause over heating of the LEDs resulting in lower efficiency and shorter lifetimes. Other electronics that need to address thermal management are resistive heater circuits, solar CPV and power electronics; especially important as vehicles utilize more electronics for controls and propulsion.

Based on these and other applications, the need is growing for a new copper clad ceramic substrate that can handle these higher temperatures as well as be flexible to allow for unique uses and installations. Further a roll-to-roll (R2R) ceramic product would enable cladding the ceramic with high performance copper foils on roll-to-roll processing lines. A thin, lightweight, copper-coated, flexible electrical insulator with good heat extraction would be transformative to the microelectronics packaging market. Thus, this led to the genesis of the partnership with Oak-Mitsui to demonstrate double-sided copper-clad 40 and 20 microns thick Thin E-Strate® with ½ oz. copper for electronic applications.

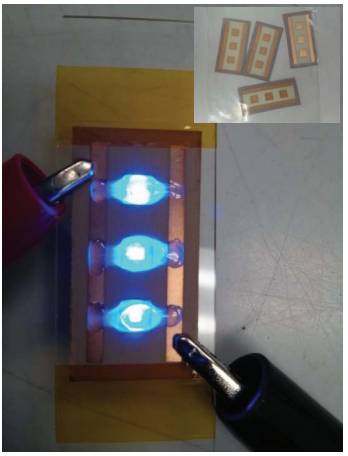

Figure 5 – LED circuit on 40 microns thick Thin E-Strate® substrate with etched copper laminate circuit. Inset photo shows etched copper circuit substrate.

COPPER-CLADDING

Oak-Mitsui is a leader in copper foil for electronics (the only electrodeposited copper foil manufacture in the Americas) as well as providing the leading edge embedded capacitor material called FaradFlex®. Their technical approach for developing a copper foil lamination process to ENrG's Thin E-Strate® began with modifying their current process (used with polyimide substrates) but maximized for the special properties of Thin E-Strate® material.

Oak-Mitsui first demonstrated this product with 40 microns thick Thin E Strate® shown in the inset photo of Figure 5. In addition to achieving pull strengths of 6 lbs./linear inch adhesion for the copper foil, which is a typical number for making printed circuit board material, they also did a "solder shock" test. This involved floating the substrate multiple times on molten solder for 10 seconds to simulate the surface mount assembly environment. The substrate passed this test as well. This clad laminate product

ultimately will permit a designer to use the inherent material properties of the dielectric support Thin E Strate®. Table 1 lists the collective material properties of Thin E-Strate®.

Table 1 – Thin E-Strate® Material Properties

Property	Measurement	Benefit
Physical:		
Material	>99.99% 3mol% YSZ	Common ceramic oxide, common electrolyte
Surface Finish	20-25 nm	Good for thin and thick film coatings
Thickness	20 or 40 microns	50% that of other available ceramic or glass materials
Density	6.04 g/cm^3	Near theoretical density, no premature passage of reactants
Crystal Structure	Tetragonal	Stable crystal structure over wide range of environments
Mechanical:		
Hardness	6.5 Mohs, 1600 Knoop (Kg/mm^2)	Will not wear, erode
Poisson Ratio	0.32	
Bend Strength	1.2 Gpa, measured on 2 cm strip, 20 microns	Gives flexibiliy, 3x other ceramics at these thicknesses
Flexural Strength	900 Mpa @RT	Permits rapid absorption of environment temperature shifts
Compressive Strength	2500 MPa @ RT	Can be put under high loads, once fully backside supported
Fracture Toughness	7.0 MPa x m$^{1/2}$	Great structural ceramic, robust in ultrathin format
Tensile Strength	248 MPa @RT	
Modulus of Elasticity	207 GPa	High for ceramic and glass materials, resists loads
Wear, Abrasion Resistance	Hard Material, near Diamond, TBD	High reliability in harsh environments
Thermal:		
Processing Temperature	Up to 1200°C	Gains in faster processing
Operating Temperature	Up to 1000°C	Higher temperature operations
Bulk Thermal Conductivity	2.7 W/mK	10x better than glass, 10% of alumina
Z-Axis Thermal Mass	Ultra-low	Phonons rapidly pass through, high heat disspation
Coefficient of Thermal Expansion	8.2ppm @ RT, 10.7 ppm @ 1000°C	Suitable for metal deposition, thin or thick films
Thermal Shock Resistance	>280-380 C/sec	Repeated rapid temperature transitions in applications
Specific Heat	0.10 cal/gC @RT	Good for rapid flexible heaters
Electrical:		
Dielectric Constant	26 @ 100kHz	Suitable for low speed electronics
Dielectric Breakdown	3200 VDC @ 40 microns, 2500 VDC @ 20 microns, 80 kV/mm @ 40 microns	High breakdown for ceramics, useful in power electronics
Resistivity	>10^{14}	Useful in power electronics
Optical:		
Light Dispersion	15% @ 40 microns	Substrate is translucent, enables backlighting, mixes and diffuses light from multi-color LEDs
IR Transparent	80% between 2-7 nm	Used in military systems
Chemical:		
Water Adsorption	0% @ RT	Near theoretical density, no moisture affects
Outgassing	0%, all temperatures	High purity, no long term degradation
Chemical Interactions	Not suitable with HF	Can be used in semiconductor processing, FDA approved for in body applications

COPPER-CLAD DESIGN SPECIFICATION WITH THIN E STRATE®

The two companies are currently targeting the following design specifications:

- 20 microns thick at >150 cm^2 and <300 cm^2
- <0.001 in/in of camber
- Edge curl <30 µm within 25 µm of the edge
- Laser cut edge or via without degradation of ceramic strength
- Total base dielectric thickness of 25-50 microns (20 microns of the ceramic)
- Copper thickness of 1-210 microns (1 to 5 microns is available by using Oak-Mitsui's Microthin® product which has a thin copper layer on a peelable copper carrier sheet)
- Operating temperatures of 2015 version, ≤ 130ºC and 2017 version, ≤ 200ºC (targeting 250ºC)
- Thermal Conductivity is TBD through testing (should be close to TC of copper/Thin E-Strate® with minimal impact of adhesive).

ENrG's product strategy is to shift away from cookie cutter type parts to higher volume applications requiring R2R ceramic format meeting the listed specifications. As a copper clad substrate, Thin E-Strate® can be sold for microbatteries, position sensors, electronics, and substrates for mounting LEDs for solid-state lighting. The technology for this product commercialization effort is high performance copper foil clad onto an ultra-thin ceramic for flexible electronic circuits in applications requiring rapid heat extraction, high voltage tolerance, high dielectric constant, lighter weight, thinner form factor and flexibility. Beyond this simplest product introduction a wide range of customization is possible in both the copper coating and the ceramic. Market and customer discovery will hone the product offerings, from thin copper for fine line circuits to thick copper and thinner ceramic for high power electronics with better heat dissipation.

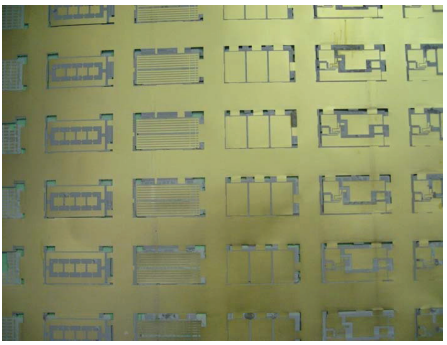

Figure 6 - Panelized customer test circuits.

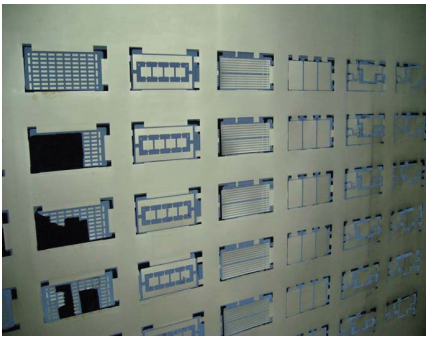

Figure 7 – Unsupported Thin E- Strate® damaged during high-pressure wash.

CUSTOMER EVALUATION AND TESTING

Seven customer designs from five sources - Hybridasol, Rensselaer Polytechnic Institute, North Carolina State University, and two unnamed companies - were panelized onto a two-sided copper-clad panel with Thin E Strate® dielectric substrates as shown in Figure 6. The ceramic substrates were about the size of glass slides. The panel assembly began with a large sheet of 20 microns thick polyimide, into which multiple rectangular areas had been cut out. These rectangular openings were slightly larger than the individual pieces of Thin E-Strate®. The ceramic pieces were aligned into the lower left corner of each opening, and then 1 ounce copper foil was clad to each side of the assembly, encasing the polyimide sheet and 20 microns thick ceramic substrates. By design, each unique circuit was held to the main panel by small copper ribbons overlapping on all four sides of the ceramic. The plan was for the ribbons to hold the finished circuits in place after printed circuit board (PCB) processing was complete.

The panels were imaged, etched and plated through Sanmina-SCI's, San Jose, CA printed circuit board line. Afterwards each individual circuit was removed from the panel by cutting the copper ribbons on the edges of the circuits. The learning from this first trial:

- The dielectric floated in the openings cut into the polyimide during the copper lamination process and many of the parts lost registration. This affected circuit placement and some of the copper ribbons did not connect to the ceramic edges.
- The panels went through a standard PCB line. Circuits with less copper support, or where the ribbons did not connect with the ceramic, were damaged during the high-pressure wash jets. Ceramic pieces broke off some parts, as seen in Figure 7. In the future, the jets can be adjusted down.

- The resin used to bond the copper foil to the ceramic remained behind on the surface of the substrates as we neglected to request a post processing plasma clean of the excess adhesive. It can be seen peeling off in some of the photos of Figures 6 – 10.

The panels were returned to ENrG and individual test circuits were singulated and supplied to the individual customers. While all are still evaluating their particular designs, one herein referred to as C1, has returned the following results.

CUSTOMER (C1) ELECTRICAL EVALUATION

Figure 8 shows all the samples taped down to a ceramic carrier. Figure 9 is a close-up of one of the samples. Ignoring a few holes in the ceramic, the sample looks good.

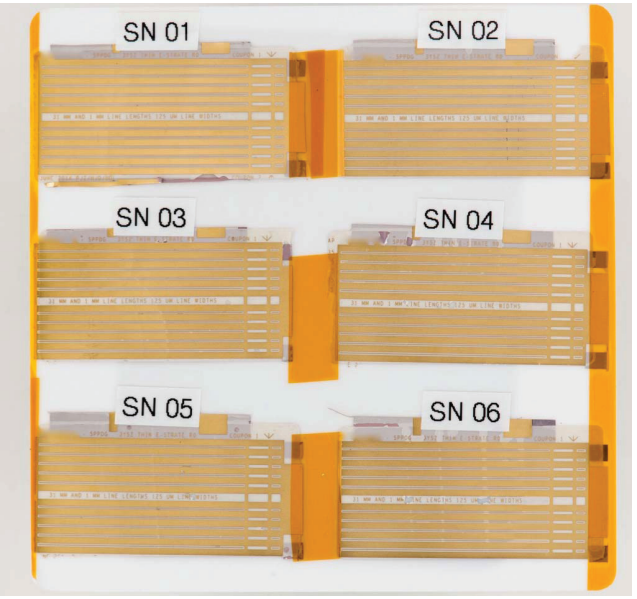

Figure 8 – C1 test evaluation circuits.

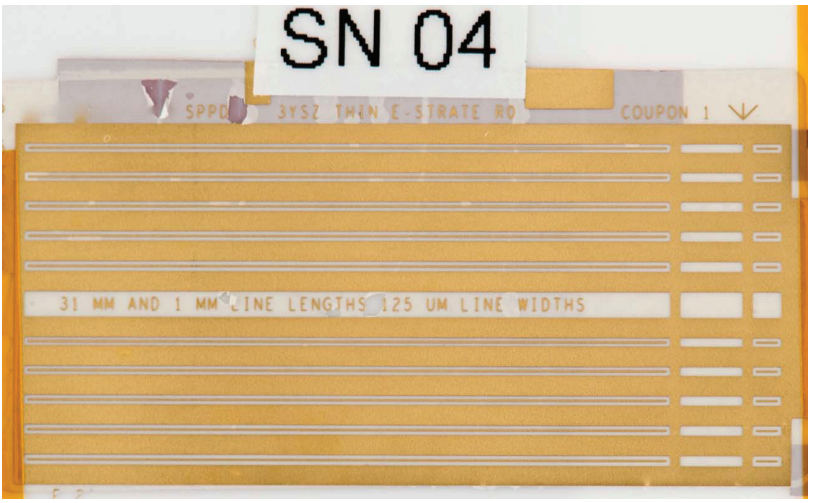

Figure 9 - C1 test circuit.

Visually, these first samples were clean, had good metal, and well defined ceramic. With an eye toward characterizing electrical performance, C1 measured three samples in three different ways, where the first two measurements lead into the third. The measurements included DC resistance, Time-domain Reflectometry (TDR), and Frequency-domain vector network analysis (VNA; often called S-parameters). The measured DC resistance of the traces averaged 256 mohm, which is 15% higher than that of bulk copper for traces of the same geometries and falls within the range C1 commonly sees on other packaging technologies. Figure 10 shows a view of the data set.

Keithley 580 Micro-Ohmmeter					Line Measurements taken in mm				
4 point resistance measurements					Measured at bottom				
SN	Line	Gap	Resistance		Gap upper	Gap lower	Line Width btm	Line Width top	Z Height
5	31 mm top	135	0.2416		0.164	0.162	0.096	0.070	0.030
5	31 mm top	145	0.2560		0.176	0.176	0.094	0.068	0.029
5	31 mm top	155	0.2580		0.186	0.187	0.091	0.068	0.028
5	31 mm top	165	0.2604		0.199	0.196	0.091	0.068	0.027
5	31 mm top	175	0.2506		0.208	0.208	0.093	0.071	0.033
5	31 mm btm	135	0.2617		0.167	0.168	0.090	0.067	0.028
5	31 mm btm	145	0.2512		0.180	0.178	0.091	0.070	0.028
5	31 mm btm	155	0.2637		0.190	0.190	0.089	0.068	0.029
5	31 mm btm	165	0.2522		0.197	0.196	0.092	0.068	0.027
5	31 mm btm	175	0.2664		0.214	0.211	0.087	0.065	0.034
			Resistance				Width, Btm	Width, Top	Height
		Average	0.2562	ohm		Average:	0.0914	0.0683	0.0293
		Std Dev	0.007431	ohm		Area:	0.0023396	mm^2	
		Std Dev	3%	%		Area:	2.34E-09	m^2	
				Effective Resistivity of Traces		1.93E-08	ohm-m		
				Theoretical Resistivity of Bulk Copper		1.68E-08	ohm-m		
					Delta	15%	% Difference From Theory		

Figure 10 - Resistance measurement data set.

TDR measurements indicate how well the signal traces match the target characteristic impedance. The measured impedance in each case was greater than the desired 50 ohms. Looking at the resistance table, the physical gap between the trace and the surrounding ground planes was 30 to 40 µm greater than it was designed. With impedance being nonlinearly related to gap distance, C1 believes the variation from the target 50 ohms was due to the larger gap distance, which was and is often a result of over-etching of the circuit traces.

In addition to being off from the target impedance, the effect of the gap distance was much lower than expected, shown in Figure 11, which plots the TDR response for the 135 µm structure and the 175 µm structure, where this dimension indicates the distance between the trace and the surrounding ground plane. The performance difference between these two gap sizes was much less than expected. Because the gap was notably larger than designed, it makes sense that the designed-variation in gap distance reduced the impact on impedance.

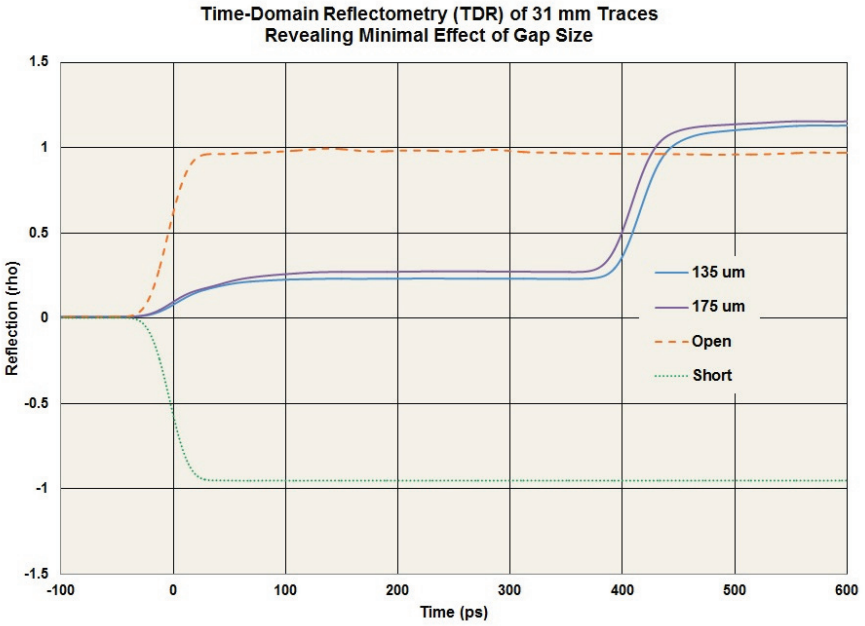

Figure 11 - TDR measurements.

The frequency domain measurements provide the most insight – and are often the most challenging to interpret. "S11" – reflection coefficient – is a measure of the characteristic impedance (similar to TDR, but in the frequency domain). Ideally, S11 would be negative-infinity (as measured in decibels, dB). When S11 is higher than -14 dB, the amount of signal being reflected at the trace's input is large enough to noticeably reduce how much signal gets into the trace, which shows up as increased effective loss.

"S21" – signal gain – is a measure of how much signal is attenuated within the trace. Ideally, S21 is 0 dB, meaning no signal is attenuated (absorbed or radiated) in the trace. As reference, C1 often looks for S21 to be above -6 dB for low-frequency interfaces, such as used for memories, processors, etc., and C1 looks for S21 to be above -15 dB for high-frequency interfaces, such as used in SerDes, optics, etc. (Oddly, faster interfaces can often tolerate greater loss due to the use of signal-equalization techniques.) The data is shown in Figures 12 and 13.

In Figures 12 and 13, the relatively high impedance shows up in two forms. In S11, the tops of the curves (peaks) reach around -7 dB to -15 dB, which supports the TDR data that the trace impedance was far from the target of 50 ohms. Looking at S21, the dips corresponds to the peaks in S11, which was due to a large fraction of the signal being reflected at the trace's input and not getting into the trace itself.

The VNA measurements also reveal limited effect of the traces' gap geometries, which confirmed the TDR data. That is, S21 for the 135 µm and the 175 µm trace are relatively similar to one another. When the VNA data is better behaved (i.e., S11 is lower than -20 dB), C1 can often extract a variety of other useful characteristics, such as how much of the attenuation was within the copper (related to resistivity) and the dielectric (loss tangent), dielectric constant,

etc. Unfortunately, the apparent over-etching of the traces increased the characteristic impedance of the traces to the point where such extractions are impractical.

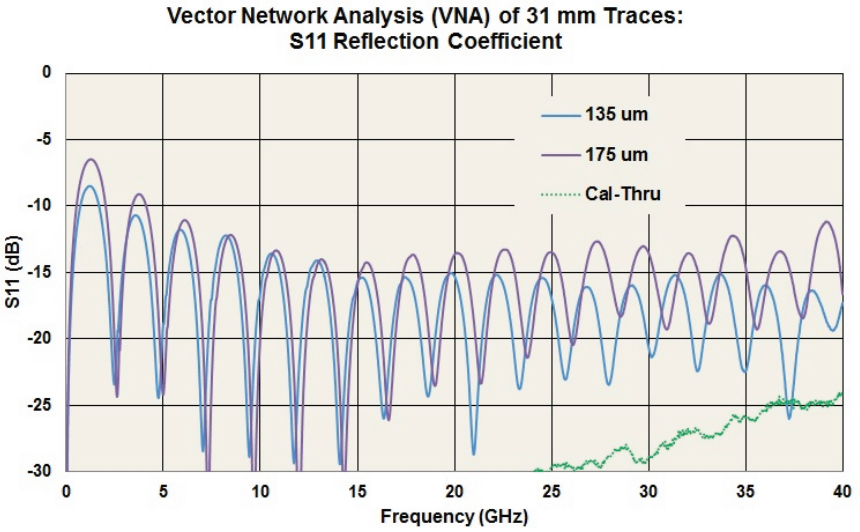

Figure 12 - S11 test measurements.

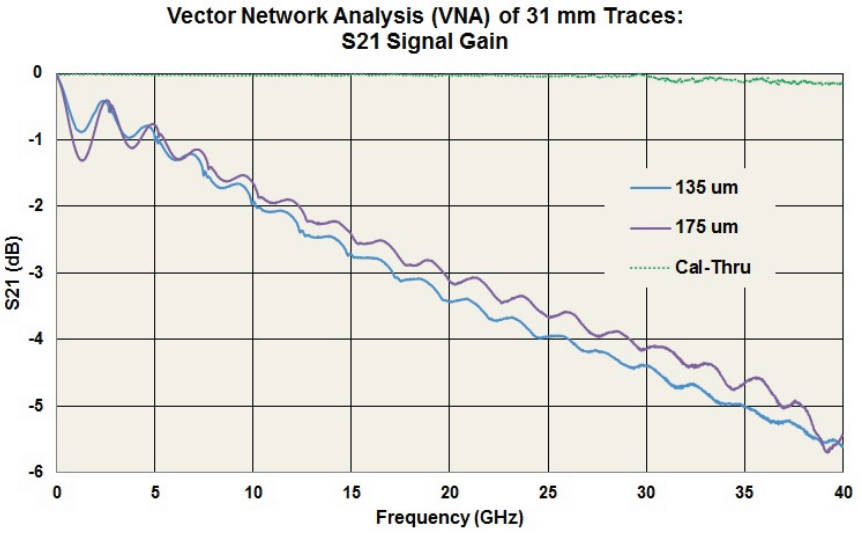

Figure 13 - S21 test measurements.

Ignoring the impedance, the attenuation shown in S21 measurements was minimal. The losses up to 40 GHz are less than 6 dB, which was terrific. The traces are relatively short at 31 mm, but the losses can generally be accommodated in digital systems.

C1's conclusion: overall, the electrical performance of the raw technology was well suited for multiple applications. The metal resistivity was close to that of bulk copper, and the attenuation could be readily accommodated in most digital systems – up to 40 Gb/s data rates – assuming traces are restricted to short lengths. Unfortunately, the excessive gap size pushed the characteristic impedance outside useful ranges, which degraded some measurements and hampered further analysis. Roughly speaking, the raw technology performed quite well relative to other packaging technologies that used similar geometries – assuming the etching process can eventually closer match that of design.

C1 further noted that the structures did not contain vias, which are essential features for most digital systems. Vias often degrade electrical performance, so their absence in these structures artificially improved the measurements relative to what would be expected in a real system.

FUTURE PLANS

Further analyses by the various customers are now planned. A R2R ceramic product would enable cladding the ceramic with high performance copper foils on roll-to-roll processing lines further penetrating the flexible electronics circuit market. The first copper cladding trials on individual sheets have shown excellent bonding to both sides of the ceramic, with pull strengths in the range of FR4 printed circuit boards and polyimide flexes. A thin, lightweight, copper-coated, flexible electrical insulator with good heat extraction would be transformative to the microelectronics packaging market.

ACKNOWLEDGEMENTS

The authors would like to gratefully acknowledge funding through New York State Energy Research and Development Authority (NYSERDA). The authors also acknowledge Corning Incorporated for the technology license. The authors acknowledge the support of Sanmina-SCI Corporation, Hybridasol, RPI, and NCSU.

REFERENCES

[1] M. E. Badding, J. E. Cortright, T. D. Ketcham, D. M. Lineman, and D. J. St. Julien, "Solid Oxide Fuel Cell and Packet Design", US Patent Application Publication No. US2003/0096147

[2] M. E. Badding, W. J. Bouton, J. L. Brown, L. Kester, S. Pollard, C. W. Tanner and P. D. Tepesch, "Ultra-low Mass Planar SOFC Design", Presented at the SOFC X11 Conference in Montreal, Canada, 2011.

ROLL-TO-ROLL ULTRATHIN FLEXIBLE CERAMIC FOR COST EFFECTIVE COATING

John A. Olenick, Viswanathan Venkateswaran, and Kathleen Olenick
ENrG Incorporated
155 Rano Street, Suite 300, Buffalo, NY 14207
www.enrg-inc.com

ABSTRACT

This paper presents ENrG's 2015 introduction of its goal to produce an in-line, coatable format of its Thin E-Strate® product. The 20 microns thick product, targeted between 100-300 meters long, with initial widths up to 5 centimeters, is being developed for customers capable of coating in roll-to-roll (R2R) form.

Unlike plastic films in which temperature and humidity affect roll-to-roll handling and alignment, Thin E-Strate® is stable, inert and is translucent for two-sided coating registration. This flexible ceramic can handle higher temperature processing, does not absorb moisture and is corrosion resistant. Thin E Strate®, a flexible zirconia based ceramic membrane, was originally introduced in 2010 at 40 microns thick. Even though so thin, the membrane is gas-tight, fully dense, strong, thermal shock tolerant and chemically inert.

Inherent properties of the membrane are compatible with many applications including wearable electronics, mechanical sensors, medical electronics, microbatteries, solar photovoltaic, power electronics, solid-state lighting, transparent infrared windows, fuel cells, and superconductors. These uses tap into additional membrane properties via application-specific coatings. Many of these market opportunities require the thin ceramic to be supplied in a R2R form for more economical processing.

INTRODUCTION

In 2010, ENrG Incorporated commercialized 40 microns thick, flexible zirconia-based ceramic membranes as shown in Figure 1. Exceptionally thin for a ceramic, these membranes are gas-tight, fully dense, strong, thermal shock tolerant and chemically inert. ENrG introduced the product with the registered trademark name of Thin E-Strate®. This technology is based on thin, sintered partially stabilized zirconia ceramic sheets developed by Corning Incorporated and used in its solid oxide fuel cell (SOFC) inventions[1,2]. The 3mole% yttria-stabilized zirconia (3YSZ), at ≤ 40 μm thick, has sufficient strength for processing and handling. The ability to relieve stress through flexing provides remarkable thermal shock tolerance, as shown in Figure 2.

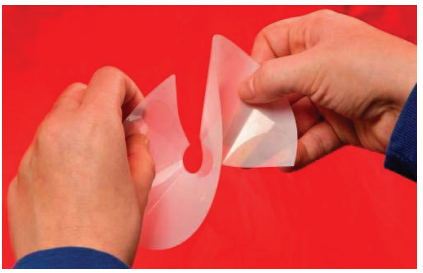

Figure 1 – Flexibility of ENrG's Thin E-Strate® 40 microns thick fired ceramic.

Yttria-Stabilized Zirconia (YSZ) is historically used in a wide variety of applications including the electrolyte in solid oxide fuel cells and solid oxide electrolyzer cells (SOECs), dental crowns, the substrate in oxygen sensors, thermal barrier coatings for metal substrates in harsh environments, and structural ceramics such as hip replacements. SOFCs, SOECs and oxygen sensors use the ionic property of partially stabilized zirconia at elevated temperatures, and these applications were ENrG Inc.'s first markets. Figure 3 shows a cross-section of the ceramic, coated with electrodes and used as the electrolyte in an electrolyte-supported SOFC[3].

Three years after introduction, it is apparent inherent properties of the membrane other than ionic conductivity are compatible with many other market applications in harsh environments. Table 1 lists the collective material properties of Thin E-Strate®. Besides thinness, flexibility and strength, these alternative applications tap into properties of translucency, low thermal mass, chemical resistance, infrared optical transmission, ability to bend around very tight radii, or enhanced capabilities with applied coatings. Uses include sensors, medical electronics, microbatteries, solar photovoltaic (PV), power electronics, LED substrates, transparent infrared windows, flexible electronics and superconductors.

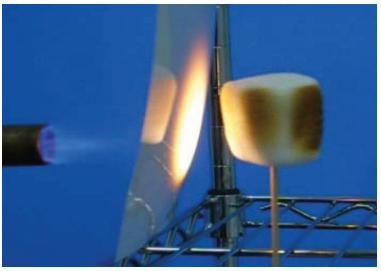

Figure 2 – Charring of a marshmallow from a blowtorch applied to the opposite side of the 40 microns thick Thin E-Strate®.

Thin E-Strate® has a number of qualities that make it attractive as a substrate for fabrication of solar thin film cells[4] and solid-state devices. These qualities include the ceramic's smooth surface, dielectric property, lack of impurities, high temperature capabilities, and its strength and flexibility for roll-to-roll handling. In addition, the future ability to scale to a roll-to-roll format offer a substrate option over stainless steel foils, thin silicon wafers, glass sheets and thick ceramic sheets. Additional high volume applications require a R2R capable substrate, with the attributes of ENrG's Thin E-Strate®, for economical deposition of active and passive coatings.

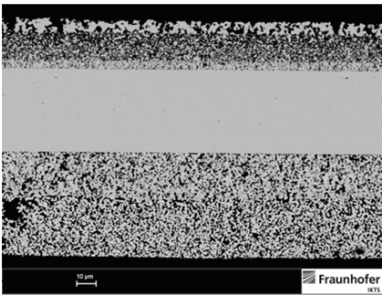

Figure 3 - Thin E-Strate® is the dense electrolyte in a cross-section of a SOFC.

(Courtesy of Fraunhofer IKTS).

Thin E-Strate® is fully dense as shown in Figure 3 and moisture impermeable. Overall device processing costs can be reduced with the elimination of barrier layers, since Thin E-Strate® is gas impermeable and a dielectric. Other integration opportunities may be possible. The ceramic is a wear and corrosion resistant material; therefore one side of the substrate could provide a seal or external surface for a final product.

The use of a single material and technology in R2R format, across multiple market sectors, can significantly increase volumes for a previously unavailable flexible ceramic.

WHY ROLL-TO-ROLL PROCESSING?

Today Thin E-Strate® is available in either 20 or 40 microns thick sheets, with a possible maximum substrate size up to 120mm x 150mm. This is not a technology limitation, but is a result of the equipment constraints in ENrG's current factory. Many shapes and sizes are available including a standard 100 mm diameter "wafer" with flat. At 40 um thick, Thin E-Strate® can safely meet a bending diameter of 0.5", demonstrated in Figure 4 as the "taco shell" bend, and the 20 um thick ceramic can obtain a bending diameter of 0.375", about the breadth of a pencil.

Table 1 - Thin E-Strate® Material Properties

Property	Measurement	Benefit
Physical:		
Material	>99.99% 3mol% YSZ	Common ceramic oxide, common electrolyte
Surface Finish	20-25 nm	Good for thin and thick film coatings
Thickness	20 or 40 microns	50% that of other available ceramic or glass materials
Density	6.04 g/cm^3	Near theoretical density, no premature passage of reactants
Crystal Structure	Tetragonal	Stable crystal structure over wide range of environments
Mechanical:		
Hardness	6.5 Mohs, 1600 Knoop (Kg/mm^2)	Will not wear, erode
Poisson Ratio	0.32	
Bend Strength	1.2 Gpa, measured on 2 cm strip, 20 microns	Gives flexibiliy, 3x other ceramics at these thicknesses
Flexural Strength	900 Mpa @RT	Permits rapid absorption of environment temperature shifts
Compressive Strength	2500 MPa @ RT	Can be put under high loads, once fully backside supported
Fracture Toughness	7.0 MPa x m$^{1/2}$	Great structural ceramic, robust in ultrathin format
Tensile Strength	248 MPa @RT	
Modulus of Elasticity	207 GPa	High for ceramic and glass materials, resists loads
Wear, Abrasion Resistance	Hard Material, near Diamond, TBD	High reliability in harsh environments
Thermal:		
Processing Temperature	Up to 1200°C	Gains in faster processing
Operating Temperature	Up to 1000°C	Higher temperature operations
Bulk Thermal Conductivity	2.7 W/mK	10x better than glass, 10% of alumina
Z-Axis Thermal Mass	Ultra-low	Phonons rapidly pass through, high heat disspation
Coefficient of Thermal Expansion	8.2ppm @ RT, 10.7 ppm @ 1000°C	Suitable for metal deposition, thin or thick films
Thermal Shock Resistance	>280-380 C/sec	Repeated rapid temperature transitions in applications
Specific Heat	0.10 cal/gC @RT	Good for rapid flexible heaters
Electrical:		
Dielectric Constant	26 @ 100kHz	Suitable for low speed electronics
Dielectric Breakdown	3200 VDC @ 40 microns, 2500 VDC @ 20 microns, 80 kV/mm @ 40 microns	High breakdown for ceramics, useful in power electronics
Resistivity	>10^{14}	Useful in power electronics
Optical:		
Light Dispersion	15% @ 40 microns	Substrate is translucent, enables backlighting, mixes and diffuses light from multi-color LEDs
IR Transparent	80% between 2-7 nm	Used in military systems
Chemical:		
Water Adsorption	0% @ RT	Near theoretical density, no moisture affects
Outgassing	0%, all temperatures	High purity, no long term degradation
Chemical Interactions	Not suitable with HF	Can be used in semiconductor processing, FDA approved for in body applications

ENrG's current manufacturing is a batch process (i.e., individual sheets). It involves significant handling of the unsintered ceramic, severely affecting yield and ultimately increasing the cost of manufacturing. Further, this batch process is energy intensive and lengthy, with the ceramic in contact with refractory kiln furniture during the entire stationary firing cycle. This increases the chances of sticking of the ceramic to the support furniture as it shrinks, or of debris adhering onto the surface of the membrane.

The development and cross-market opportunities have enabled cost reductions of these thin zirconia membranes, even with the present batch fabrication process. However, imagine a thin ceramic substrate with the aforementioned harsh environment tolerant properties, available in rolls up to 300 meters long, for R2R handling and coating. The translucent nature of the ceramic would aid in alignment of double-sided printing. The ceramic, unlike polymer substrates, will not stretch or deform under humidity, the processing heat of applying coatings or during R2R movement.

ADDRESSING THE CHALLENGE

Today a roll of flexible ceramic is not available on the market, but such a product would revolutionize ceramic component delivery to many large market applications. Producing a R2R

polycrystalline-sintered ceramic is not trivial. During sintering, the ceramic is shrinking, is a challenge to keep flat and has weak points during the cycle, presenting handling challenges.

Feasibility was demonstrated at Corning Incorporated in their initial development of thin membranes, and ENrG further verified viability at the laboratory scale in 2013 shown in Figure 4. With in-house available equipment, ENrG was able to process lengths as long as 0.5 meters viewed in Figure 5. These preliminary experiments clearly demonstrated that the ceramic could be continuously processed.

Since the ceramic is very thin and light, an overwhelming fraction of the energy spent is used for heating the furnace. ENrG has done a systematic analysis of energy consumption in the batch furnace versus a continuous line. Based on the analysis it is possible to obtain over 80% energy savings. In addition there are other benefits such as 30x productivity increase over the same energy signature, significant capital cost savings, and reduction in amount and replacement of kiln furniture.

Figure 4 - Thin E-Strate® handled by rollers.

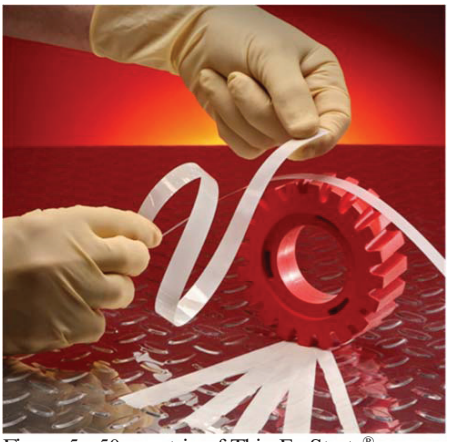

Figure 5 - 50 cm strip of Thin E- Strate®.

A flexible continuous "ribbon" of Thin E-Strate® would allow feeds into several commercial direct write / aerosol jetting systems for products requiring unique circuit definition, such as RFIDs or other serialized / labels for harsh environments. A R2R ceramic product would enable cladding the ceramic with high performance copper foils on roll-to-roll processing lines further penetrating the flexible electronics circuit market.

By the end of 2015, ENrG will introduce an in-line, coatable format of its Thin E-Strate® product at 20 microns thick, targeted at 10 meters long, with initial widths up to 5 centimeters. This is being developed for customers capable of coating in R2R form. Investment and development in 2016 and beyond will scale the format to 100-300 meters, and pursue wider formats.

SUMMARY

Thin E-Strate® has a number of qualities that make it attractive for high volume applications requiring a R2R capable substrate for economical deposition of active and passive coatings. The future ability to scale to a roll-to-roll format offers a substrate option over stainless steel foils, thin silicon wafers, glass sheets and thick ceramic sheets.

Thin E-Strate® has a very strong value proposition in terms of offering a novel flexible ceramic membrane, with applications across multiple markets, thereby significantly reducing costs. In addition, Thin E-Strate® is compatible with many existing coating processes. Offering this unique ceramic in a R2R format will be a disruptive technology and a game-changer for many applications in wearable electronics, defense and aerospace, consumer products, embedded

sensors, medical electronics and extended uses beyond the limits of polyimide flexible electronics.

ACKNOWLEDGEMENTS

The authors would like to gratefully acknowledge funding through New York State Energy Research and Development Authority (NYSERDA). The authors also acknowledge Corning Incorporated for the technology license.

REFERENCES

[1] Badding, M. E., Brown, J. L., Ketcham, T. D., St. Julien, D. J. and Wusirika, R. R., "High Performance Solid Electrolyte Fuel Cells", US Patent #6,623,881.

[2] M. E. Badding, W. J. Bouton, J. L. Brown, L. Kester, S. Pollard, C. W. Tanner and P. D. Tepesch, "Ultra-low Mass Planar SOFC Design", Presented at the SOFC X11 Conference in Montreal, Canada, 2011.

[3]Olenick, J., Kuznesoff, M., Trofenko, N., Olenick, K. and Michaelis, A., "Electrolyte Supported Cells Based on an Ultrathin 3 YSZ substrate", Paper presented at the 10th CMCEE Conference in Dresden, Germany, May 2012

[4]Fobare, D., Haldar, P., Efstathiadis, H., Metacarpa, D., Wax, J., Olenick, J., Olenick, K. and Venkateswaran, V., "Novel Application of Yttria Stabilized Zirconia as a Substrate for Thin Film CIGS Solar Cell", Poster presented at the 40th IEEE Photovoltaic Specialist Conference (PVSC) in Denver, CO, US, June 2014

NANOMATERIALS FOR ENERGY CONVERSION – THE SYNTHESIS OF HIGHLY CRYSTALLINE YTTERBIUM(III) FLUORIDE NANOPARTICLES FROM IONIC LIQUIDS

Chantal Lorbeer[1] and Anja-Verena Mudring[2,3]*

[1] Massachusetts Institute of Technology, Department of Chemistry, Cambridge, MA 02139; USA
2 Department of Materials Science and Engineering, Iowa State University and Critical Materials Institute, Ames Laboratory (DOE), Ames, IA 50011, USA. E-mail: mudring@iastate.edu.
[3] Critical Materials Institute, Ames Laboratory (DOE), Ames, IA 50011, USA. E-mail: mudring@ameslab.gov

ABSTRACT
Small, uniform ytterbium(III)fluoride nanoparticles could be obtained by conversion of ytterbium acetate hydrate with reactive tetrafluoroborate ionic liquids. In the reaction the anion of the ionic liquid serves as a mild fluoride source. The influence of the cation of the tetrafluoroborate ionic liquid (1-butyl-3-methylimidazolium vs. trisbutyltetradecylphosphonium) as well as the heat providing mechanism (classical heat transfer and dielectric heating) were investigated. In all cases small, highly crystalline nanoparticles could be obtained which are promising host materials for optical applications.

INTRODUCTION
New synthetic strategies towards a known material can acutally extend the range of applications of a given, well-known material. In this regard, the manufacturing of materials on various lengthscales, especially on the nanoscale, in defined morphologies as regularly shaped, well-crystallized particles, rods and plates has become more and more imperative with the increasing significance of nanotechnology. Increasing societal welfare seems to be intimately linked with a growing demand for energy and in consequence, the smart and responsible management of energy has become a key factor to guarantee prosperity. Currently around twenty percent of the total electrical energy consumption in the U.S. are used for lighting purposes [1], and there is a strong quest for more energy efficient lighting [2]. State-of-the-art as well emerging technologies rely for the major share on luminescent materials [3]. A key factor in the design of energy-efficient lighting devices is the quality of light conversion. Energy losses through non-radiative relaxations, which can arise, amongst others, from defects such as impurities as well as structural disorder need to be minimized to achieve higher quantum yields. However, the synthesis of a high-purity and well-crystallized material is especially demanding for nanomaterials. Yet the demand for luminescent nanomaterials is large – not only for lighting purposes but also for a number of other application such as (bio-)imaging where the nanoscale is critical in achieving a better resolution in appliances due to a smaller pixel size.[4] The most versatile materials for both, lighting and imaging purposes are rare-earth doped ceramics such as rare earth fluorides as they combine a high chemical and thermal stability with low phonon energies and a large band gap that is situated around the energy levels of the dopant ions.[5,6] The aim of this work is therefore to synthesize well-crystallized, nanoscale ytterbium fluoride that can serve as a high-quality host for luminescent activator dopant ions. A few methods have been established in recent years for the synthesis of metal nanofluroides: the hydrothermal method, the ultrasonic route and the microemulsion technique as well as physical vapour deposition methods, amongst

others. [7-10] We found that the microwave assisted synthesis in ionic liquids (ILs) is particularly suitable for obtaining high purity and well crystallized nanofluorides.[11] ILs as solvents and reaction media are beneficial for the synthesis of nanomaterials as the ionic medium is efficiently able to stabilize electrostatically as well as sterically nanoparticles (NPs) against coalescence and agglomeration.[12] As they are composed of distinct anions and cations, their nature can be adapted to the needs of nanosynthesis of ceramic materials through structural variations on the cation and the anion as well as through the choice of the ion combination.[13] The ILs can be designed in such a way that it serves not only as the reaction medium and nanoparticle stabilizer but also as the reaction partner.[14] For the generation of nanofluorides ILs can be used that serve as a mild fluoride through the decomposition of their complex anions, namely, tetrafluoroborate or hexafluorophosphate. [11] In the context of nanosynthesis, it is even possible to use them as an extraordinarily efficient heat transfer medium. As ILs are composed of ions and the ions themselves typically have a high polarizability ILs are tremendously good microwave absorbers. In consequence, microwave irradiation of ILs leads to extremely high reaction rates leading to high nucleation rates and, in turn, the formation of small particles. Resulting from the direct energy transfer to the reactive species often improved yields, purer products in the synthesis of nanoceramics are observed. [15] But reactions also may proceed in a different way due to altered kinetics which can even lead to products or different polymorphs of crystalline materials. [16]
The aim of this work is to study the influences of two reactive ILs which have distinctly dissimilar properties as well as the impact of different energy providing mechanism - microwave radiation vs. conventional heating - on the formation of ytterbium(III) fluoride nanoparticles. YbF_3 is of importance for a wide number of optical applications where it serves as a host material that has, in addition to good thermal and chemical stability and a large bandgap, a high optical transparency from the UV to the far infra-red region of light.[17]

EXPERIMENTAL DETAILS

SYNTHESES

Synthesis and sample handling were carried out using standard Schlenk and Argon-glove box techniques. The starting chemicals were used as received.

1-Methyl-3-butylimidazolium chloride, [C_4mim]Cl.
For [C_4mim]Cl 73 ml (0.914 mol) 1-methylimidazole (99%, Sigma Aldrich) and 95 ml (0.914 mol) chlorobutane (99%, Acros) were heated in 110 ml acetonitrile (99.5%, J. T. Baker) under reflux at 80 °C for 72 h. After cooling to roomtemperature the solvent was removed under vacuum. The residual pale yellow oil was dissolved in dichloromethane and recrystallized from toluene at -50 °C to yield white crystals. Finally, the product was dried from any remaining solvent for 24 h under dynamic vacuum at 80 °C. Yield: 124.53 g (78 %). ^{1}H-NMR δ_H /ppm (298 K, 250 MHz, $CDCl_3$):10.79 (s, 1 H, N=CH-N), 7.50 (t, 1 H, N-CH=CH-N), 7.37 (t, 1 H, N-CH=CH-N), 4.30 (t, 2 H, N-CH_2-$(CH_2)_2$-CH_3), 4.10 (s, 3 H, N-CH_3), 1,87 (quin., 2 H, N-CH_2-CH_2-CH_2-CH_3), 1.34 (sex., 2 H, N-$(CH_2)_2$-CH_2-CH_3), 0.93 (t, 3 H, N-$(CH_2)_3$-CH_3). Anal. Calcd for $C_8H_{15}N_2Cl$: C, 55.0; H, 8.7; N, 16.0. Found: C, 54.8; H, 8.7; N, 16.1

1-Methyl-3-butylimidazolium tetrafluoroborate, [C_4mim][BF_4].
To obtain [C_4mim][BF_4] a mixture of 122.1 g (0.7 mol) 1-butyl-3-methyl-imidazolium chloride and 76.9 g (0.7 mol) sodium tetrafluoroborate (98%, Aldrich) was added to 800 ml acetonitrile. The mixture was stirred at room temperature for 72 h. The colorless precipitate was filtered off

and the obtained solution washed with acetone and stirred for additional 24 h with 5 g activated carbon. After another filtration, the solvent was removed in vacuo. The residual liquid was mixed with 300 ml dichloromethane (99.9%, Fisher Scientific) and washed with little amounts of water in order to remove the chloride. Finally, the solution was dried over magnesium sulfate, then the solvent was removed in vacuo and the residual liquid was dried at 80 °C for 24 h. Yield: 134.5 g (85 %).
^{1}H-NMR δ_H /ppm (298 K, 250 MHz, $CDCl_3$): 8.64 (s, 1 H, N=CH-N), 7.37 (t, 2 H, N-CH=CH-N), 4.14 (t, J=7.4 Hz, 2 H, N-CH_2-$(CH_2)_2$-CH_3), 3.88 (s, 3 H, N-CH_3), 1.87-1.72 (m, 2 H, N-CH_2-CH_2-CH_2-CH_3), 1.38-1.20 (m, J=7.3 Hz, 2 H, N-$(CH_2)_2$-CH_2-CH_3), 0.86 (t, J=7.3 Hz, 3 H, N-$(CH_2)_3$-CH_3). IR Ξ / [cm^{-1}]: 3164 (w), 2964 (w), 1573 (m), 1466 (w), 1285 (w), 1169 (m), 1033 (s, BF4), 847 (m), 753 (m), 623 (m), 520 (m). Anal. Calcd for $C_8H_{15}N_2BF_4$: C, 42.5; H, 6.7; N, 12.4. Found: C, 42.2; H, 6.6; N, 13.0. Mass spectrometry (FAB) mz. 139.1 ([C_4mim]+), 365.2 (M-[C_4mim]+).

Tributyltetradecylphosphonium tetrafluoroborate, [P_{44414}][BF_4].
The ionic liquid [P_{44414}][BF_4] was synthesized by stirring a mixture of 21.76 g (0.05 mol) tributyltetradecylphosphonium chloride (Cytec Canada Inc.), 5.76 g (0.05 mol) sodium tetrafluoroborate (98%, Aldrich), and 250 ml acetonitrile (99.5% J. T. Baker) at room temperature for 72 h. Then, the mixture was filtered and the colorless precipitate was washed with acetone. The solvent was removed in vacuo and the residual liquid was mixed with 300 ml dichloromethane (99.9% Fisher Scientific). After washing with water until all chloride was removed, the solution was dried over magnesium sulfate (99.99% Riedel de Häen), and the solvent was removed in vacuo. The residual liquid was dried at 80 °C for 24 h. Yield: 20.2 g (83 %). ^{1}H-NMR δ_H /ppm (298 K, 250 MHz, $CDCl_3$): 2.26-2.02 (m, 8 H, P-CH_2-(CH_2)x-CH_3), 1.57-1.40 (m, 16 H, P-CH_2-$(CH_2)_2$-$(CH_2)_x$-CH_3), 1.23 (m, 20 H, P-$(CH_2)_3$-$(CH_2)_x$-CH_3), 0.95 (t, J=6.8 Hz, 9 H, P-$(CH_2)_3$-CH_3), 0.85 (t, J=6.7 Hz, 3 H, P-$(CH_2)_{13}$-CH_3). IR Ξ / [cm^{-1}]: 2921 (w), 1465 (w), 1048 (m). Anal. Calcd for $C_{26}H_{56}PBF_4$: C, 64.2; H, 11.6. Found: C, 63.9; H, 10.7. Mass spectrometry (FAB) mz 399.4 ([P44414]+), 883.7 (M-[P44414]+).

YbF_3 nanomaterial.
In a typical reaction a solution of $4 \cdot 10^{-5}$ mol ytterbium acetate tetrahydrate (99.9% ABCR) in 0.3 ml ethylene glycol (99%, J. T. Baker) was added to 2 ml of [C_4mim][BF_4] or [P44414][BF_4], respectively. For conversion in the microwave the reaction mixture was placed in 10 ml glass vessels equipped with a Teflon© septum and heated within 5 min. to 120 °C in a single mode microwave operating at 2455 MHz (CEM Discover). After 10 min. of heating at 120 °C and continuous stirring the conversion was completed and the reaction mixture was cooled to room temperature by means of pressurized air. Alternatively, the reaction was carried out in Teflon® lined steel autoclaves. Here the mixture was heated at 120 °C for 20h in a lab furnace (Heraeus, Hanau, D). After cooling to room temperature, the resulting colloidal solutions were centrifuged, washed twice with ethanol and once with water. The obtained colorless powders were dried at 90 °C.

CHARACTERIZATION

Elemental Analysis. Elemental analyses were obtained on a Vario EL (Elementar Analysensysteme GmbH, Hanau, D).

Nuclear magnetic resonance (NMR) spectroscopy.

^{1}H-NMR spectra were measured on a Bruker Advance DPX 200 and a Bruker Advance DPX 250 spectrometer (Bruker Germany GmbH, D). The peaks corresponding to the residual protons of the deuterated solvents were used for reference.

Infra-red (IR) spectroscopy.
Attenuated total reflection (ATR) spectroscopy was carried out on an Alpha P ATR spectrometer, which is equipped with a diamond crystal (Bruker, Karslruhe). Solid samples were pressed on the crystal, liquid samples were dropped on the crystal.

Mass (MS) spectrometry.
Mass spectrometry was carried using a VG Autospec mass spectrometer of the company VG instruments (Kent, USA). The spectrometer exhibits EBEE geometry. Due to the low vapour pressure of ionic liquids, fast atom bombardment (FAB) was used to ionize the samples.

Powder X-ray diffraction (PXRD).
Powder X-ray diffraction measurements were carried out on a XRD Huber G670 (Rimsting) operating with monochromatized MoKα radiation. For the measurement, the YF_3 powders were sealed in Lindeman glass capillaries of 0.3 as well as 0.5mm diameter.

Transmission electron microscopy (TEM).
A transmission electron microscope H-8100 of the company Hitachi (Tokyo, Japan) additionally equipped with an Oxford EDX detector Penta FET was applied.

RESULTS AND DISCUSSION

Synthesis.
Tetrafluoroborate ionic liquids are known to release fluoride upon heating and in contact with water. This reaction can be used to convert rare earth salts to the corresponding fluorides. Conveniently, the use of such reactive ILs omits the use of hazardous hydrogenfluoride to generate phase-pure fluoride material. As the fluoride is generated in-situ and is immediately consumed by the rare earth cations, the reaction not only proceeds with a high atom economy but is an extremely benign and safe way to generate nanosized metal fluorides. Aside from providing the fluoride source, the IL also serves as the NP stabilizer. Past experiments have given evidence that in case of ceramic materials the cation plays a decisive role in the NP stabilization as well as the size and morphology control of the final product [17]. For that reason two ILs with distinctly different cations were chosen: The tetrafluoroborate of 1-butyl-3-methylimidazolium and trisbutyl-tetradecylphosphonium. Whilst the 1-butyl-3-methylimidazolium cation ($[C_4mim]^+$) has an aromatic π-system as well as acidic ring protons that can interact with the generated material and also renders the IL in itself more hydrophilic, the trisbutyl-tetradecylphosphonium cation ($[P_{44414}]^+$) is not only considerably larger (and thus less basic [19]), but it featuress also a long alkyl chain, saturated cation which makes the IL itself substantially more hydrophobic.

To convert the starting material, ytterbium(III) acetate, to the trifluoride by reaction with the tetrafluoroborate ionic liquid two different heat sources were examined: First, conventional heating where glass containers with the reaction mixture were heated in a laboratory furnace. Heating was achieved here via classical heat transfer. Secondly, direct, dielectric heating of the reaction medium and the starting material via microwave irradiation was explored. Full conversion of the starting materials to the products was achieved already in a few minutes due to the efficient energy uptake of the IL.

Powder X-ray Diffraction.

In order to analyse the products from conversion of ytterbiumacetate tetrahydrate with $[C_4mim][BF_4]$ and $[P_{44414}][BF_4]$ to YbF_3 under microwave and conventional heating, X-ray powder diffraction (PXRD) studies were carried out. For all samples, the diffraction peaks in the powder diffraction patterns (shown in Fig. 1) can be attributed to YbF_3 crystallizing in the YF_3 type of structure. [20] No diffraction peaks pointing to impurities like, for example, YbOF or Yb_2O_3 or the starting materials could be detected. However, the relative intensities of the diffraction peaks vary for the materials obtained via conventional heating in a furnace (Fig. 1 b and c) compared to the ones obtained from microwave heating (Fig. 1 d and e). This becomes most obvious when comparing the relative intensities of the (111) and (020) diffraction peaks. For the material obtained by conventional heating, the relative peak intensities are quite similar to the expected values, as can be seen by comparison with the simulated powder pattern (Fig. 1 a), whereas for the samples, that were heated in the microwave, the (020) diffraction peaks gain significantly more intensity than the (111) diffraction peaks indicating substantial texture effects and an anisotropic particle growth.

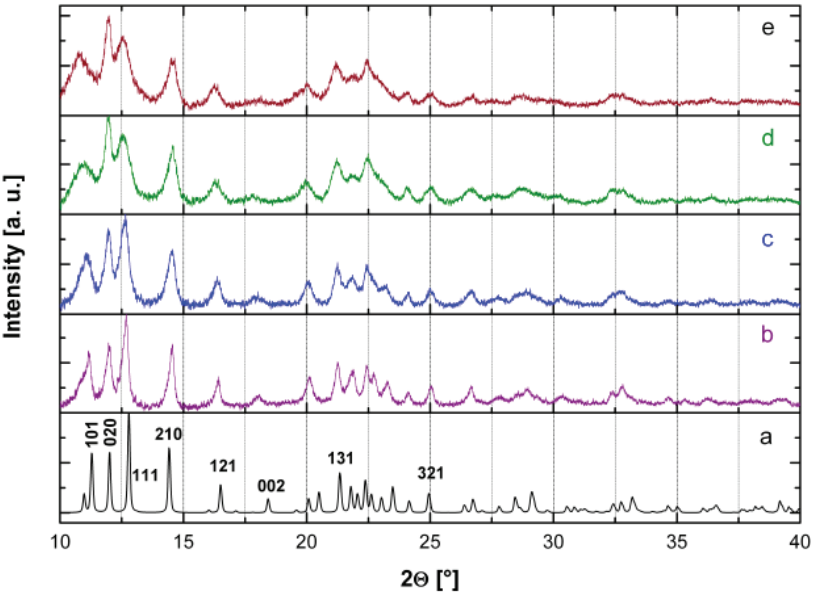

Figure 1. Powder X-ray diffraction pattern of synthesized YbF_3. a) Database pattern simulated from ICSD 9844, b) YbF_3 synthesized with $[C_4mim][BF_4]$ by in the furnace, c) with $[P_{44414}][BF_4]$ in the furnace, d) with $[C_4mim][BF_4]$ in the microwave, e) with $[P_{44414}][BF_4]$ in the microwave.

In addition, the particles synthesized in the microwave seem to have a larger peak width, which points to a smaller particle size. In order to quantize this assumption, the particle size has been calculated from the full width half maximum (FWHM) of diffraction peaks at different diffraction angles using the Debye-Scherrer equation (eq. 1) with K being the particle shape constant (0.9 is used here), λ being the wavelength of the used radiation (Mo-K_α, 0.07093 nm):

$$t = \frac{K \cdot \lambda \cdot 57.3}{FWHM \cdot \cos\Theta} \qquad \text{equ. 1}$$

Unfortunately, the broadness of the diffraction peaks leads to a large overlap. For that reason, only the (210) and (121) diffraction peaks are considered to calculate the crystal particle size as they do not overlap with neighbouring diffraction peaks (Table 1).

Table 1: Debye-Scherrer particle size evaluation for the different YbF_3 samples.

Synthesis route	hkl	FWHM [°]	Particle size /nm
$[C_4mim][BF_4]$, furnace	(020)	0.320	11.97
	(111)	0.285	12.86
	(210)	0.265	13.92
	(121)	0.265	13.95
$[P_{44414}][BF_4]$, furnace	(020)	0.370	10.35
	(111)	0.460	7.96
	(210)	0.410	8.99
	(121)	0.365	10.13
$[C_4mim][BF_4]$, microwave	(020)	0.623	6.12
	(111)	1.08	3.39
	(210)	0.440	8.38
	(121)	0.470	7.86
$[P_{44414}][BF_4]$, microwave	(020)	0.595	6.42
	(111)	1.09	3.36
	(210)	0.495	7.45
	(121)	0.465	7.95

Noticeably, the particles synthesized in the furnace exhibit a larger size than the particles synthesized in the microwave. In addition, the particles synthesized with $[C_4mim][BF_4]$ seem to be slightly larger than those obtained from $[P_{44414}][BF_4]$. To confirm this, transmission electron microscopic (TEM) studies were undertaken.

Transmission Electron Microscopy (TEM).

The TEM micrographs observed for the YbF_3 particles synthesized in the furnace with $[C_4mim][BF_4]$ are presented in Fig 2. On the left site, an overview micrograph shows rhombic particle agglomerations with an average length of 400 nm and a width of about 250 nm. In fact, the rhombic agglomeration consists of smaller particles and crystalline growth areas are shown in the upper left insert of Fig. 2. The crystalline area has been enlarged in order to emphasize the particle intergrowth. Lattice plane resolution could be achieved (Fig. 2, bottom left) and the TEM image confirms the uniform crystalline growth. This is supported by the corresponding selected area electron diffraction pattern (SAED), shown in Figure 2, bottom right. The electron diffraction pattern consists of single diffraction peaks which meet reflection conditions for YbF_3 crystallizing in the YF_3 type of structure. The size of the single crystalline areas is in agreement with the PXRD observations.

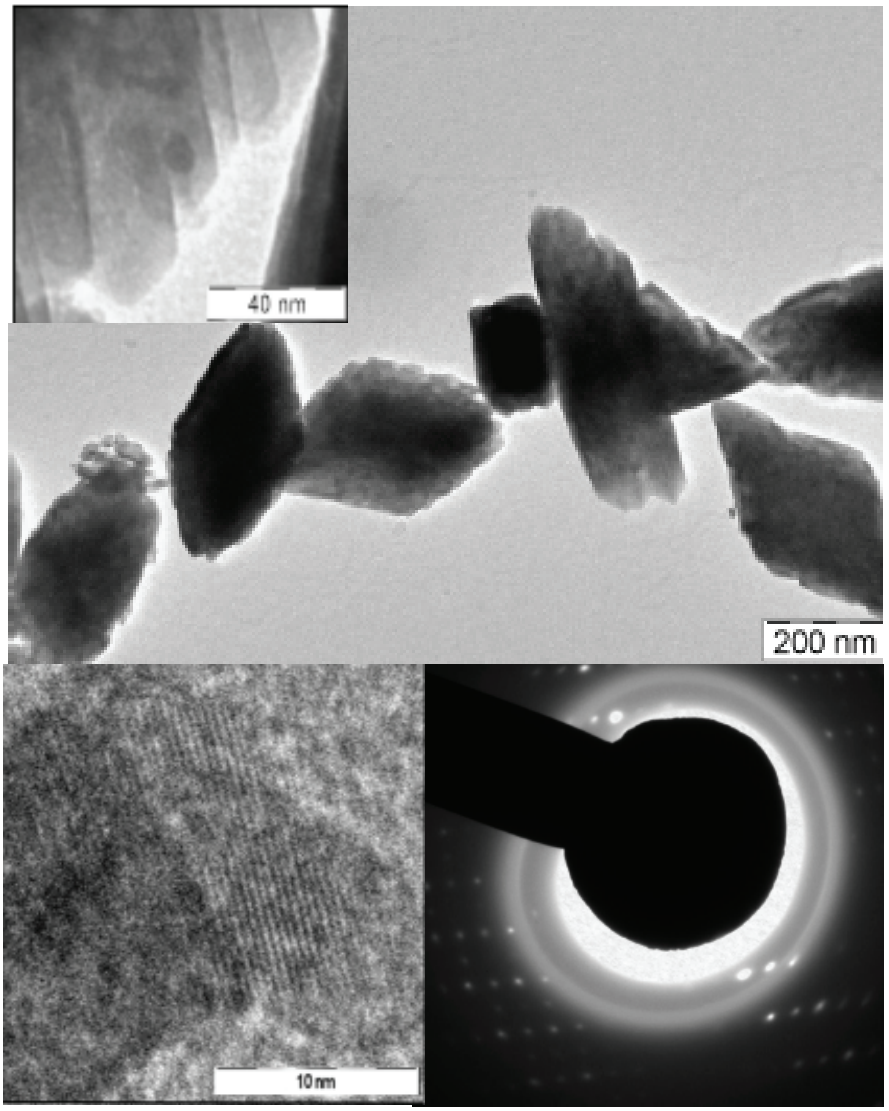

Figure 2. TEM micrographs and YbF_3 particles synthesized from $[C_4mim][BF_4]$ in the furnace.

TEM micrographs of YbF_3 synthesized with $[C_4mim][BF_4]$ under microwave irradiation are displayed in Fig. 3. They show small particles forming bundle like agglomerates. These

agglomerates have an average length of 800 nm and a width of about 280 nm. The individual particle size varies in a range of 5-20 nm which is in good agreement with the PXRD results.

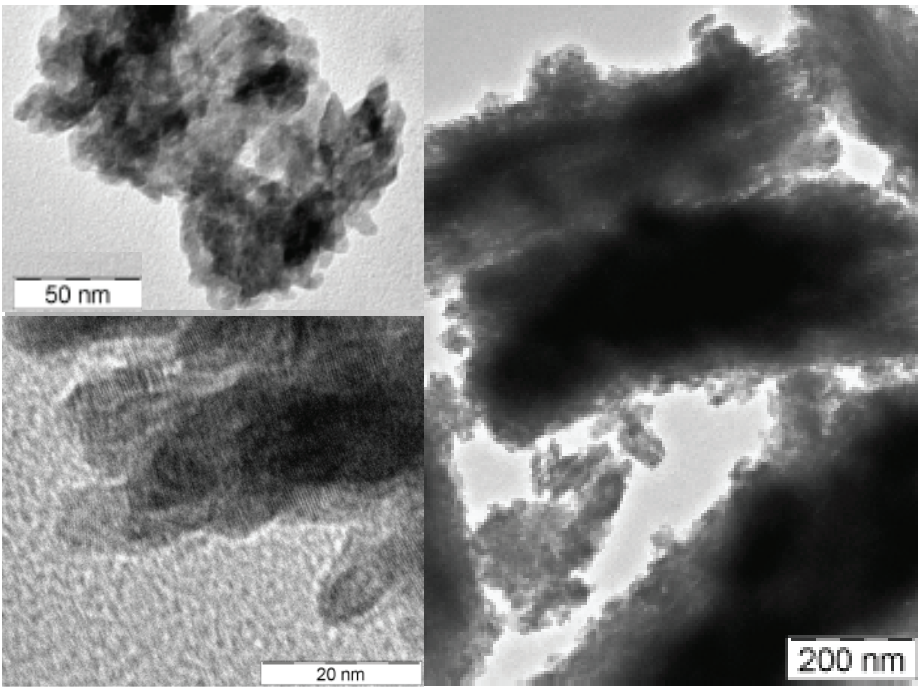

Figure 3. YbF_3 particles synthesized from $[C_4mim][BF_4]$ in the microwave.

On the contrary to the previous samples, smaller particles can be obtained when using the hydrophobic phosphonium ionic liquid $[P_{44414}][BF_4]$. For material prepared from this ionic liquid by heating, the TEM micrographs (Fig. 4) reveal particle with an average size of 10 nm. Still aggreagates form, but the particles appear to be much more separated compared to synthesis in $[C_4mim][BF_4]$, HRTEM and SAED confirm that these areas are single crystalline. However, it has to be noted that the observed individual diffraction peaks are broadened comparted to the material obtained by a similar procedure in $[C_4mim][BF_4]$. First signs of diffraction rings also point to increasing polycrystallinity.

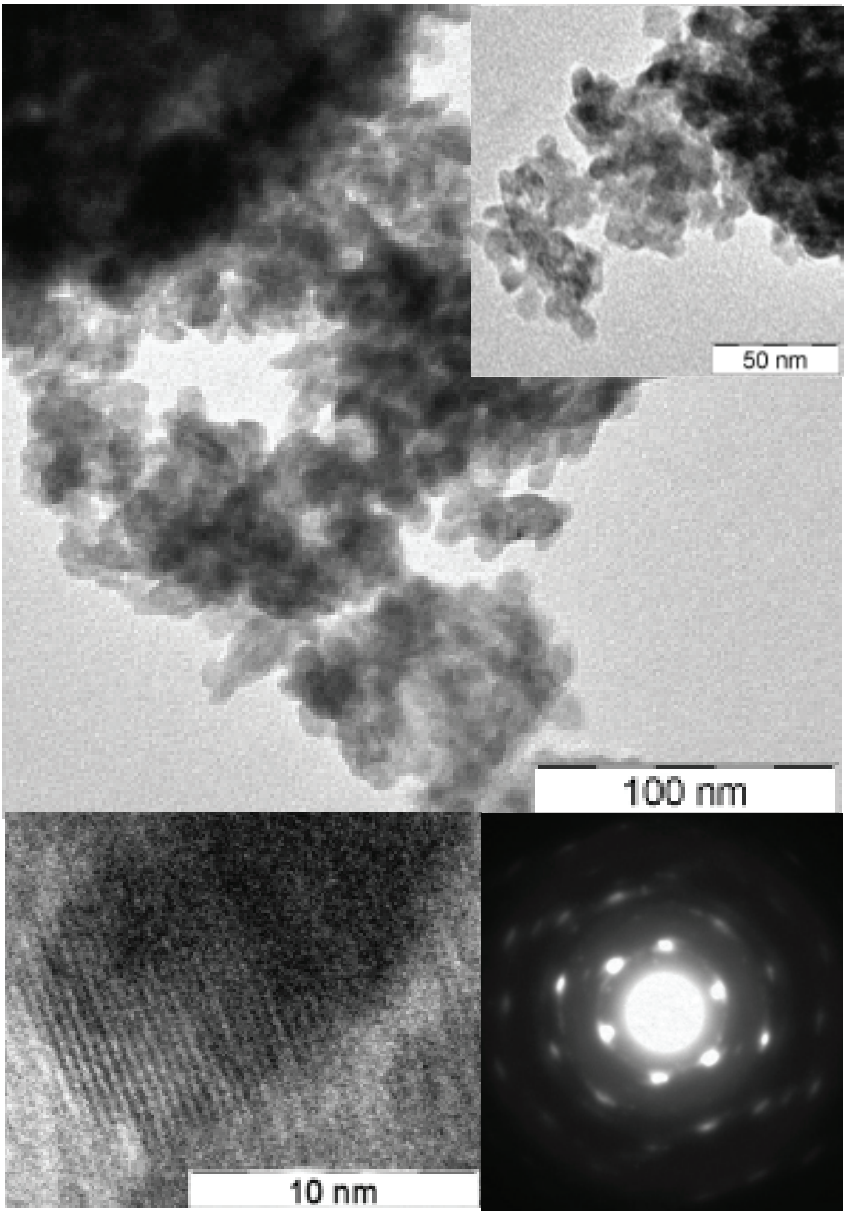

Figure 4. YbF_3 particles synthesized from $[P_{44414}][BF_4]$ in the furnace.

Also for YF_3 material synthesized form $[P_{44414}][BF_4]$ in the microwave, the particles seems to be more loosely aggregated that when $[C_4mim][BF_4]$ was employed in the synthesis (Fig. 5). Yet, loose aggregates with a length of about 850 nm and a width of 200 nm can be made out. However, in contrast to the synthesis in the furnace, when microwave irradiation is used as the energy providing source, the particles become less uniform and the size distribution spreads between 5 and 80 nm.

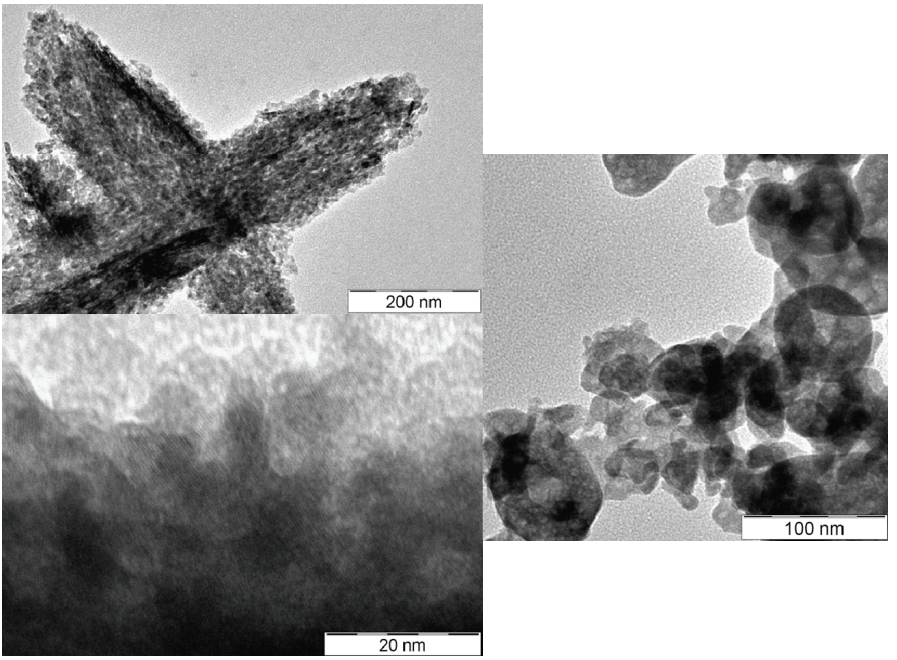

Figure 5. YbF_3 particles synthesized from $[P_{44414}][BF_4]$ under microwave irradiation.

CONCLUSIONS

YbF_3 nanoparticles of high crystallinity were successfully synthesized by reacting ytterbium acetate hydrate with 1-butyl-3-methylimdazolium and trisbutyltetradecylphosphonium tetrafluoroborate under conventional heating or by microwave irradiation. The tetrafluoroborate salts serve a multi-fold purpose: They are not only the solvent for the starting material and the reaction medium, but also the fluoride source and serve as the stabilizing agent for the nanoparticles. Thus, no additional surfactants and stabilizers need to be used to obtain nanoparticles. However, due the fact that the tetrafluoroborate ion decomposes, the particles had to be cleaned from the stabilizing IL prior to TEM investigations. This lead to substantial particle aggregation. This is commonly observed for nanomaterial obtained from ILs. Nevertheless, it is possible re-disperse the material in the IL or another solvent by sonication. When it comes to microwave synthesis, the IL provides steep heating rates through dielectric

heating. Thus, the reaction times could be reduced substantially – from hour for conventional heating to minutes. However, this certainly affected the product. The microwave reaction not only proceeded faster but also yielded smaller particles compared to conventional heating. However, the extended reaction time of the conventional heating procedure resulted in a higher product crystallinity and in smaller particle size distributions. Not only the heating procedure affected the particle size and morphology, but also the cation of the ionic liquid showed a notable impact. In case of trisbutyltetradecylphosphonium tetrafluoroborate smaller and more separted particles could be obtained, when compared to products obtained from 1-butyl-3-methylimidazoliumtetrafluoroborate. Nevertheless, in all cases material of small particle size and high crystallinity could be obtained in relatively safe and mild procedures.

ACKNOWLEDGEMENTS
This work was supported by in part by the European Research Council with an ERC Starting Grant (EMIL) and by the Critical Materials Institute, an Energy Innovation Hub funded by the U.S. Department of Energy, Office of Energy Efficiency and Renewable Energy, Advanced Manufacturing Office.

References

[1] http://www.eia.gov/tools/faqs/faq.cfm?id=99&t=3. Last accessed: Jan. 13th 2015.
[2] http://apps1.eere.energy.gov/buildings/publications/pdfs/ssl/ee_lighting_vol2.pdf. Last accessed: Jan. 13th 2015.
[3] G. Blasse, B.C. Grabmaier, Luminescent Materials, Springer-Verlag, Berlin, Heidelberg, 1994.
[4] X. Chen, Y. Liu, D. Tu, Lanthanide-Doped Luminescent Nanomaterials: From Fundamentals to Bioapplications (Nanomedicine and Nanotoxicology), Springer-Verlag, Berlin, Heidelberg, 2014.
[5] P. Ghosh, C. Lorbeer, A.-V. Mudring, Nanofluorides for environmentally benign lighting and energy conversion in solar cells, in Florine-Related nanoscience with Energy Applications, ACS Symposium Series, 2011, 1064, 87-99.
[6] C. Lorbeer, F. Behrends, J. Cybinska, H. Eckert, A.-V. Mudring, J. Mat. Chem. C 2014, 2, 9439-9450.
[7] I. A. de Ćarcer, P. Herrero, A. R. Landa-Ćanovas, B. Sobolev, Appl. Phys. Lett., 2005, 87, 53105
[8] P. Ptacek,H. Schäfer, K. Kömpe, M. Haase, Adv. Funct. Mater., 2007,17, 3843.
[9] L. Zhu, X. Liu, J. Meng and X. Cao, Cryst.Growth Des., 2007,7, 2505.
[10] K. Richter, C. Lorbeer, A.-V. Mudring, Chem. Commun. 2015, 51, 114-117.
[11] C. Lorbeer, J. Cybinska, A.-V. Mudring, Chem. Commum., 2010, 46, 571-573.
[12] C. Lorbeer, J. Cybinska, A.-V. Mudring Cryst. Growth Des., 2011, 11, 1040-1048; C. Lorbeer, J. Cybinska, E. Zych, A.-V. Mudring, Opt. Mat. 2011, 21, 3207; C. Lorbeer, A.-V. Mudring, J. Phys. Chem. C, 2013, 12229-12238; C. Lorbeer, A.-V. Mudring, ChemSusChem, 2013, 6, 2382-2387; C. Lorbeer, A.-V. Mudring, Chem. Commun. 2014, 50, 13282-13284.
[12] K. Richter, P. S. Campbell, T. Bäcker, A. Schimitzek, D. Yaprak, A.-V. Mudring, physica status solidi b, 2013, 250, 1152-1164; K. Richter, A. Birkner, A.-V. Mudring, Phys. Chem. Chem. Phys., 2011, 13, 7136–7141.
[13] T. Alammar, H. Noei, Y. Wang, W. Grünert, A.-V. Mudring, ACS Sustainable Chemistry and Engineering 2015, 3, 42-54; T. Alammar, I. Hamm, A.-V. Mudring, M. Wark, Appl. Catalysis B 2015, xx, ahead of print; T. Alammar, H. Noei, Y. Wang, A.-V. Mudring,

Nanoscale, 2013, 5, 8045-8055.; T. Alammar, O. Shekhah, J. Wohlgemuth, A.-V. Mudring, J. Mater. Chem., 2012, 22, 18252-18260.; T. Alammar, A.-V. Mudring, ChemSusChem, 2011, 12, 1796-1804.
[14] P. S. Campbell, C. Lorbeer, J. Cybinska, A.-V. Mudring, Adv. Funct. Mater., 2013, 23, 2924-2931; C. Lorbeer, J. Cybinska, A.-V. Mudring, J. Mater. Chem., 2012, 22, 9505-9508; C. Lorbeer, J. Cybinska, E. Zych, A.-V. Mudring, ChemSusChem, 2011, 4, 595-598.
[15] T. Alammar, Kit Chow, A.-V. Mudring, New J. Chem., 2015, 39, 1339 – 1347.
[17] C. Lorbeer, J. Cybinska, A.-V. Mudring, , J. Mat. Chem. C, 2014, 2, 1862-1868.
[18] S. Shinoya, W.M. Yen, H. Yamsmoto, Phosphor Handbook (Laser and Optical Science and Technology), CRC Press, Taylor & Francis Group, Boca Raton, 2007.
[19] A. Babai, G. Kopiec, A. Lackmann, B. Mallick, S. Pitula, S.-F. Tang, A. Babai, A.-V. Mudring, J. Mol. Liq. 2014, 92, 191-198; S. Pitula, A.-V. Mudring, Phys. Chem. Chem. Phys., 2010, 12, 7056-7063. J. Bartosik, A.-V. Mudring, Phys. Chem. Chem. Phys., 2010, 12, 4005-4011.
[20] M. M. Lage, A. Righi, F.M. Matinaga, J.-Y. Gesland, R.L. Moreira, Journal of Physics: Condensed Matter 2004, 16, 3207-3218; O. reis, O.; T. Petzel, Z. Anorg. Allg. Chem. 1973, 403, 1-22.

Author Index

WILEY END USER LICENSE AGREEMENT

Go to www.wiley.com/go/eula to access Wiley’s ebook EULA.